2011

Demonstration of extractive cryocooled inert preconcentration with FTIR spectroscopy instrumentation and methodology for autonomous measurements of atmospheric organics

Patrick I. Buckley

DEMONSTRATION OF EXTRACTIVE CRYOCOOLED INERT PRECONCENTRATION WITH FTIR SPECTROSCOPY INSTRUMENTATION AND METHODOLOGY FOR AUTONOMOUS MEASUREMENTS OF ATMOSPHERIC ORGANICS

by

PATRICK I. BUCKLEY

A DISSERTATION

Submitted in partial fulfillment of the requirements
for the degree of Doctor of Philosophy
in
The Department of Atmospheric Science
to
The School of Graduate Studies
of
The University of Alabama in Huntsville

HUNTSVILLE, ALABAMA

2011

In presenting this thesis in partial fulfillment of the requirements for a doctorate degree from The University of Alabama in Huntsville, I agree that the Library of this University shall make it freely available for inspection. I further agree that permission for extensive copying for scholarly purposes may be granted by my advisor or, in his absence, by the Chair of the Department or the Dean of the School of Graduate Studies. It is also understood that due recognition shall be given to me and to The University of Alabama in Huntsville in any scholarly use which may be made of any material in this dissertation.

Buchlux _____ 10/31/2011 _____
(date)

DISSERTATION APPROVAL FORM

Submitted by Patrick I. Buckley in partial fulfillment of the requirements for the degree of Doctor of Philosophy in Atmospheric Science and accepted on behalf of the Faculty of the Graduate Studies by the dissertation committee.

We, the undersigned members of the Graduate Faculty of The University of Alabama in Huntsville, certify that we have advised and/or supervised the candidate on the work described in this dissertation. We further certify that we have reviewed the dissertation manuscript and approve in partial fulfillment of the requirements for the degree of Doctor of Philosophy in Atmospheric Science.

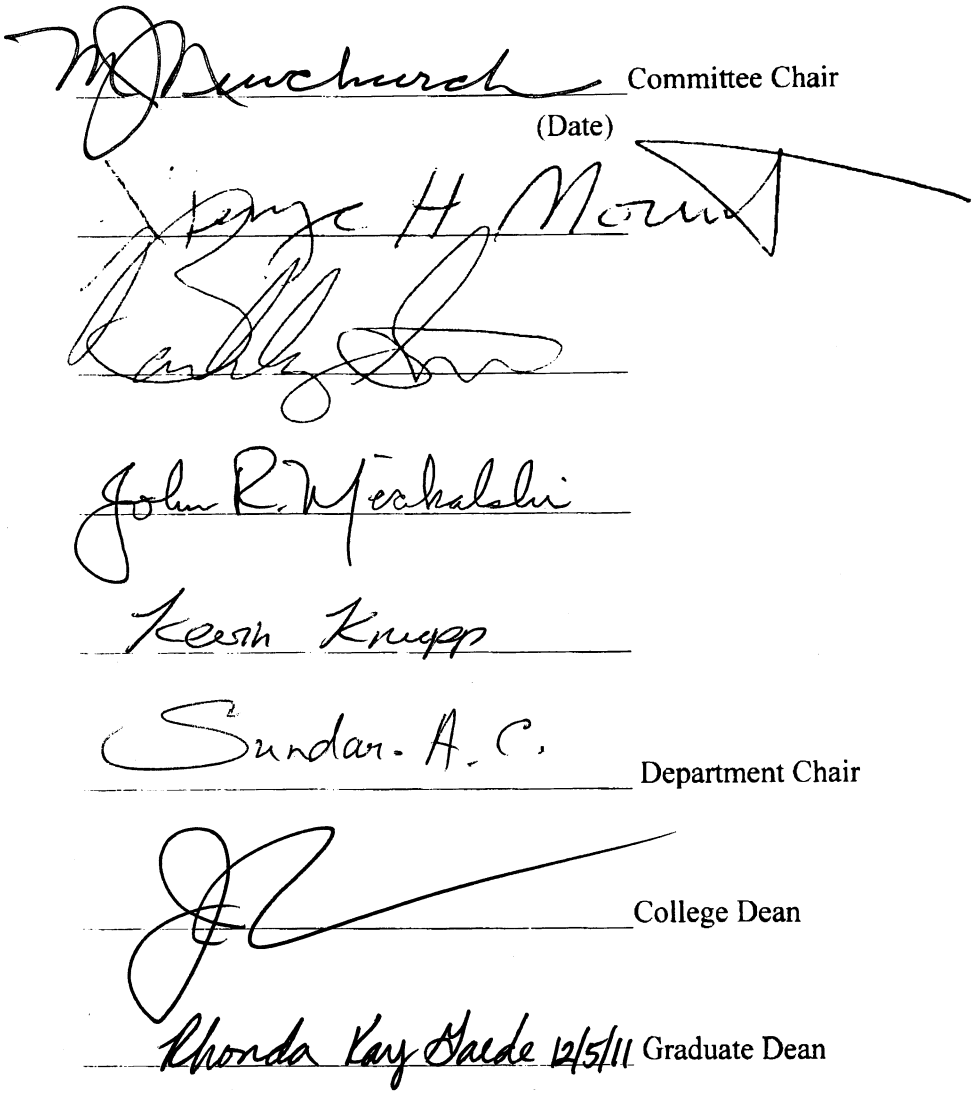

Committee Chair

(Date)

Department Chair

College Dean

Graduate Dean

ABSTRACT

The School of Graduate Studies
The University of Alabama in Huntsville

Degree Doctor of Philosophy College/Dept. Science/Atmospheric Science

Name of Candidate Patrick I. Buckley

Title Demonstration of Extractive Cryocooled Inert Preconcentration with FTIR Spectroscopy Instrumentation and Methodology for Autonomous Measurements of Atmospheric Organics

At present researchers exclusively use gas chromatography (GC) systems to monitor multiple volatile organic compounds (VOCs) in either real- or near-real-time. We have designed, developed, and constructed an experimental atmospheric air-quality monitoring system capable of measuring low-concentration VOCs using advanced optical techniques. This system uses a commercial Fourier Transform Infrared spectrometer (FTIR), a commercial long-path gas cell, a commercial acoustic Stirling cryocooler, and a custom cryogen-free cryotrap to autonomously monitor a multi-pollutant suite of VOCs with on-board quality assurance/quality control (QA/QC) calibration. Every four hours, the system records a five minute co-added FTIR interferogram using preconcentrated batch samples which are thermally desorbed from the cryotrap into the gas cell. From this interferogram, the spectral processing algorithm calculates a corresponding absorption spectrum and derives trace gas concentrations using a peak fitting technique to achieve compound-specific detection limits of

6-60 parts per trillion volume (pptv). During the calibration cycle, the system acquires QA/QC measurements made in a similar fashion using high-purity calibration gas bottles.

The presented laboratory results show the system is capable of measuring single- and multi-component calibration gas mixtures within the manufacturer's accuracy specifications. *In situ* canister samples analyzed using gas chromatography with electron capture and flame ionization detection (GC/ECD/FID) presents a narrow background for possible VOC concentrations at the National Space Science and Technology Center (NSSTC) in Huntsville, AL. *In situ* observations by the FTIR-based system showcase the capabilities of the system to run fully autonomously and analyze a complex atmospheric mixture with a high degree of fidelity. Complex error analysis highlights the shortfalls of this methodology and presents quantitative correction factors for a number of systematic error sources. The results demonstrate the utility of this technology for a wide range of atmospheric gas-phase organics research and monitoring applications in a number of environments.

Abstract Approval: Committee Chair 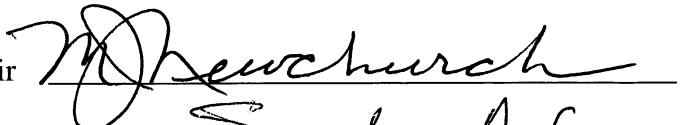

Department Chair 

Graduate Dean 

ACKNOWLEDGMENTS

First and foremost, I have to acknowledge the love and support of my Lord and Savior Jesus Christ. Without the assurance of His presence in my life and His gift of the Holy Spirit, I would not be able to endure ANY challenge, especially the challenge of my Ph.D. work over the last five years.

Secondly, to my loving wife, Courtney, and my beautiful daughter, Mary Abilene, it has been the greatest joy of my life to be your husband and father. Your constant encouragement and unfailing love has seen me through this arduous time and has allowed me to complete my work without any undue pressure.

Thirdly, each of my committee members has affected me and my research in very profound ways. Dr. Newchurch has provided me with the scientific basis to become the researcher I am today. His influence will have a dramatic affect on me for the remainder of my life, in and out of the workplace. Dr. Sive has generously given his time and supplies to provide invaluable data and given me the tools to perform in-depth research with Phoenix. The validation measurements provided by Dr. Sive gave me the encouragement I needed to complete my work. Dr. Mount has provided me with the drive and knowhow to attack FTIR optics with careful precision. His encouragement throughout the completion of my research provided me with untold motivation. Dr. Knupp showed me how to perform careful field observations and the importance of boundary layer dynamics in performing accurate data analysis. Dr. Mecikalski has driven me these last few months to completion and has shown me how to balance my research.

Special gratitude belongs to Mr. David Bowdle, whose vision and innovation brought this project to life. Throughout my time at UAHuntsville, David has led me to

diligently consider every detail when it comes to complex instrument development. Through David's foresight Phoenix has become what it is today and what it potentially will become.

Finally, I would be remiss if I didn't thank my fellow students and colleagues, three in particular, Guanyu (Brian) Huang, Wes Cantrell, and Andrew Jones. Brian and Wes helped me collect the data that makes up the majority of the important work contained within. Brian has helped keep me sane during my research with our in-depth discussions of the Premiership, the Champions League, and all things football. Andrew spent two summers helping me get the mechanical and electrical components of Phoenix debugged and installed. Also, Andrew taught me many things about the fine art of 3D computer aided design.

TABLE OF CONTENTS

Page

List of Figures

List of Tables

List of Abbreviations

AC	--	alternating current
AI	--	analog input
AO	--	analog output
AppalAIR	--	Appalachian Atmospheric Interdisciplinary Research
AVOC	--	anthropogenic VOC
BL	--	boundary layer
BVOC	--	biogenic VOC
CDT	--	Central Daylight Time
CFIC	--	Clever Fellows Innovation Consortium
CLS	--	classical least squares
DAQ	--	data acquisition
DTGS	--	deuterated triglycine sulfate
ECD	--	electron capture detector
ECIP-FTIR	--	extractive cryocooled inert preconcentration FTIR
EMI	--	electromagnetic interference
EPA	--	Environmental Protection Agency
FGCMS	--	Fast GC/MS
FID	--	flame ionization detector
FTIR	--	Fourier transform infrared
FSL	--	fused silica lined
GC	--	gas chromatograph(y)
Gen I	--	first generation
Gen II	--	second generation
GHG	--	greenhouse gas
ILS	--	instrument line shape
IR	--	infrared
JCDH	--	Jefferson County Department of Health
LN_2	--	liquid nitrogen
LPM	--	liters per minute
MCT	--	mercury cadmium telluride
MDL	--	minimum detection limit
MFC	--	mass flow controller
MFM	--	mass flow meter
mLPM	--	milliliters per minute

MS	--	mass spectroscopy
NAAQS	--	National Ambient Air Quality Standard
NBL	--	nocturnal boundary layer
NCAR	--	National Center for Atmospheric Research
NESDIS	--	National Environmental Satellite, Data, and Information Service
NI	--	National Instruments
NIOSH	--	National Institute of Occupational Health and Safety
NLLS	--	non-linear least squares
NMHC	--	non-methane hydrocarbons
NOAA	--	National Oceanic and Atmospheric Administration
NSSTC	--	National Space Science and Technology Center
OPUS	--	Optical Users Software
OVOC	--	oxygenated VOC
PC	--	personal computer
PLS	--	partial least squares
PNNL	--	Pacific Northwest National Laboratory
ppbv	--	parts per billion by volume
pptv	--	parts per trillion by volume
PRT	--	platinum resistance thermometer
PTR	--	proton transfer reaction
QA	--	quality assurance
QC	--	quality control
RFI	--	radio frequency interference
RH	--	relative humidity
RMS	--	root mean squared
sccm	--	standard cubic centimeters per minute
SCXI	--	signal conditioning extension for instrumentation
SOA	--	secondary organic aerosol
SRC	--	speed relay control
SS	--	stainless steel
SSR	--	sum of the squares of residuals
TE	--	thermal electromotive
TRACE-P	--	Transport and Chemical Evolution over the Pacific
UNH	--	University of New Hampshire
UPS	--	Universal Power Supply
UV	--	ultraviolet

VI	--	virtual instrument
VOC	--	volatile organic compound
WAS	--	whole air sample

List of Symbols and Variables

T	--	transmission, temperature [K]
λ	--	wavelength [cm]
$\tilde{\nu}$	--	wavenumber [cm^{-1}]
I	--	radiance [W sr^{-1} m^{-2}]
b	--	pathlength [cm]
α	--	absorption coefficient [cm^{-1}]
σ	--	absorption cross section [cm^2 $molecule^{-1}$]
A	--	absorbance [AU]
c	--	concentration [molecules cm^{-3}]
L	--	source radiance [W sr^{-1} m^{-2}]
a	--	source area [cm]
Ω	--	solid angle [rad]
η	--	optical efficiency, mixing ratio [ppbv, pptv]
G	--	detector gain [dB]
$\Delta\nu$	--	resolution [cm^{-1}]
t	--	time [sec]
$\boldsymbol{K}_{0,1}$	--	residual error matrix
F	--	flow rate [sccm]
V	--	volume [L, cm^3]
δ	--	delta function
Π	--	rectangular function
m	--	slope
d	--	intercept
n_0	--	Loschmidt's constant [molecule cm^{-3}]
k_B	--	Boltzmann Constant [J K^{-1}]

CHAPTER I

INTRODUCTION

Both anthropogenic and biogenic sources contribute to the total global volatile organic compound (VOC) burden in the atmosphere. Biogenic VOCs (BVOCs) account for ~1150 Tg yr^{-1} globally of which 84 Tg yr^{-1} (~14%) comes from North America [*Guenther et al.*, 1995; *Guenther et al.*, 2000], while anthropogenic VOCs (AVOCs) contribute ~110 Tg yr^{-1} globally, 19.5 Tg yr^{-1} (21%) from the United States [*Piccot et al.*, 1992]. Homogeneous gas-phase oxidation of VOCs [*Atkinson and Arey*, 2003] contributes to air quality and climate in two significant areas. First, these organic hydrocarbons are precursors to ozone (O_3) production, an important greenhouse gas (GHG) and tropospheric oxidant [*Atkinson*, 2000; *Chameides et al.*, 1992; *Fehsenfeld et al.*, 1992; *Ryerson et al.*, 2001]. Second, the oxidation of VOCs produces low-volatility products which can nucleate into secondary organic aerosol (SOA) [*Griffin et al.*, 2002; *Hoffmann et al.*, 1997; *Ng et al.*, 2007].

In addition to O_3 and SOA production, emissions of AVOCs and photochemical production of secondary products have negative effects on human health [*Devlin et al.*, 1997; *Sicard et al.*, 2011], vegetation [*Hartikainen et al.*, 2009; *Karnosky et al.*, 2007], and visibility [*Jacobson and Streets*, 2009]. Also, formation of SOA impacts the radiative balance of the atmosphere [*Jacobson and Streets*, 2009]. Plus, Title III of the 1990 Clean Air Act Amendments lists 189 compounds as hazardous air pollutants capable of causing various types of cancer and respiratory maladies [*EPA*, 1990]. Thus, in order to investigate the

chemical processes regulating O_3 and SOA formation and subsequent chemical transformations, researchers must accurately identify and quantify the temporal and spatial variation of VOCs.

In response, the Environmental Protection Agency (EPA) has outlined a number of Compendia for monitoring atmospheric organic compounds. Although distinct, these methods have some fundamental similarities. The sample measurement procedure follows a straightforward process involving ambient sample collection in the field, followed by sample processing and analysis in a regional laboratory. The four general sample collection methods involve a) drawing air through sampling cartridges containing sorbent materials specific to the compounds of interest; b) drawing air through either reactive sorbent or non-reactive absorbent filters; c) drawing air into a low-temperature chamber that condenses the selected analytes; and d) drawing air into an evacuated sample canister.

A constant issue with sample degradation is evident when the sample is collected in the field and analyzed at a later time, particularly when extreme care is not taken. As the time between sample collection and analysis increases, the compounds begin reacting or degrading. This problem leads to errors in the analysis of field-collected samples, particularly for oxygenated VOCs (OVOCs) [*Doezema et al.*, 2010; *Kelly and Holdren*, 1995; *Ochiai et al.*, 2002].

The focus of this study is a continuation of my previous thesis work [*Buckley*, 2009] to design, fabricate, optimize, and demonstrate a novel ambient air quality sensor enabling dramatic improvements in current EPA standard organics monitoring technologies. This sensor uses a Fourier Transform Infrared (FTIR) spectrometer, a commercial long-path gas cell, a commercial acoustic Stirling cryocooler, and a single cryogen-free cryotrap integrated

into an autonomous system with on-board quality control/quality assurance (QC/QA). We refer to this methodology as Extractive Cryocooled Inert Preconcentration with FTIR spectroscopy (ECIP-FTIR; hereafter referred to as Phoenix). This Dissertation describes in detail instrument design decisions, laboratory design and operations, and initial laboratory and field measurements to illustrate the utility of this technology as an upgrade for current EPA air quality sensors.

Chapter II of this dissertation outlines the current state of knowledge available regarding VOC chemistry, particularly its influence in O_3 production. Chapter II also describes the comparable existing standard method used by the EPA, and the existing advanced VOC monitoring methods. Chapter III describes the key methodologies applied in the described method, particularly a thorough description of FTIR methodology and error sources, and two quantitative methodologies, univariate and multivariate linear regression using Beer's Law. Chapter IV describes the key subsystems of Phoenix including flow schematics, system capabilities, and optical, fluid, communication, and auxiliary subsystem designs, and how these subsystems combine into an automated field analysis device. Chapter V presents analysis of field survey data collected during a one-week field readiness study performed using whole air samples (WAS) collected at the National Space Science and Technology Center (NSSTC) in Huntsville, AL. This data serves as background information for the acceptable mixing ratios of the compounds monitored by Phoenix. Chapter V also presents preliminary field data collected by Phoenix on 12-18 September 2011 to demonstrate the capabilities of the system to autonomously monitor ambient VOCs. This chapter also includes data and error analysis quantifying the accuracy and precision of this method and critical device-specific error sources. Chapter VI outlines the future work with

Phoenix as a field-ready device emphasizing possible deficiencies with the method before advancing to an optimized system with long-term unattended operation at a field site. Finally, Chapter VII contains the conclusions drawn from the design, development, and deployment of the Phoenix Generation I (Gen I) instrument and how these conclusions will lead to improvements in the design of future Phoenix systems.

CHAPTER II

BACKGROUND

a. VOC Atmospheric Chemistry

VOCs play an important role in the production and loss of atmospheric O_3. Numerous researchers have performed extensive studies on the kinetics and monitoring of VOCs and their interaction with O_3 [e.g., *Ambrose et al.*, 2007; *Apel et al.*, 2008; *Atkinson*, 2000; *Berkowitz et al.*, 2005; *Biesenthal et al.*, 1997; *Blanchard et al.*, 2010; *Chameides et al.*, 1992; *Doraiswamy et al.*, 2009; *Gilman et al.*, 2009; *Goldan et al.*, 1995; *Jenkin et al.*, 1997; *Kleinman*, 2005; *Pressley et al.*, 2004; *Qin et al.*, 2007; *Rappenglück and Fabian*, 1999; *Ryerson et al.*, 1998; *Sillman et al.*, 1998; *Sillman and He*, 2002; *Volkamer et al.*, 2005; *Wang et al.*, 2002; *Wert et al.*, 2003; *Wong and Stutz*, 2010; *Xiao et al.*, 2010]. As a result of this research, it is clear there are a wide range of possible outcomes for VOCs emitted in the atmosphere. Diurnal [e.g., *Blanchard et al.*, 2010; *Gorham et al.*, 2010; *Qin et al.*, 2007] and nocturnal [e.g., *Banta et al.*, 1998; *Brown et al.*, 2007; *Warneke et al.*, 2004; *Wong and Stutz*, 2010] differences are particularly important, especially in boundary layer chemistry [*Banta et al.*, 2007; *Couach et al.*, 2003; *Jenkin and Clemitshaw*, 2000; *Salmond and McKendry*, 2002; *Wong and Stutz*, 2010] and its effect on surface air quality [*Atkinson*, 2000; *Fenger*, 1999; *Lippmann*, 1991; *Miller et al.*, 2010; *Weisel*, 2002].

In general, O_3 production in a polluted environment begins with a hydrocarbon (RH) reacting with the hydroxyl radical (OH). Degradation of VOCs leads to the formation of reactive organic peroxy radicals (RO_2 or HO_2), which react with nitric oxide

(NO), converting NO to nitrogen dioxide (NO_2), which then photolyzes at $\lambda < 420$ nm to form O_3 [*Atkinson*, 2000; *Finlayson-Pitts and Pitts*, 2000; *Jacobson*, 2005; *Kleinman*, 1994; *Seinfeld and Pandis*, 2006].

$$RH + OH \rightarrow RO_2 + H_2O \quad (2.1)$$

$$RO_2 + NO \rightarrow RO + NO_2 \quad (2.2)$$

$$RO + O_2 \rightarrow R'O + HO_2 \quad (2.3)$$

$$HO_2 + NO \rightarrow OH + NO_2 \quad (2.4)$$

$$NO_2 + h\nu \rightarrow NO + O(^3P) \quad \lambda < 420 \text{ nm} \quad (2.5)$$

$$O(^3P) + O_2 + M \rightarrow O_3 + M \quad (2.6)$$

Alkoxy radicals (RO) produced by 2.2 are generally converted to OVOCs by rapid oxidation into carbonyls (R'O). Photolysis of O_3 at $\lambda < 310$ nm produces excited state atomic oxygen ($O^1(D)$) which can react with water vapor (H_2O) to form OH leading to a net loss in O_3 [*Atkinson*, 2000; *Finlayson-Pitts and Pitts*, 2000; *Jacobson*, 2005; *Seinfeld and Pandis*, 2006].

$$O_3 + h\nu \rightarrow O(^1D) + O_2 \quad (2.7)$$

$$O(^1D) + H_2O \rightarrow 2OH \quad (2.8)$$

In the presence of low NO (rural/"clean" environments), O_3 reacts with OH and HO_2 to form molecular oxygen with no radical loss, representing an additional loss mechanism for O_3.

$$O_3 + OH \rightarrow HO_2 + O_2 \quad (2.9)$$

$$O_3 + HO_2 \rightarrow OH + 2O_2 \quad (2.10)$$

Therefore, the ratio of production and loss of O_3 depends on mixing ratios of NO, HO_x ($OH+HO_2$), and RO_x ($RO+RO_2$) [*Atkinson*, 2000; *Jacobson*, 2005; *Kleinman*, 1994;

Lelieveld and Dentener, 2000; *Logan*, 1985; *Sillman et al.*, 1998]. More specifically, oxidation of organic compounds makes up a great deal of the total atmospheric chemical process. *Atkinson et al.* [2006] presents over 30 years of kinetics research on interactions between organics and OVOCs. Most of the products in these reactions produce additional organic compounds, which either photolyze or oxidize eventually becoming the simplest form of oxygenated VOC formaldehyde (CH_2O), CO_2, or O_3. *Atkinson* [1994] imparts exhaustive kinetics data for selected classes of gas phase organics, including alkanes [e.g., *Blanchard et al.*, 2010; *McKeen et al.*, 1997; *Riemer et al.*, 1998; *Russo et al.*, 2010], alkenes [e.g, *Ambrose et al.*, 2007; *Brown et al.*, 2009; *Hagerman et al.*, 1997; *Russo et al.*, 2010; *Sillman et al.*, 2002; *White et al.*, 2008], alkynes, aromatics [e.g., *Barro et al.*, 2009; *Blunden et al.*, 2005; *Filipy et al.*, 2006; *Jobson et al.*, 2004; *Riemer et al.*, 1998], and OVOCs [e.g., *Fried et al.*, 2008; *Herndon et al.*, 2007; *Sillman et al.*, 2002; *Wagner et al.*, 2001].

With all of this in mind, it is paramount to have a thorough understanding of the atmospheric concentrations of these compounds, particularly considering the rapid reaction and photolysis rates and variable nocturnal and diurnal processes.

b. Comparable Existing Standard Method

While it is beyond the scope of this Dissertation to outline every EPA Compendium Method, a thorough outline of relevant Compendia can be found in *Buckley* [2009] and a review by *Kumar and Viden* [2007]. However, understanding the comparable Compendium Method in the context of this research is essential. Compendium Method TO-15 [*EPA*, 1997] is a method instituted by the EPA to monitor VOCs. TO-15 uses specially prepared stainless steel canisters to collect ambient air

samples. Regional testing laboratories receive these canisters where the VOCs are preconcentrated on a solid multisorbent trap, dried, refocused onto a second trap, and analyzed using gas chromatography with mass spectroscopy (GC/MS) usually within 30 days of their arrival. Experienced lab technicians compare mass spectra to known library spectra in order to identify and quantify ambient compounds. This method is capable of monitoring both polar and non-polar VOCs including carbon tetrachloride, methyl chloride, and chloroform at detection limit ranges of 0.2-1.64 ppbv (see Table 3 in TO-15 for complete list of VOCs and their detection limits).

The EPA has thoroughly tested and extensively used the above standard method for several years at National Ambient Air Quality Standards (NAAQS) sites across the country. This method samples an extensive set of VOCs, because it takes advantage of sample drying combined with multisorbent trapping techniques. This technique also allows for a unique analysis of polar VOCs, something no previous EPA sampling method was capable of retrieving [*McClenny et al.*, 1995].

However, there are several disadvantages to TO-15. Labor-intensive sample handling at the collection sites, during shipment, and during analysis, as well as delays between sample collection and sample analysis, can cause sample degradation for many compounds of interest [*Batterman et al.*, 1998; *Doezema et al.*, 2010; *Kelly and Holdren*, 1995; *Kim et al.*, 2004; *Ochiai et al.*, 2002; *Pate et al.*, 1992]. Additionally, the co-collection of SO_2, NO_2, and other species with organic compounds might chemically alter the collected sample during storage in the short term (see R1-R4). The EPA states, "Chemical reactions between VOCs and substances inside the canister are generally assumed to cause the gradual decrease of concentration over time" [*EPA*, 1997].

Koppmann et al. [1995] studied different inlet configurations to address how O_3 affected low mixing ratio alkenes in laboratory mixtures. Inlet heating reduced initial O_3 mixing ratios by ~50%. Thermal desorption of the remaining O_3 in the presence of alkenes resulted in losses of ~10%. This desorption affect is minimal and well within the error range of TO-15.

Ochia et al. [2002] tested the effect of water vapor and condensed water on polar and non-polar VOC recovery in fused-silia lined (FSL) canisters and SUMMA canisters at low-ppbv levels. They found FSL canisters were "more inert" than the SUMMA canisters, with a recommendation of 53% humidity to maintain VOC stability, with good recoveries (> 80%) over 28 days for both types of canisters. The exception was thiol organosulfur compounds, which showed marked decreases over three days in FSL canisters and were unrecoverable in SUMMA canisters. The reader is referred to Table 2 in *Ochiai et al.* [2002] for full range of recovery values for 58 different VOCs.

Also, data latency is poor due to delays between sample collection and data delivery. Low temporal resolution with one 24-hour sample every sixth or twelfth day prevents rapid response to data anomalies and prevents quantification of critical chemical processes, many of which have reaction lifetimes much less than 24 hours. Finally, high life-cycle costs, including purchase, installation, and annual operation at the distributed sampling stations and processing laboratories makes this a high-cost method both short-term and long-term.

c. Real-Time GC

Many ambient air monitors use GC techniques to measure a wide range of VOCs [*Chang et al.*, 2010; *Helmig*, 1999]. Due to the wide range of detection methods possible

in GC such as flame ionization (FID) [e.g., *Ambrose et al.*, 2010; *Blunden et al.*, 2005; *Chang et al.*, 2010; *Jobson et al.*, 2010; *Park et al.*, 2010] and mass spectrometry (MS) [e.g., *Christian et al.*, 2004; *Filipy et al.*, 2006; *Jordan et al.*, 2010; *Legreid et al.*, 2007; *Miller et al.*, 2008; *Sive et al.*, 2005; *Su et al.*, 2008; *White et al.*, 2008], many groups use GC techniques, including University of New Hampshire (UNH), National Center for Atmospheric Research (NCAR), and Scripps Institute of Oceanography. These research groups developed real-time air quality monitors using GC/MS primarily because of its high sensitivity and excellent selectivity.

McClenny et al. [1984] first studied preconcentration as a possible solution to improving measurement sensitivity to monitor low-concentration VOCs. Two 0.32 cm O.D. nickel traps packed with 60-80 mesh Pyrex beads formed two identical enrichment traps. The traps wound onto cylindrical heaters and stainless steel shells housed the traps during sample collection. Liquid nitrogen cooled the traps from +120 ºC to -150 ºC in 225 seconds. Flow controllers maintained constant 4 mL/sec flow of specially prepared VOC standards. *McClenny et al.* [1984] introduced varying amounts of water vapor into the calibration samples and ran the mixture through Nafion dryers. The desorbed flow split in equal amounts to a GC coupled with both electron capture and flame ionization detectors (ECD/FID) to analyze desorbed samples.

Laboratory tests of this system resulted in collection and release efficiencies of 100 ± 5%, well within the experimental error range of ± 10%. Additionally, *McClenny et al.* [1984] found adding increasing amounts of ozone (0-300 ppbv) and nitrogen dioxide (0-250 ppbv) did not affect the calibration analytes (see Table III in *McClenny et al.* [1984]). Their results are not exhaustive, but are well within the error range of the

instrument and the calibration ranges well within expected atmospheric values. They also found using the Nafion driers in both dry and 50% humidity samples had no effect on the expected results, within the error of the instrumentation. This system served as the springboard for a number of rapid-response GC systems. *Haberhauer-Troyer et al.* [1999] have since shown Nafion driers to generate sampling artifacts when measuring trace VOCs.

NCAR developed the first GC/MS system considered in this review [e.g., *Apel et al.*, 2003a; *Apel et al.*, 2003b; *Apel et al.*, 2010; *Cantrell et al.*, 2003; *Dunlea et al.*, 2009; *Heald et al.*, 2008]. This system, outlined in *Apel et al.* [2003b], is an airborne fast response GC/MS (FGCMS) system used to sample several target organic VOCs, including acetaldehyde and carbon tetrachloride. Figure 1 in *Apel et al.* [2003b] outlines the FGCMS flow path. The system collects ambient air through an air inlet for in-flight sampling. The ambient sample flows through a series of pumps at 75 mL per minute (mLPM) toward the first trapping stage, the water removal trap. Liquid nitrogen (LN_2) cryogen along with an auxiliary heater maintains this trap at -15 °C during sampling. The dried sample then travels to an enrichment trap filled with silanized glass wool to trap the compounds of interest. The cryogenic system holds this trap at -120 ºC. During analysis, helium carrier gas directs the thermally desorbed sample into the cryofocusing trap, which is also held at -120 °C. Rapidly heating the cryofocusing trap desorbs the sample into the GC/MS column to collect chromatograms. This setup allows the FGCMS to collect 12 data samples every hour on a continuous basis for up to fifteen hours until the LN_2 cryogen is exhausted (180 chromatograms).

Field testing of this system finished in 2001 as part of the Transport and Chemical Evolution over the Pacific (TRACE-P) aircraft campaign [*Carmichael et al.*, 2003]. During that time, chromatograms of the targeted compounds, collected with five-minute temporal resolution, tested the robustness of this device. As configured during these missions, the FGCMS had compound-dependent detection thresholds of 5-75 pptv. Coincident measurements, collected by *Fried et al.* [2003], showed the utility of the FGCMS system as a rapid response monitoring system. However, this comparison also showed its shortcomings.

The primary limitation of the FGCMS system is its requirement of liquid cryogen. The difficult handling conditions and rapid consumption rates limit the continuous monitoring capabilities of this system. However, because this system is airborne, run times rarely exceed fifteen hours. The airborne tests found the integrated sample time changed as a function of altitude due to the changes in flow rate through the sample holding volume. These issues along with other instrument artifacts lead to a measurement uncertainty of ±15-20%.

The Scripps Institute of Oceanography developed another real-time GC/MS system [*Miller et al.*, 2008; *Weiss et al.*, 2008]. This system, called Medusa, uses cryogen-free preconcentration to monitor a set of 38 halocarbons, hydrocarbons, and sulfur compounds involved in the ozone photochemistry plus methyl chloride and benzene. Figure 1 in *Miller et al.* [2008] outlines the Medusa flow schematic. First, a sampling inlet collects the sample and channels it through two Nafion filters in series to dry the sample at a flow rate of 0.1 liters per minute (LPM). A high-purity divinylbeneze adsorbent maintained at -165°C preconcentrates the sample removing most of the volatile

compounds. Next, the trapped concentrate is desorbed into a second trap (Trap 2), containing the same adsorbent medium, to further remove the bulk air gases that can interfere with the MS analysis. Nafion 2 further dries the desorbed material prior to analysis by GC/MS. This system is capable of 24 measurements over a 24 hour period at ~1 pptv detection threshold, as determined by a year-long (~3600 samples) field validation campaign at Trinidad Head, CA.

This lengthy field validation process illustrates the utility of Medusa as a long-term, autonomous monitoring system. However, a few key design decisions could cause data problems. Nafion dryers have a high potential for artifact formation, primarily in the presence of hydrocarbons [*Haberhauer-Troyer et al.*, 1999]. Despite this artifact potential, *Miller et al.* [2008] developed Medusa to measure a list of 38 target analytes, 15 of which showed little to no effect when one or more Nafion filters are introduced into the flow stream.

Also, the use of a reactive solid adsorbent as the trapping medium can cause artifacts (by contrast *Apel et al.* [2003b] and later *Sive et al.* [2005] used silica trapping media, because they are inert and desorption is relatively efficient). Because Medusa monitors highly volatile compounds and halocarbons, a highly reactive absorbent surface is required. In an artifact study similar to the Nafion test in *Haberhauer-Troyer et al*. [1999], *Miller et al.* [2008] found 50% of the 38 compounds showed no detectable artifact contamination. Although the design decisions lead to some artifact generation, in order for Medusa to efficiently monitor the volatile compounds important to O_3 photochemistry, the system must employ reactive adsorbent media.

The final GC/MS system reviewed for this study was engineered by UNH [e.g., *Ambrose et al.*, 2007; *Jordan et al.*, 2010; *Russo et al.*, 2010; *Sive et al.*, 2005; *White et al.*, 2008; *Zhou et al.*, 2008]. This system also uses cryogen-free preconcentration with real-time GC/MS. Figure 2 in *Sive et al.* [2005] shows the UNH flow schematic. This system uses an inert collection medium (1 mm glass beads) to avoid sample artifacts during enrichment and desorption cycles, similar to the FGCMS system designed by NCAR [*Apel et al.*, 2003b]. This design decision allows the UNH system to measure an extensive list of 98 ambient VOCs, including acetaldehyde and isoprene, at a compound-dependent measurement uncertainty of ±0.3-15%.

The UNH GC/MS gathers an ambient sample and channels it into two traps. The first trap collects water vapor at -20 °C. Next, the cryotrap, maintained at -175 °C, enriches the sample for GC/MS analysis. This system is similar to *Apel, et al.* [2003b] with a few major exceptions. First, the cryotrap temperature is lower in the UNH GC/MS, due to their use of an efficient mechanical cryocooler rather than LN_2. Second, the trap collects and desorbs more efficiently, because UNH uses silanized glass beads rather than packed glass wool. The glass beads improve the collection and desorption processes by reducing the number of microcavities where analytes can remain trapped. Both of these improvements result in a larger number of detectable analytes at much lower detection thresholds.

The UNH system was run in parallel with two established monitoring methods, proton transfer reaction MS (PTR/MS) and whole air canisters [*Sive et al.*, 2005]. This validation process demonstrated good correlation between the UNH GC/MS and both the PTR/MS (r^2 = 0.92 – 0.95) and the whole air samples (r^2 > 0.92), which persisted even at

sub-pptv mixing ratios. Therefore, using cryogen-free preconcentration and inert, macroporous collection media yields improved ambient air measurements when compared to using liquid cryogens and chemically active microporous adsorbents.

All of the above methods have a wide range of capabilities, but their limitations still suggest an alternative method is desirable. This alternative method should 1) maintain high quantitative accuracy of better than 20%, measurement quality, and compound selectivity, 2) be easily automated without extensive sample handing and data manipulation, 3) improve temporal data resolution for applicability for air quality modeling and process studies, and 4) reduce both short-term operating costs and long-term life-cycle costs.

CHAPTER III

METHODOLOGY

a. FTIR Methodology

The Bouguer-Lambert-Beer Law (henceforth referred to as Beer's Law) is the fundamental concept used in quantifying measured IR transmittance spectra. Beer's Law states the transmittance, $T(\tilde{\nu})$, of radiation at wavenumber $\tilde{\nu}$ ($\tilde{\nu} = \frac{1}{\lambda}$) through a sample is the ratio of the radiance, $I(\tilde{\nu})$, at the gas cell exit to the radiance, $I_0(\tilde{\nu})$, at the entrance. Assuming a sample thickness of b [cm] in a non-scattering medium and ignoring scattering over the short path lengths used in the laboratory, Beer's Law for a single absorber is expressed as

$$T(\tilde{\nu}) = \frac{I(\tilde{\nu})}{I_0(\tilde{\nu})} = \exp[-\alpha'(\tilde{\nu})b] = \exp[-\sigma(\tilde{\nu})bc], \tag{3.1}$$

where $\alpha'(\tilde{\nu}) = \sigma(\tilde{\nu})c$ is the linear absorption coefficient in cm^{-1}, where $\sigma(\tilde{\nu})$ is the absorption cross section in cm^2 $molecule^{-1}$ and c is concentration in molecules cm^{-3}. Taking the $\log_{10}$ of Equation (3.1) converts transmittance to absorbance (for this dissertation, we will use absorbance in all cases base 10 for consistency with the Pacific Northwest National Laboratory (PNNL) absorbances for gases),

$$A(\tilde{\nu}) = \log_{10}\frac{1}{T(\tilde{\nu})} = \frac{1}{ln10}[\sigma(\tilde{\nu})bc]. \tag{3.2}$$

If the FTIR is sampling a complex mixture of M compounds at varying molecular concentrations, c_i and consequent varying absorbances, Equation (3.2) becomes,

$$A(\tilde{\nu}) = \sum_{i=1}^{M}[\sigma_i(\tilde{\nu})bc_i]. \tag{3.3}$$

Equation (3.3) serves as the basis of the quantification algorithm for the designed system.

Consider two spectra, one containing a calibration mixture of gases in N_2 (subscript 2) and one containing only N_2 (subscript 1), and using the same FTIR with the same settings to collect both spectra, ratioing of spectral radiance, $I_2(\tilde{\nu})/I_1(\tilde{\nu})$ from Equation (3.1) yields at each frequency

$$\frac{I_2}{I_1} = \frac{I_{2,0}}{I_{1,0}}\left(\frac{T_2}{T_1}\right)$$

$$\frac{I_2(\tilde{\nu})}{I_1(\tilde{\nu})} = \left\{\left(\frac{L_2(\tilde{\nu})}{L_1(\tilde{\nu})}\right)\left(\frac{a_2(\tilde{\nu})\Omega_2(\tilde{\nu})}{a_1(\tilde{\nu})\Omega_1(\tilde{\nu})}\right)\left(\frac{\eta_2(\tilde{\nu})}{\eta_1(\tilde{\nu})}\right)\left(\frac{G_2(\tilde{\nu})\Delta\tilde{\nu}_2\Delta t_2}{G_1(\tilde{\nu})\Delta\tilde{\nu}_1\Delta t_1}\right)\right\}\left(\frac{T_2(\tilde{\nu})}{T_1(\tilde{\nu})}\right), \tag{3.4}$$

where $L(\tilde{\nu})$ is the source radiance in W m^{-2} sr^{-1} m, $a(\tilde{\nu})$ is the detector area in m, $\Omega(\tilde{\nu})$ is the solid angle of the source beam through the FTIR in sr, $\eta(\tilde{\nu})$ is the optical efficiency in m^2 sr^{-1}, $G(\tilde{\nu})$ is the detector gain in dB, $\Delta\tilde{\nu}$ is the wavenumber resolution in m^{-1}, and Δt is the signal integration time in sec. The bracketed terms in Equation (3.4) cancel except for only very minor fluctuations in optical efficiency, source radiance, and trace-gases in the external optical path. Therefore, applying Equation (3.4) to Equation (3.2) yields for a single species,

$$A_{1,2}(\tilde{\nu}) = -\ln\left(\frac{I_2(\tilde{\nu})}{I_1(\tilde{\nu})}\right) = -\ln\left(\frac{T_2(\tilde{\nu})}{T_1(\tilde{\nu})}\right) + \boldsymbol{K_{1,2}}(\tilde{\nu}), \tag{3.5}$$

where $\boldsymbol{K_{1,2}}(\tilde{\nu})$ is the residual error matrix, which is minimized operationally.

Finally, since absorbance is proportional to concentration and the path length of the gas cell, the general form of Equation (3.5) becomes,

$$A_{1,2}(\tilde{\nu}) = \\ b\sum_i\{c_i(T_2,P_2)\sigma_i(\tilde{\nu}_2,T_2,P_2) - c_i(T_1,P_1)\sigma_i(\tilde{\nu}_1,T_1,P_1)\} + \tag{3.6}$$

$$\boldsymbol{K_{1,2}}(\tilde{\nu}).$$

Equation (3.6) relates the measured absorbance for the i^{th} compound to the concentration of the i^{th} compound and the wavenumber-specific absorption cross section of the i^{th} compound, as a function of temperature T and pressure P. This fundamental relationship makes absorption spectroscopy, specifically FTIR, an effective analytical tool capable of monitoring complex mixtures of IR-active gases with detection limits dependent upon the analytical set up (i.e., spectral resolution, temporal resolution, gas cell path length, detector optics, availability of accurate photoabsorption cross sections measure at various temperatures and pressures, and electronic stability).

Research over the years has shown concentrations of VOCs can vary from sub-pptv levels for biogenic VOCs in rural environments [e.g., *Kim et al.*, 2010; *Warneke et al.*, 2010] to mid-ppbv levels near heavy pollution sources, such as power plants and automobiles [e.g., *Peischl et al.*, 2010; *Zaveri et al.*, 2010]. Therefore, it is desirable to design an analytical device capable of measuring these ranges for a number of VOC species. Applying Equation (3.6) to extractive FTIR methodology such as that found in EPA Method 320 [*EPA*, 1999] using a spectroscopically transparent gas (e.g., N_2) and eliminating absorbing gases from the background spectrum simplifies the expression to

$$A_{1,2}(\tilde{\nu}) = b\sum_i\{c_i(T_2,P_2)\,\sigma_i(\tilde{\nu},T_2,P_2)\} + \boldsymbol{K_{1,2}}(\tilde{\nu}). \quad (3.7)$$

Extractive FTIR methods such as EPA Method 320 [*Cantu et al.*, 1998; *EPA*, 1999] remove the dependence on the background spectrum (subscript 1 in Equation (3.6)) by collecting an evacuated background, thus eliminating interference by H_2O and CO_2 in the background spectrum and reducing the temperature and pressure dependence of the methodology. However, with no method to remove H_2O and CO_2 from the actual sample

spectrum (subscript 2 in Equation (3.6)) [*NIOSH*, 2003] these major spectroscopic interferents reduce the accuracy of the calculation and make key spectral windows unavailable for analysis. Additionally, trace-gas absorption cross sections are so small in the IR low detection limits require long co-addition times and long optical path lengths. These constraints make real-time extractive monitoring nearly impossible, except in highly polluted conditions. Even with these compromises, extractive FTIR has difficulty achieving the low detection limits of GC with preconcentration.

The work that comprised this Dissertation utilizes the advantages of extractive FTIR in combination with cryogen-free low-temperature pre-concentration to reduce detection limits closer to 'clean' ambient mixing ratios. Incorporating cryogenic pre-concentration in extractive FTIR introduces a "pre-concentration" term to Equation (3.7);

$$A_{1,2}(\tilde{\nu}) = b_{cell}\left(\frac{F_{trap}\Delta t_{trap}}{V_{cell}}\right)\sum_i\{c_i(T_2,P_2)\,\sigma_i(\tilde{\nu},T_2,P_2)\} + \boldsymbol{K_{1,2}}(\tilde{\nu}), \tag{3.8}$$

where b becomes b_{cell} which is the path length of the gas cell (1000 cm in this case), F_{trap} is the flow rate through the cryogenic trap in standard cubic centimeters per minute (sccm), Δt_{trap} is the residence time in the cryogenic trap in minutes, and V_{cell} is the volume of the gas cell in cm^3 (2000 cm^3 in this case). Equation (3.8) shows the total absorption within the spectral range is due to the additive affect of all absorbers within the gas cell. Assuming a single absorbing species, solving Equation (3.8) for *c*, and rearranging to group like terms illustrates how pre-concentration reduces the minimum detectable concentration within the wavenumber range

$$c_i(T_2,P_2) = \left(\frac{A_i(\tilde{\nu})}{\sigma_i(\tilde{\nu},T_2,P_2)}\right)\left(\frac{V_{cell}}{b_{cell}}\right)\left(\frac{1}{F_{trap}\Delta t_{trap}}\right) - \boldsymbol{K_{0,1}}(\tilde{\nu}). \tag{3 9}$$

The reduced detection limits along with the advantages listed in Table 3.1 make

Table 3.1. Comparison of the advantages and disadvantages between FTIR and GC/MS with preconcentration. The advantages are in the unshaded cells. The disadvantages are in the shaded cells.

Feature	FTIR	GC-MS
Molar Sensitivity	relatively low	relatively high
Chemical Separation	not required	required (adsorbent columns)
Analysis Method	one method for all analyte types	column type must match analyte type
Analysis Domain	spectral (wavelength)	temporal (retention time)
Co-Addition (*i.e.*, Integration)	inherent in the method, improves sensitivity	usually not feasible
Chemical Fingerprints	(a) absorption band positions do not vary with pressure and temperature in the cell (b) absorption band widths vary only weakly with pressure and temperature in the cell (c) 1.0 cm^{-1} resolution, narrow linewidths, and multiple spectral features reduce line overlap for analyte detection.	(a) baseline, peak elution time and elution profile can vary with column pressure, temperature, condition (contamination or damage) (b) a given analyte has only one elution peak; multiple analytes may have overlapping peaks, some of which cannot be distinguished by MS analysis
Purchase Cost	relatively low	relatively high
Maintenance	infrequent, inexpensive	can be frequent, expensive
Primary Consumables	UHP dry helium	UHP helium, hydrogen, LN_2

extractive FTIR with inert cryogenic preconcentration a desirable methodology for monitoring ambient trace organics.

b. Noise Sources in FTIR

As mentioned above, the bracketed terms in Equation (3.4) do not perfectly cancel in the real world. In reality, photon fluctuations and thermal influences in the detector (receiver) and electronics add noise to the interferogram prior to Fourier conversion; variations in source intensity (radiance) multiplies the noise; mechanical vibration adds noise depending on the derivative of the vibration; temperature variations in the gas cell change the refractive index of the sample; and non-linearities in the detector add higher powers to the interferogram [*Brault*, 1985; *Davis et al.*, 2001; *Griffiths and deHaseth*, 2007; *Hirschfeld*, 1979]. When transformed, an idealized interferogram of monochromatic radiation does not produce a spectral line of zero width, but a delta function, $\delta(x)$, convolved with a sinc function, $sinc(x)$, and a rectangular function, $\prod(x)$. In theory $\delta(x)$ requires infinite spectral resolution to resolve; however, this is not practical in the real world.

Assuming a monochromatic interferogram, the interferogram as a function of the optical path difference x between two beams is given by

$$I(x) = \cos(2\pi\tilde{\nu}_0 x). \tag{3.10}$$

Because the path length, b, is finite, it is similar to taking an infinitely long interferogram and truncating it using the rectangular function, $\prod(x)$

$$I_{obs}(x) = I(x) \cdot \Pi\left(\frac{x}{2b}\right). \tag{3.11}$$

Taking the Fourier transform of Equation (3.11) convolves the spectral signal with the sinc function

$$B_{obs}(\tilde{\nu}) = B(\tilde{\nu}) \star 2bsinc(2b\tilde{\nu}), \tag{3.12}$$

where $2bsinc(2b\tilde{\nu})$ represents the instrument function, $O(\tilde{\nu})$. This convolution produces ringing in the interferogram, typically suppressed using apodization, which reduces ringing at the high and low ends of the interferogram resulting in truncated spectral range [*Harris*, 1978; *Lee and Comisarow*, 1987]. Apodization reduces the SNR by degrading spectral resolution.

For radiation departing from the source to traverse through the interferometer requires a finite aperture. This finite aperature generates both on- and off-axis light. The off-axis path difference at angle α is $xcos(\alpha)$ and the interference intensity becomes

$$dI = \cos(2\pi\tilde{\nu}xcos(\alpha))\, d\Omega, \tag{3.13}$$

where $d\Omega$ is the incremental solid angle at α. The small angle approximation reduces Equation (3.13) to

$$dI = \cos\left(2\pi\tilde{\nu}x\left[1 - \frac{\alpha^2}{2}\right]\right) d\Omega. \tag{3.14}$$

Integrating over the aperture and equating $\Omega = \pi\alpha^2$ for a circular aperture

$$I(x) = \int_0^{\Omega_m} dI = \int_0^{\Omega_\mathrm{m}} \cos\left(2\pi\tilde{\nu}x\left[1 - \frac{\Omega}{2}\right]\right) d\Omega$$

$$I(x) = \Omega_m sinc\left(\frac{\tilde{\nu}x\Omega_m}{2\pi}\right) \cos\left(2\pi\tilde{\nu}x\left[1 - \frac{\Omega_\mathrm{m}}{4\pi}\right]\right). \tag{3.15}$$

The finite aperture has introduced a significant scale change [*Davis et al.*, 2001] and has multiplied the interferogram by the sinc function.

Additionally, *Anderson and Griffiths* [1975] found the finite resolution of a Fourier Transform spectrometer to be a source of noise. Assuming a Lorentzian line shape and either triangular apodization or zero apodization with a 4 cm^{-1} wide absorption band and spectral resolution of 2 cm^{-1}, the apodization reduces measured peak

absorbance by 16% compared to the Beer's-Law-derived theoretical absorbance. *Anderson and Griffiths* [1975] postulate this discrepancy results from the apodization beginning slightly beyond the actual zero optical path difference of the interferometer. Thus, the true apodization function becomes trapezoidal rather than triangular. The distance between the zero optical path difference and the actual starting point of the apodization function is independent of resolution. However, these effects are most prevalent at low resolution (> 4 cm^{-1}). Therefore, measuring at higher resolution will circumvent these effects.

Finally, mechanical vibration results in noise on the order of the time rate of change of the vibration itself during the interferometer mirror scan. The most dramatic vibrations are those with frequencies near the natural frequency of the FTIR instrument case and the interferometer within the case. When performing FTIR analysis ideally the spectrometer would be placed on a vibration-dampening optical bench housed within an electromagnetic/radio frequency interference (EMI/RFI) dampening enclosure. In field observations, the former method is impractical and expensive while the later is feasible and inexpensive.

c. Quantitative Methodology and Analysis

Solving Equation (3.3) for c_i and setting $b = b_{cell}$

$$\sum_i c_i = \frac{1}{b_{cell}} \sum_i \frac{A_i(\tilde{\nu})}{\sigma_i(\tilde{\nu})} \tag{3.16}$$

yields the ambient concentration of the i^{th} analyte. Introducing a preconcentration factor yields Equation (3.17);

$$\sum_i c_i = \frac{1}{b_{cell}} \left(\frac{V_{cell}}{F_{trap} \Delta t_{trap}} \right) \sum_i \frac{A_i(\tilde{\nu})}{\sigma_i(\tilde{\nu})}, \tag{3.17}$$

where V_{cell} is the gas cell volume in cm^3, F_{trap} is the trap flow rate in sccm, and Δt is the trap retention time in minutes. This enrichment factor makes this preconcentration method desirable. In the case of Phoenix, $V_{cell} = 2000\ cm^3$, $F_{trap} = 2000\ sccm$, and $\Delta t_{trap} = 240\ minutes$, resulting in an enrichment factor of 240, decreasing the minimum detection range by 4.2 x 10^{-3} when compared to flow into the gas cell without preconcentration.

At the ambient inlet,

$$C_{amb}F_{amb} + C_{VOC}F_{VOC} = C_{trap}F_{spike}, \tag{3.18}$$

where C_{amb}, C_{VOC}, and C_{trap} are the concentrations of the ambient, VOC calibration spike, and trap inlet components in cm^{-3} and F_{amb}, F_{VOC}, and F_{spike} are the flowrates of the ambient, VOC calibration spike, and spiked trap inlet components in sccm. Rearranging and solving for C_{amb},

$$C_{amb} = \frac{C_{trap}F_{spike} - C_{VOC}F_{VOC}}{F_{amb}}$$

$$C_{amb} = \frac{C_{trap}(F_{amb} + F_{VOC})}{F_{amb}} - \frac{C_{VOC}F_{VOC}}{F_{amb}}$$

$$C_{amb} = C_{trap}\left(1 + \frac{F_{VOC}}{F_{amb}}\right) - C_{VOC}\frac{F_{VOC}}{F_{amb}} \tag{3.19}$$

$$\sum_i C_{i,amb} = \left(\sum_i \frac{A_i(\tilde{\nu})}{\sigma_i(\tilde{\nu})}\right)\frac{1}{b_{cell}}\left(\frac{V_{cell}}{F_{trap}\Delta t_{trap}}\right)\left(1 + \frac{F_{VOC}}{F_{amb}}\right) - C_{VOC}\frac{F_{VOC}}{F_{amb}}. \tag{3.20}$$

Equation (3.20) gives the concentration following a full trapping sequence. Term 1 combines the measured absorbance in base 10 with the absorption cross section deduced

from the Pacific Northwest National Laboratory's (PNNL) IR Database [*Sharpe et al.*, 2004]. All other terms are constant or monitored by Phoenix in real time.

For continuous flow through the gas cell without preconcentration, the compound concentration C_{cell} in the flowstream $F_{celltotal}$ entering the gas cell are the same as the concentration in the flowstream entering the trap C_{trap}, except for a correction term from an adjustable dilution flow of cryopurged clean, dry air $F_{dilution}$ with concentration $C_{dilution}$

$$C_{trap}F_{spikedcell} + C_{dilution}F_{dilution} = C_{cell}F_{celltotal}.$$

Rearranging,

$$C_{trap}(F_{celltotal} - F_{dilution})$$

$$= C_{cell}F_{celltotal} - C_{dilution}F_{dilution}$$

$$C_{trap} = C_{cell}\frac{F_{celltotal}}{(F_{celltotal}-F_{dilution})} - C_{dilution}\frac{F_{dilution}}{(F_{celltotal}-F_{dilution})}.$$

Since $C_{dilution} = 0$, the relationship between continuous flow concentrations through the gas cell and the trap inlet becomes,

$$C_{trap} = C_{cell}\frac{F_{celltotal}}{(F_{celltotal}-F_{dilution})}. \quad (3.21)$$

Combining Equations (3.21) and (3.19) yields the continuous flow concentration,

$$C_{amb} = C_{cell}\frac{F_{celltotal}}{(F_{celltotal} - F_{dilution})}\left(1 + \frac{F_{VOC}}{F_{amb}}\right) - C_{VOC}\frac{F_{VOC}}{F_{amb}}$$

$$C_{amb} = C_{cell}\frac{1}{\left(1 - \frac{F_{dilution}}{F_{celltotal}}\right)}\left(1 + \frac{F_{VOC}}{F_{amb}}\right) - C_{VOC}\frac{F_{VOC}}{F_{amb}}$$

$$C_{amb} = C_{cell}\frac{\left(1+\frac{F_{VOC}}{F_{amb}}\right)}{\left(1-\frac{F_{dilution}}{F_{celltotal}}\right)} - C_{VOC}\frac{F_{VOC}}{F_{amb}}.$$

Substituting in Beer's Law from Equation (3.16),

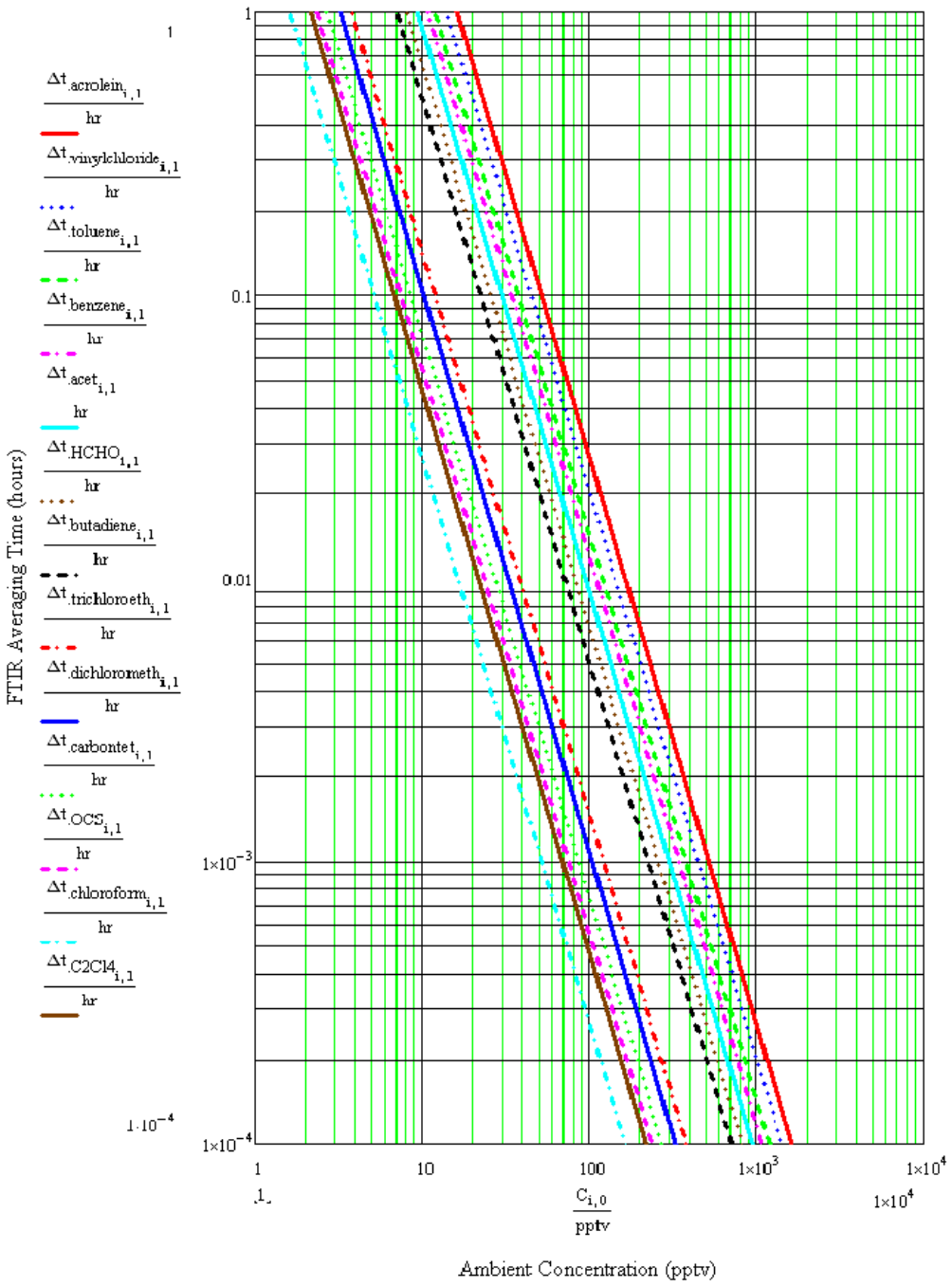

Figure 3.1. FTIR co-addition time in hours versus minimum detectable mixing ratio in pptv for Phoenix on a log-log scale. The FTIR averaging time for Phoenix is five minutes (0.08 hours) as indicated by the red horizontal line. If the detection limits are the same, the MDL of the second compound is reduced by 15% for graphical clarity (vinyl chloride, acetaldehyde, 1,3-butadiene, and OCS).

$$\sum_i C_{i,amb} = \sum_i \frac{A_i(\tilde{\nu})}{\sigma_i(\tilde{\nu})} \frac{1}{b_{cell}} \frac{\left(1+\frac{F_{VOC}}{F_{amb}}\right)}{\left(1-\frac{F_{dilution}}{F_{celltotal}}\right)} - C_{VOC}\frac{F_{VOC}}{F_{amb}}. \quad (3.22)$$

Equation (3.22) gives the concentration during continuous flow sampling. Term 1 is the same as Term 1 in Equation (3.20). All other terms are either constant or monitored by Phoenix in real time.

We used Equation (3.20) to calculate minimum detection limits (MDLs) for Phoenix using a preconcentration time of four hours (240 minutes), and a total-flow volume through the trap of 480 liters. As mentioned previously, the enrichment factor is 240. Assuming a possible analyte concentration range of 1 - 10^6 pptv and non-preconcentration MDLs ranging from 6 – 60 pptv, the preconcentrated MDLs decrease significantly, as shown in Figure 3.1.

d. Linear and Non-linear Least Squares Regression Analysis

The ideal quantitative method for Phoenix would utilize a linear least squares regression based on a complete set of library spectra that fully represent the molecules being measured. However, due to the time constraints of this research, the complex linear least squares algorithm could not be developed to properly explore this technique. This section outlines the background methodology of least squares regression analysis as it pertains to several methods, including spectral subtraction, classical least squares (CLS) and partial least squares (PLS) regression analysis, and non-linear least square methods, and how these different methods could be applied to the final Phoenix quantitative algorithm.

With the availability of high-spectral-resolution, low-noise library spectra [*Rothman et al.*, 2009; *Sharpe et al.*, 2004], an operator can sequentially subtract these pure spectra from an observed spectrum until all that remains is noise in the residual

spectrum. While not ideal, since spectral subtraction does not use the full amount of information available across the entire observed spectral range and cannot handle the wavelength-dependent cross correlation of the molecular photoabsorption spectral patterns resulting from the ambient gas mixture, this method can be effective if large peaks in absorption occur from single molecular species, i.e., where the molecular cross sections and abundances generate enough absorbance to show separated peaks of single molecules. To obtain the best results using this method, the quantitative process should select spectral regions where the features of a particular reference compound dominate all other compounds in the region. Following the collection of observed spectra, the operator interactively subtracts each compound, systematically reducing the complexity of the observed spectrum. However, this process can be time-consuming and requires a good deal of skill and experience, and produces a product inferior to spectral analysis using the entire wavelength range where molecules exhibit differential structured cross sections. For best results using spectral subtraction, the observed spectrum should be high enough resolution to not alias spectral features and the frequency and phase shifts between the observed and reference spectrum should be corrected [*Bacsik et al.*, 2004].

To produce a best fit using linear regression for the data collected by Phoenix, a plot of absorbance versus concentration of a single species would assume the form of a straight line, assuming absorbance is small (< 15% base e)

$$A(\tilde{\nu}) = mC + d, \tag{3.23}$$

where m is the slope of the best fit line and d is the intercept. Ideally d would be zero; however, that is unrealistic when analyzing complex gas-phase mixtures, possibly

because of optical interference or reflection loss. While multivariate analysis seeks to minimize error in measured data, it is unlikely any dataset lie perfectly on a straight line. A more accurate approach would be to measure the square of the distance from each measurement point perpendicular to the modeled straight line and to minimize the sum of the squares of all the distances [*Griffiths and deHaseth*, 2007]. The following section describes the basics of linear and non-linear least squares regressions. *Haaland and Easterling* [1982], *Haaland and Thomas* [1988a], and *Thomas and Haaland* [1990] contain detailed mathematical analysis and application which we will utilize during future work.

Linear least squares regression is a univariate technique, meaning a single dependent variable attributes all the variance in the regression. In the case of Fourier Transform spectroscopy, the dependent variable is spectral absorbance and the independent variable is concentration. This approach poses certain limitations. First, the absorbance at a single wavelength must relate to a single component only (i.e., no overlapping spectral features, which is unrealistic). Second, linear least squares regression best applies to simple mixtures with no overlapping spectral features, but this is also unrealistic and least squares regression analysis does provide the most comprehensive and accurate method of handling these common issues. These issuses pose a problem in the case of Phoenix, because it is not monitoring sample mixtures, rather it is monitoring a hopelessly convoluted medium, the atmosphere.

Therefore, the ideal way to apply linear least squares regression with Phoenix is to apply a full spectral range fit to minimize spectral residuals from all species

simultaneously.[1] Analytical software can construct a linear least squares regression for more than one component if it modifies Beer's Law to recognize measured absorbance as the sum of the absorbances of all the components in the mixture generating a multivariate regression model. CLS and PLS are two such statistical evaluation methods for use with multivariate data. CLS is the simplest of the multivariate least squares methods, primarily because it is based directly on Beer's Law [*Bacsik et al.*, 2004; *Haaland and Thomas*, 1988a]. Basically, CLS fits a linear combination of single-component library spectra by varying concentration to the observed spectrum such that the sum of the squares of the residual (SSR) spectrum is minimized. Assuming two components, *x* and *y*, contribute to a measured mixture and those components have spectral overlap, the absorbances at two unique wavenumbers are

$$\begin{aligned} A_{\widetilde{\nu_1}} &= k_{x_{\widetilde{\nu_1}}} C_x + k_{y_{\widetilde{\nu_1}}} C_y + E_{\widetilde{\nu_1}} \\ A_{\widetilde{\nu_2}} &= k_{x_{\widetilde{\nu_2}}} C_x + k_{y_{\widetilde{\nu_2}}} C_y + E_{\widetilde{\nu_2}}, \end{aligned} \tag{3.24}$$

where k is the absorption cross section times the pathlength and C is the component-specific concentration. The E terms represent the residual error inherent in a linear least squares method. Equation 3.24 has two known quantities and four unknowns, the k terms.

To apply this methodology to a linear least squares regression model, multiple concentrations of components *x* and *y* are chosen to produce a good fit. The two-component mixture in Equation 3.24 becomes a complex matrix of many different compounds

$$\boldsymbol{A} = \boldsymbol{K} \cdot \boldsymbol{C} + \boldsymbol{E}, \tag{3.25}$$

where $\boldsymbol{A}$ represents all the absorbance values at the any number of wavelenghts, $\boldsymbol{K}$ is the

[1] Personal Communication with George Mount, 2011

absorption coefficients, $\boldsymbol{C}$ is the concentrations of the components in each mixture, and $\boldsymbol{E}$ is the residual error for each measurement. In general, the algorithm should contain all components of the observed spectrum to optimize performance. See *Esler et al.* [2000a; 2000b] for application of CLS on observations of CO_2, CH_4, N_2O, CO, and $^{13}C/^{12}C$ isotope ratio of CO_2 in air.

Prior to application with complex, unknown mixtures, the model must evaluate $\boldsymbol{K}$ matrix. Removing the $\boldsymbol{E}$ matrix for simplicity and solving Equation 3.25 for $\boldsymbol{K}$ produces

$$\boldsymbol{K} = \boldsymbol{A} \cdot \boldsymbol{C}^{-1}. \tag{3.26}$$

The multivariate advantage of CLS over linear least squares regression techniques removes the need to have non-overlapping spectral features, although the extent of the overlap and the cross correlation coefficient between molecular cross sections will affect the errors assigned to the derived concentration. Another advantage is the use of the entire spectral range over which the molecule has a differential (structured) absorption cross section, which presents a better fit between the calibration-generated model and the measured spectrum producing a minimized residual spectrum.

If the CLS model is missing a single compound in the observed mixture and that compound contributes to the absorption of another compound at a particular wavenumber (i.e., overlaps), the derived concentrations for all calculated compounds will have increased error bars, but the spectrum of the missing compound should show itself clearly in the residual spectrum if the noise is low enough. Additional disadvantages include chemical reaction within the sample which will complicate the observed spectral mixture of the pure components used in the model and will cause the model to produce a large residual spectrum containing unknown compounds, unless the reaction products are part

of the calibration library matrix; the concentrations of the components used to build the model must be random to capture all the possible concentrations in the measured sample (i.e., if the concentration is higher or lower than those used in the model, the CLS will fail unless the system is completely linear which is unrealistic); and if the spectral ranges are not selected judiciously, the model will produce erroneous measurements if any of the cross sections of the calibration mixtures are linearly related, which frequently occurs, especially in the IR due to the intrinsic widths of the spectral features of VOCs. Different spectral regions are often used to analyze for different molecular species

Second, we consider the PLS regression method [*Dayal and MacGregor*, 1997; *Wold et al.*, 2001]. PLS, like CLS, is a full-spectrum method and fits a combination of reference spectra to an observed spectrum. The first step is to create a series of mixture spectra spanning the range of natural ambient concentrations. The algorithm performs factor analysis on the reference spectra (training) to generate a linear combination of the factor spectra weighted by a score for each factor. For application with an unknown mixture (e.g., the atmosphere), the PLS algorithm fits the observed spectrum as a combination of the factors derived during from the training and the concentration of each component (calibration) is calculated from the fitted factors and the scores of the second linear regression [*Bacsik et al.*, 2004]. Application of this methodology can be found in *Mattu et al.* [1997] and *Haaland and Thomas* [1988b].

Although computationally and mechanically labor intensive, the PLS method combines the strengths of CLS, which provides full spectral coverage and improves the analysis precision while providing the capability to model specific components in each analyzed sample. PLS is robust enough to analyze very complex gas-phase mixtures (e.g.,

the atmosphere). The shortcomings are minor and include slow calculations speed (irrelevant using high-speed, quad-core processor), and PLS requires a large number of mixture spectra to yield a highly precise regression model.

Beer's law goes non-linear when I/I_0 is less than 0.85 [e.g., *Philpotts et al.*, 1951] and that non-linearity grows exponentially with increasing absorbance. To extend retrievals into high-absorption conditions where this non-ideality is important, a number of observational techniques apply non-linear least sqaures (NLLS) methods to quantify observed spectra. *Stutz and Platt* [1996] and *Spinei et al.* [2010] use a combination of linear fitting and a low-order polynomial fit to account for broadband molecular scattering (Rayleigh ($\text{diameter}_{\text{scatter}} << \lambda_{\text{light}}$) and Mie ($\text{diameter}_{\text{scatter}} > \lambda_{\text{light}}$)) in total column measurements of O_3, NO_2, SO_2, and CH_2O, although absorbances from scattering in the relatively short length of a laboratory cell are generally ignored. These scattering features exhibit slow variations in extinction with wavelength, and they change only a small amount over the typical wavelength interval used in *Stutz and Platt* [1996] and *Spinei et al.* [2010]. For Phoenix, scattering changes exhibit a much larger dynamic range than the cited studies, but the wavelengths involved are long enough to reduce the significance of either type of scattering. Additionally, Phoenix uses a filter to remove aerosols from the ambient sample, eliminating interference from Mie scattering. Therefore, a combination of linear least squares and NLLS would be the best analytical methodology for Phoenix. Ultimately, the Phoenix quantitative algorithm will implement these advanced retrieval techniques.

CHAPTER IV

INSTRUMENTATION

a. ECIP-FTIR Methodology

The University of Alabama in Huntsville (UAHuntsville) has developed a near-real-time trace-gas sensor with initial support from the Jefferson County Department of Health (JCDH) in Birmingham, AL, and Region IV of the EPA in Atlanta, GA, with continued support from the National Oceanic and Atmospheric Administration (NOAA) National Environmental Satellite, Data, and Information Service (NESDIS). The UAHuntsville sensor uses a commercial FTIR spectrometer (Bruker Optics Tensor 27; Billerica, MA), a commercial long-path infrared (IR) gas cell (Gemini MARS 10L/2M; Buena Park, CA), a commercial acoustic Stirling cryocooler (Clever Fellows Innovation Consortium (CFIC) QDrive 2S102K; Troy, NY), and a custom cryogen-free cryotrap to obtain autonomous measurements of a suite of VOCs, with special emphasis on the target analytes listed in Table 4.1. Figure 4.1 shows the spectral peaks for each target analyte.

Every 15 minutes, Phoenix records a trace gas absorption spectrum and the derived trace gas mixing ratios, using continuous non-preconcentrated sample flow through the gas cell, to achieve compound-specific detection limits of ~10 ppbv. Every four hours, the FTIR and gas cell obtain similar data on preconcentrated batch samples that have been thermally desorbed from the cryotrap to improve compound-specific detection limits to 6-60 pptv.

Table 4.1. Listing of Phoenix target analytes in order of molecular weight. The EPA MDLs are from EPA 40 CFR Part 58. N/A means not listed by this document. The Phoenix MDLs are derived from Figure 3.1. The melting point temperatures are from Figure 4.7.

Target Analyte	Symbol	EPA MDL (ppbv)	Phoenix MDL (ppbv)	Spectral Peak (cm^{-1})	Abs. Cross Section (cm^2 $molec^{-1}$)	Melting Point (°C)
Formaldehyde	CH_2O	0.020	0.028	1121	2.40E-20	-117.0
Acetaldehyde	CH_3CHO	0.010	0.039	1103	3.20E-20	-123.5
1,3-butadiene	C_4H_6	0.070	0.030	908	4.80E-19	-108.9
Acrolein	C_3H_4O	N/A	0.060	959	1.41E-19	-88.0
Carbonyl sulfide	OCS	N/A	0.008	868	2.80E-20	-139.0
Vinyl chloride	CH_2CHCl	0.060	0.060	942	3.43E-19	-154.0
Benzene	C_6H_6	0.040	0.038	674	2.42E-18	5.5
Dichloromethane	CH_2Cl_2	0.060	0.012	750	3.34E-19	-96.7
Toluene	C_7H_8	0.050	0.030	3042	9.00E-20	-93.0
Chloroform	$CHCl_3$	0.050	0.009	772	1.08E-18	-63.5
Trichloroethylene	C_2HCl_3	0.070	0.014	851	4.35E-19	-73.0
Carbon tetrachloride	CCl_4	0.080	0.009	795	2.14E-18	-22.9
Tetrachloroethylene	C_2Cl_4	0.052	0.006	916	5.72E-19	-19.2

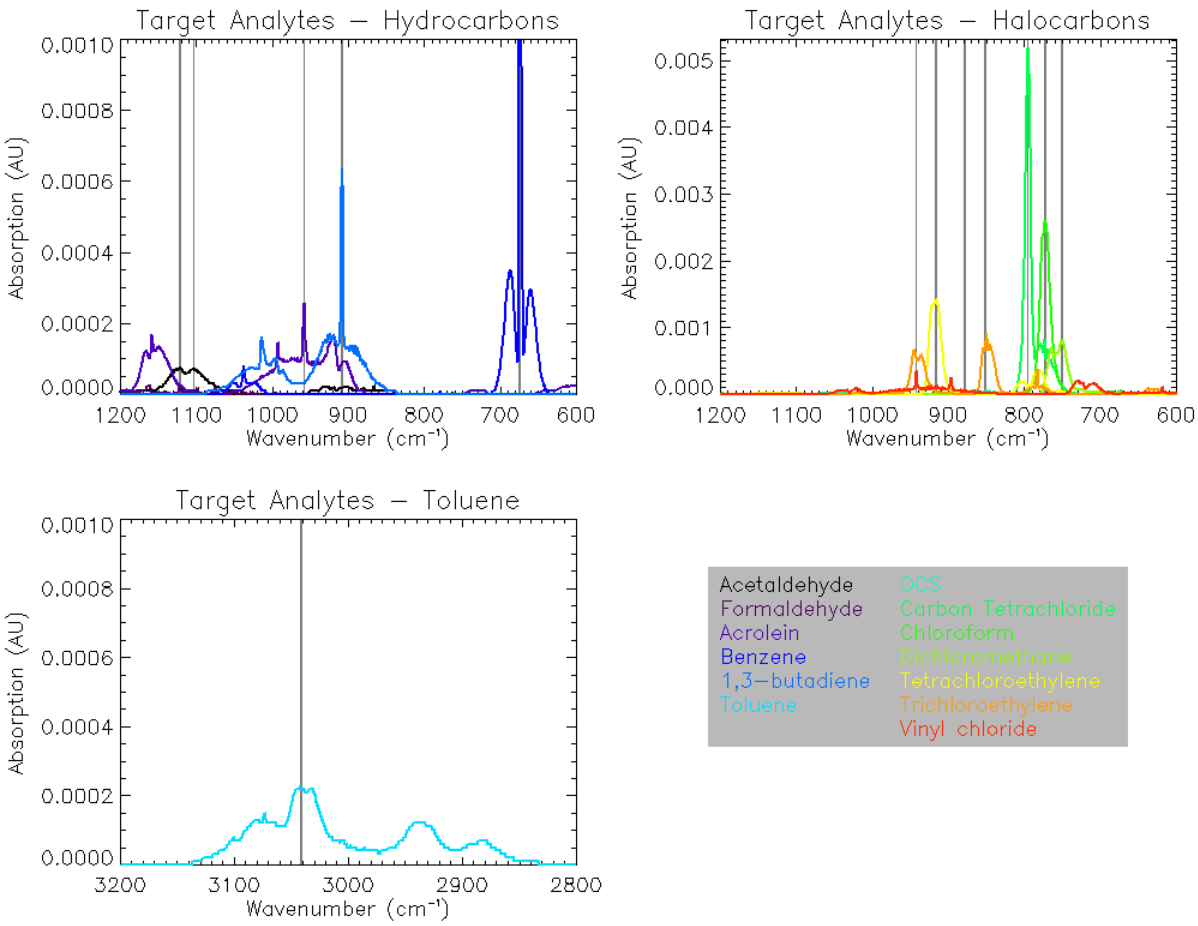

Figure 4.1. IR spectra for each target analyte derived from *Sharpe et al.* [2004]. The grey vertical lines represent the spectral ranges used for quantification of each compound in the quantitative algorithm. Refer to Table 4.1 for exact wavenumber locations of each spectral feature.

The Phoenix flow diagram has multiple pathways as shown in Figure 4.2. A series of multiport stepper valves (Valco Instruments Company, Inc., Houston, TX) selects each flow path depending on the desired mode of operation. These two-position switching valves and multi-position stream-selection valves can isolate or disable selected elements of the fluid system or run them in parallel.

Ambient air (blue trace) is introduced into the system at the inlet filter (F_{amb}). Immediately following insertion into the fluid system, two in-line traps collect H_2O and CO_2 to remove these strong interferents from the analytical system. The first trap is a 0.635 cm OD x 0.55 cm ID x 152.4 cm trap placed inside a small freezer to trap H_2O vapor. The freezer holds the trap at -2 °C and collects ambient H_2O vapor. The trap is manually desorbed daily to remove the condensate. Phoenix uses this method for availability, simplicity, and trapping efficiency. The second trap is a 0.635 cm OD x 0.55 cm ID x 15.2 cm trap filled with Ascarite (sodium hydroxide coated silicate) to trap CO_2. Phoenix uses this material for availability and adsorption efficiency (up to 1 ppmv removal). Comparing an untreated ambient air sample and a trapped sample in continuous flow mode shows a clear reduction in both H_2O and CO_2 concentration of 82% and 33%, respectively (see Figure 4.3 for resulting spectra). However, this is not an idealized and optimized set up, and additional research will be required to optimize this functionality.

Once the ambient sample is treated it splits into two flow paths. The first is the continuous flow path shown in the lower portion of Figure 4.2. The ambient sample travels through a mixer fed by a high-purity Metal Bellows pump (Senior Aerospace

Table 4.2. Comparison between EPA Method TO-15 and Phoenix. Yellow rows highlight the most critical differences in both methodologies.

	EPA (TO-15)	**Phoenix**
Analysis Method	ECP-GC/MS	ECIP-FTIR
Target Science	Human Health	NATTS Chemistry
Target Airmass	Bakground Urban	Background Urban
Target Analytes	NATTS	NATTS
Flow Rate	5 sccm	2000 sccm
Collection Time	24 hr	4 hr
Sample Volume	100 mL	480 L
Sampling Cycle	1 in 6 or 12 Days	6 in 1 Day
Water Management	Dry purge adsorbent trap before desorption	0.55 cm x 152 cm trap at -2 °C
Cryotrap Temperature	-150 °C	-150 °C
Cryotrap Channel	24.5 cm x 1.1 mm SS	0.55 cm x 178 cm Silanized SS
Cryotrap Packing	Hybrid Column Tenax/Deactivated Glass Beads	1 mm Silanized Glass Beads
Cryotrap Coolant	Liquid Argon	Mechanical Cryocooler
Desoprtion	120 °C with He	100 °C with N_2
Cryofocusing Trap	Active Adsorbent	N/A
Cryostat Pressure	N/A	Soft Vacuum
Detection Threshold	4-240 pptv	6-60 pptv
Process Control	Linux	LabVIEW

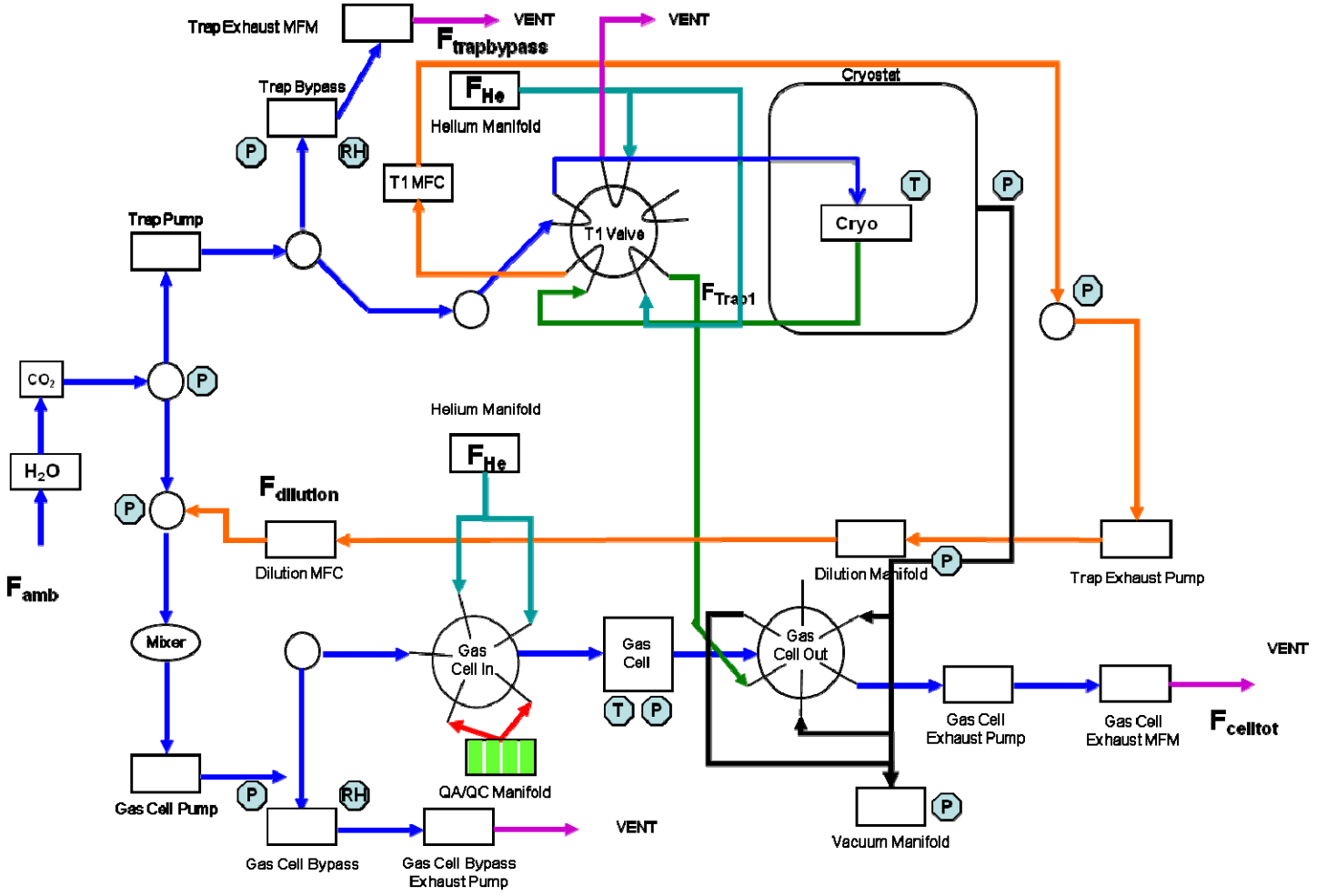

Figure 4.2. Phoenix Flow schematic. Blue paths represent ambient air flow. Green paths represent cryogenically preconcentrated flow. Orange paths represent dilution air flow. Blue-green paths represent helium (purge) flow. Red paths represent calibration gas flow. Black paths represent vacuum flow. Purple paths represent vented flow.

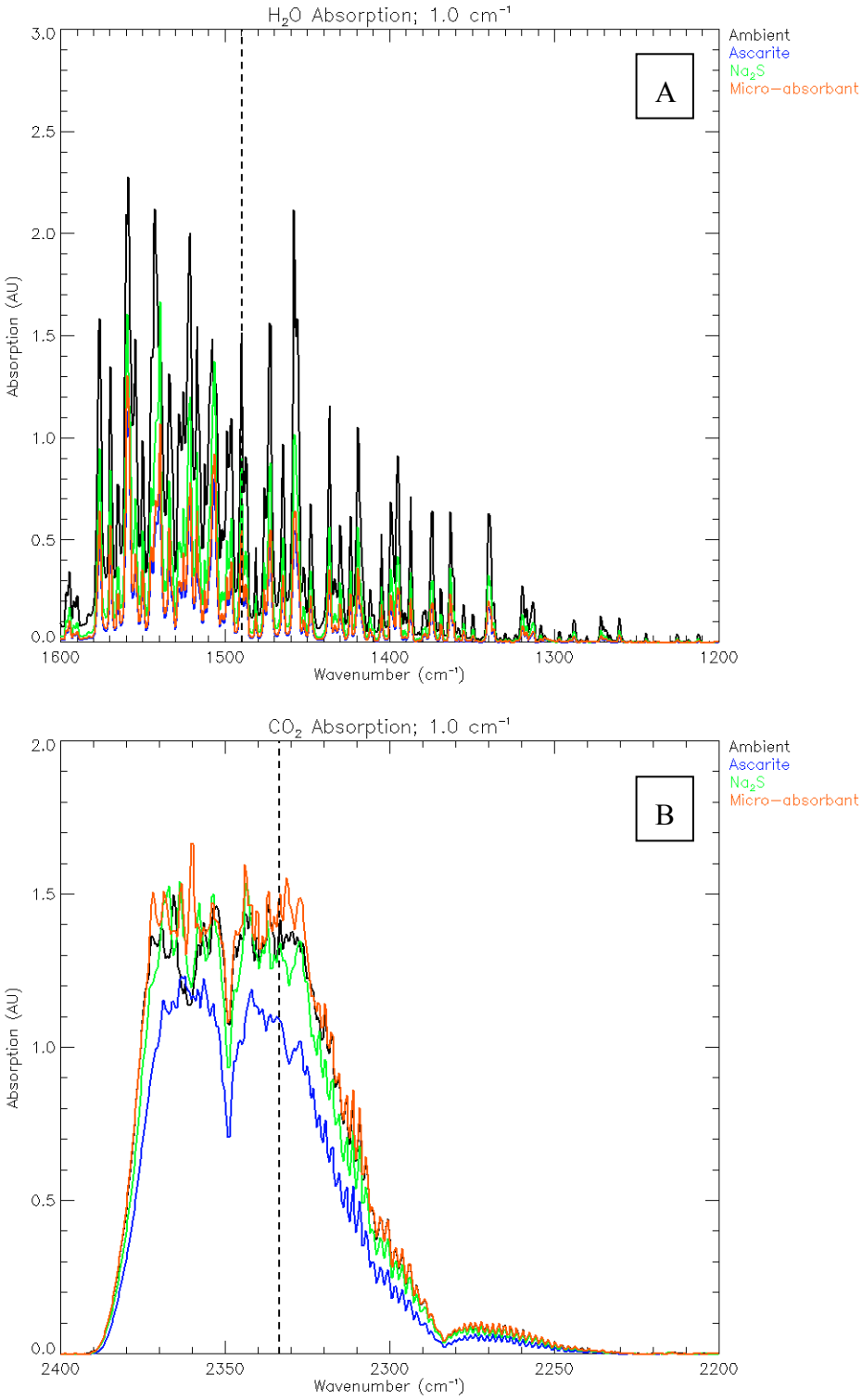

Figure 4.3. IR spectra between 1600-1200 cm^{-1} (Panel A) and 2400-2200 cm^{-1} (Panel B) to illustrate water vapor and CO_2 trapping efficiency. Quantification performed at 1490 cm^{-1} for water vapor and 2332 cm^{-1} for CO_2 represented by the vertical dashed line.

Metal Bellows, Sharon, MA). From the outlet of the gas cell supply, the ambient flow splits into either the gas cell flow path or the gas cell bypass. The gas cell bypass directs the partially diluted ambient flow through a back-pressure controller to maintain the gas cell at one atmosphere. Flow control and monitoring devices for temperature and relative humidity (RH) are also part of the gas cell bypass, which avoids placing them in line with the analytical flow path. The gas cell flow path channels the partially diluted ambient air through the gas cell inlet stream-selection valve and into the long-path gas cell for FTIR analysis. Sensors monitor gas cell pressure and temperature in real time. MFCs control the volumetric flow rate through the gas cell at 2 LPM by a critical orifice with a downstream exhaust pump (KNF Neuberger, Trenton, NJ), and mass flow meters (MFM) monitor the flow rate in real time (MKS Instruments, Andover, MA). This flow rate ensures adequate residence time in the gas cell. The gas cell bypass and gas cell flow path are rejoined downstream of the gas cell and upstream of a second MFM that monitors the total flow out of the entire gas cell portion of the flow schematic ($F_{Celltot}$). Once the flow meter records flow values, the flow stream is vented back into the ambient through an exhaust manifold.

The top portion of Figure 4.2 shows the second primary path. The ambient sample flows through the trap supply pump and splits into two paths. The top path is the trap bypass portion of the flow schematic. This portion is similar to the gas cell bypass outlined above. More emphasis is placed on the RH measurements in order to determine the dilution required to prevent water condensation in the gas cell. This flow measurement (F_{trap_bypass}) is used to compute the total ambient flow when either the dilution ($F_{dilution}$) or spike (F_{VOC}) flows are present.

The lower path is where the ambient sample is cryogenically preconcentrated, which improves the sensitivity of Phoenix. A single stage 0.635 cm OD x 0.55 cm ID x 177.8 cm cryogenic trap packed with 1-mm silanized glass beads is wrapped around a 7.62 cm OD x 5.08 cm copper torus. The torus is cut to 4.7 cm above the bottom, leaving 0.38 cm of copper in direct contact with the adapter plate (see Figure 4.4).

Following a four-hour sample collection, the trap valve is switched from sample to purge, the cryotrap is thermally desorbed at 100 °C (F_{trap1}), and the desorbed concentrate is deposited through the gas cell outlet valve into the vacuum-pressurized gas cell for FTIR analysis. This trapping process provides the necessary SNR enhancement required to measure low-concentration ambient organics.

The QA/QC manifold performs internal system validation cycles on a 24-hour basis. This portion of the flow system (F_{VOC}) can either flow directly into the gas cell or mix with the incoming ambient airstream near the ambient inlet. By injecting known amounts of calibration standards and comparing the resulting spectra, Phoenix can quantify analyte losses and related artifacts, and identify the flow channels where those artifacts occur.

b. Subsystem Descriptions

The following section outlines the subsystems comprising Phoenix, including optical, fluid, computer, and auxiliary subsystems. Each subsystem device is listed in Table 4.3. Process control algorithms integrate these subsystems into an autonomous air quality monitoring system capable of long, uninterrupted sampling periods.

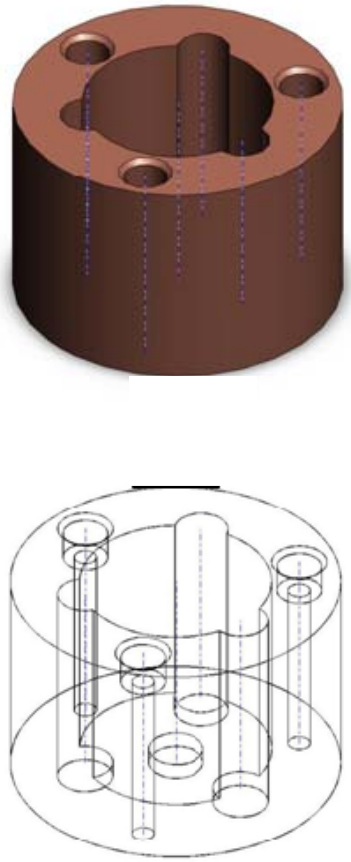

Figure 4.4. Current heat sink configuration. The configuration is 5.08 cm in height cut to 4.7 cm above the base. The diameter is 7.62 cm.

Table 4.3. Device listing by subsystem.

Subsystem	Category	Item	Manufacturer/Supplier
Optical	Analyzer	FTIR	Bruker Optics
		IR Gas Cell	CICP
Cryogenic	Cryocooler	Acoustic Stirling Cryocooler	CFIC
	Cryostat	Cryostat with Feedthroughs	Nor-Call
		Copper Heat Sink Exhaust Fans	McMaster-Carr
		Cryogenic Insulation	Evonik
Fluid	Pump	Supply	Metal Belows
		Exhaust, Vacuum	KNF-Neuberger
	Manifold	QA/QC Dilution	Swagelok
		Exhaust, Vacuum	McMaster-Carr
	Valve	Multi-position Stepper	VICI
		Vacuum, Relief, Check	Swagelok
		Soleniod	Norgren
		Critical Orifice	Lenox Laser
	Calibration	Gas Bottles	Spectra Gases, MESA
		Regulators	Swagelok
	Flow Channel	Tubing, Fittings	Swagelok, VICI
		Cryotrap Media	OVC
		Silcosteel Coating	Restek
Electrical	DAQ	Chassis, Modules, Controllers	NI
	Power	AC: Receptacles, Power Strips Surge Protectors, UPS	Tripp-Lite
		DC: Power Supplies	Acopian
	Heating	Heaters, Controllers, TCs	Watlow
	Monitoring	Temperature, RH	Vaisala
		Mass Flow Meters/Controllers	MKS
		Pressure Transducers	Omega
		Pump Speed Sensor	Red Lion
		AC/DC voltage, current	McMaster-Carr
	Accessories	Cables, Connectors, Junctions	Turck
Mechanical	Instrument Cart	Extruded Aluminum Frame	80/20

1) Optical

Two primary components make up the optical subsystem: the FTIR spectrometer and the long-path IR gas cell. Both elements work in concert to produce mid-IR spectra of all analyzed samples, whether they are non-concentrated continuous flow samples or preconcentrated batch samples from the cryotrap.

The FTIR is a commercial model Tensor 27™ from Bruker Optics® (Billerica, MA). Figure 4.5 diagrams the optical path for the Tensor 27™. In this configuration, the IR source (Figure 4.5.A) is directed toward a potassium bromide (KBr) beamsplitter (Figure 4.5.D) through adjustable aperture and filter wheels (Figure 4.5.B and C, respectively). This setup yields a receiver-specific spectral range of 7500 – 370 cm^{-1}. During spectral analysis, Phoenix analyzes the mid-IR range (4000 – 400 cm^{-1}) with quantitative emphasis on the window between 1200-600 cm^{-1}, between the thermal IR water vapor window and the ν_2 bending mode CO_2 feature. The beamsplitter partially reflects the source radiation to one of two mirrors: one stationary and one moving. Both split beams return to the beamsplitter where the reflected and transmitted radiation beams recombine interferometrically. The modulated beam is transmitted to the switching mirror (Figure 4.5.E), through the sample compartment via barium fluoride (BaF_2) coated windows (Figure 4.5.F), and onto the detector (Figure 4.5.H).

The Phoenix FTIR uses a thermal electromotive deuterated L-α-alanine doped triglycine sulfate (TE-DTGS) element which offers long-term thermal stability and a wide spectral range yielding reasonably high spectral resolution (0.5 cm^{-1}) and adequate sensitivity. Also, this type of detector has a more linear response than mercury cadmium telluride (MCT) detectors without additional cooling, which makes them better for

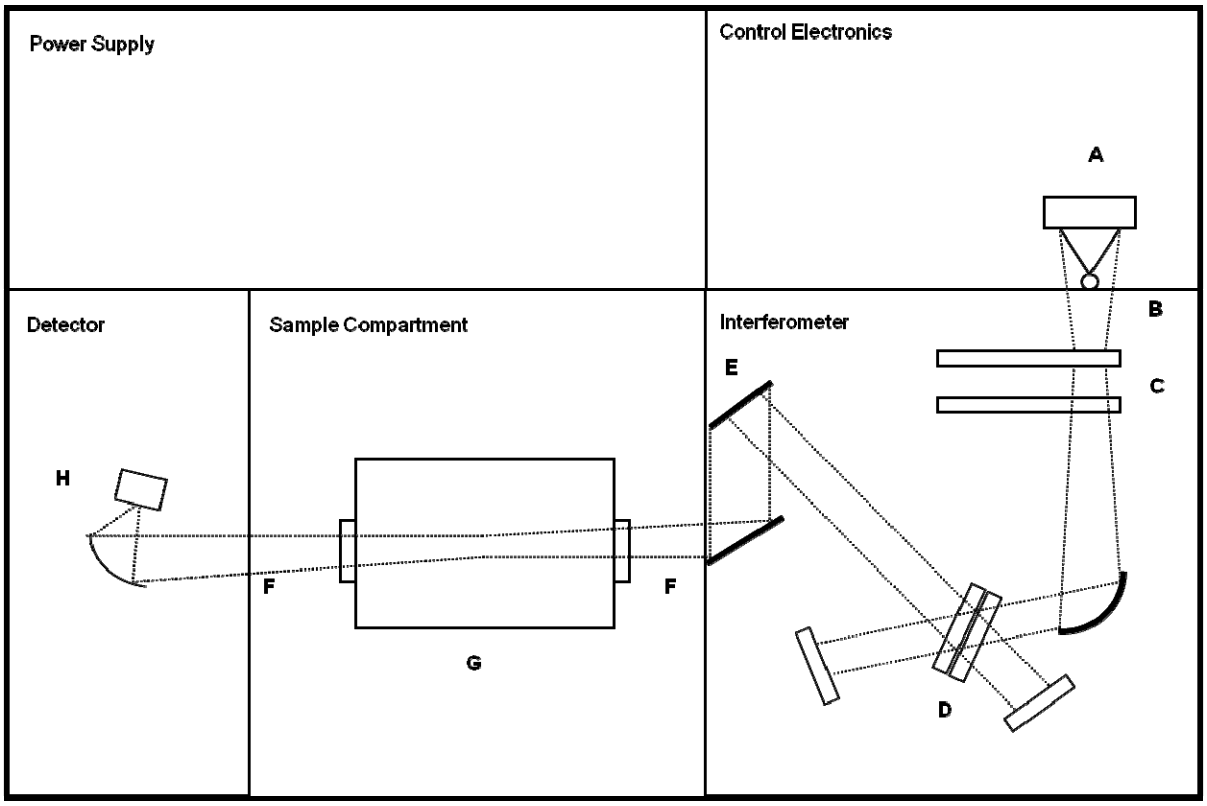

Figure 4.5. The optical path for the Bruker Optics Tensor 27™ FTIR. The mid-IR source (SiC glow bar; A) is directed through the aperture wheel (B) and the filter wheel (C) before entering the interferometer optics. The source is directed though the beamsplitter (D), reflected by the moving and stationary mirrors, back to the beam splitter to interfere. The modulated recombined beam proceeds to the switching mirror (E), and out of the interferometer compartment through a barium fluoride coated mirror (F) into the sample compartment, through the gas cell (G; see Figure 4.6), and into the detector compartment where the detector (H) measures the interferogram.

quantitative applications [*Griffiths and deHaseth*, 2007; *Richardson et al.*, 1998]. With this configuration, the Tensor 27™ has a wavenumber accuracy of better than 0.01 cm^{-1} and a photometric accuracy of better than 0.1%.

Before the modulated IR beam reaches the detector, it passes through a long-path gas cell (Figure 4.5.G). The gas cell chosen for Phoenix is the MARS-2L/10M-SS unit from Gemini Scientific Instruments (Buena Park, CA).

Figure 4.6 shows a vertical cross section of the optical path inside the cell. The IR beam passes into the gas cell folding mirror and a zinc selenide (ZnSe) optical window at the base of the gas cell (Figure 4.6.E). Once inside the gas cell, the beam is reflected by a series of precision aligned mirrors (Figure 4.6.B and D), where the beam passes vertically through the sample multiple times to improve the measurement sensitivity. Once the 40 passes are complete, the beam exits the gas cell through a matching ZnSe window and folding mirror, and enters the detector compartment where the detector measures the interferogram.

Optical Users Software (OPUS) version 5.5 controls the FTIR and all data manipulation processes, including Fourier transform, spectral co-addition, and file conversion. Customized process control software calls critical FTIR procedures and software macros, automating the entire analysis process, which is important for field operations.

This optical configuration produces high SNR and long-term stability in an idealized laboratory environment. Figure 4.7 plots the SNR from a geometric scan series and compares it to the optimal SNR modeled using square root of scan count, *N*. The root mean squared (RMS) SNR increases as a function of the number of scans as predicted in

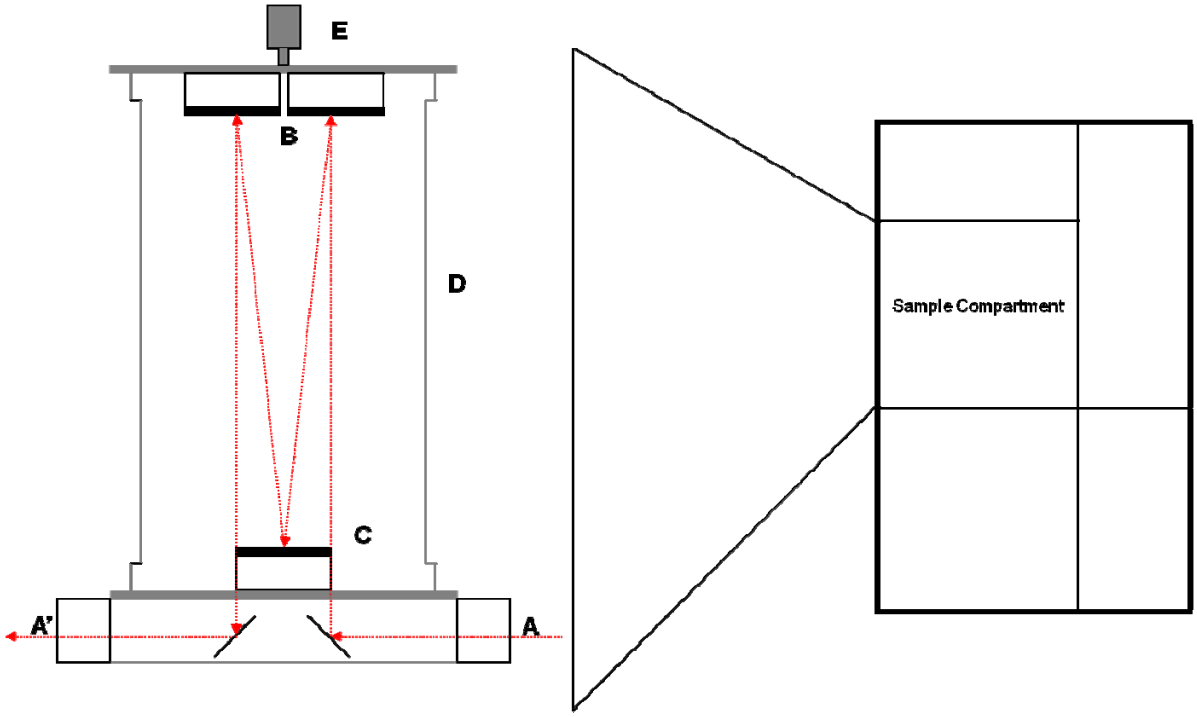

Figure 4.6. Vertical cross-section of the schematic optical path for the Gemini Scientific MARS-10M-2L-SS IR gas cell. Once the modulated IR beam leaves the interferometer compartment, the beam enters the gas cell through the optical window (A). From there it is reflected 40 times between the precision mirror mounts (B & C), and back out through an optical window (A') to the detector. Gas samples enter and leave the gas cell body (D) through longitudinal tube stubs (E).

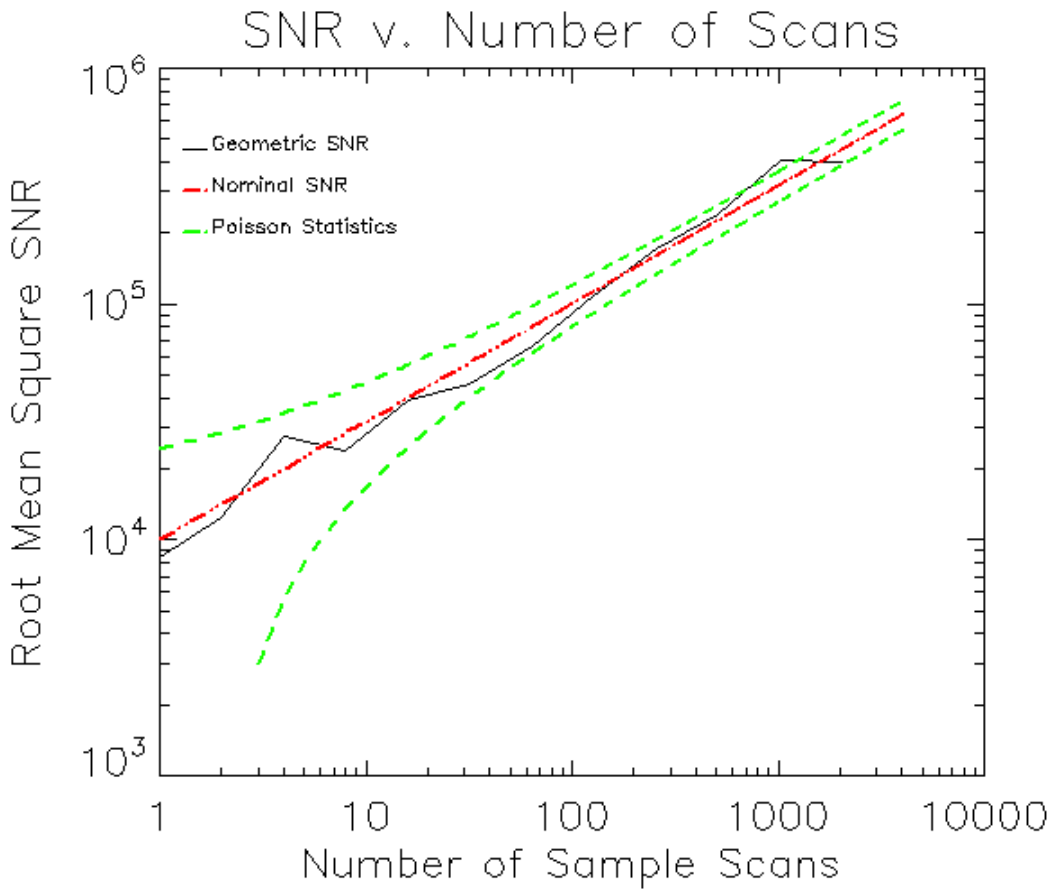

Figure 4.7. Signal-to-noise ratio versus number of scans (1,2,4,8…4096) on log-log scale. The black trace is the sample SNR as calculated from the 100% spectrum (the ratio of two spectra obtained under identical conditions with an empty sample chamber) between 2100 cm^{-1} and 1900 cm^{-1}. The red trace is the nominal SNR based upon the $\sqrt{t}$ relationship. The green traces represent the uncertainty envelope as predicted by Poisson statistics for a finite number of sample scans, background scans, and spectral bins.

the experimental model. OPUS calculates RMS SNR by fitting a parabola to the spectrum between 2200-2100 cm^{-1}. This parabolic curve defines the nominal signal, and RMS is calculated as the root of the mean square of deviations (i.e., the standard deviation) from that nominal signal.

In order to determine the overall FTIR performance two sets of spectra were collected at different spectral resolutions (1, 2, 4, 16, 32, 64 cm^{-1}) at 16 scans for 0.3 psi air, 15 psi air, and 15 psi UHP dry N_2. RMS SNR and peak to peak noise were calculated and ratioed to observe the stability of the analysis system at varying spectral resolutions and sample pressures. Figure 4.8 shows the Phoenix FTIR to be stable over increasing spectral resolution even at very short scan times.

2) Fluid

The fluid subsystem is made up of three primary components: the preconcentration system, the exhaust and vacuum manifolds, and the QA/QC manifold. Silanized stainless steel (SS) tubing makes up the majority of fluid subsystem, with all whetted surfaces receiving passivation coating (Restek Silcosteel; Bellefonte, PA) and additional cleaning with acetone, deionized water, and low-temperature bake out. All fluid components are connected via silanized SS tubing with multi-port switching valves from Valco to maintain sample purity and integrity.

Phoenix contains two exhaust manifolds: the gas cell bypass and the cryotrap bypass. Each manifold is made of chemically-resistant Teflon® (PTFE) and houses several analytical sensors and relief valves critical to the overall performance and safety of the system. The first is the gas cell bypass (Path 1 in Figure 4.2). This bypass line

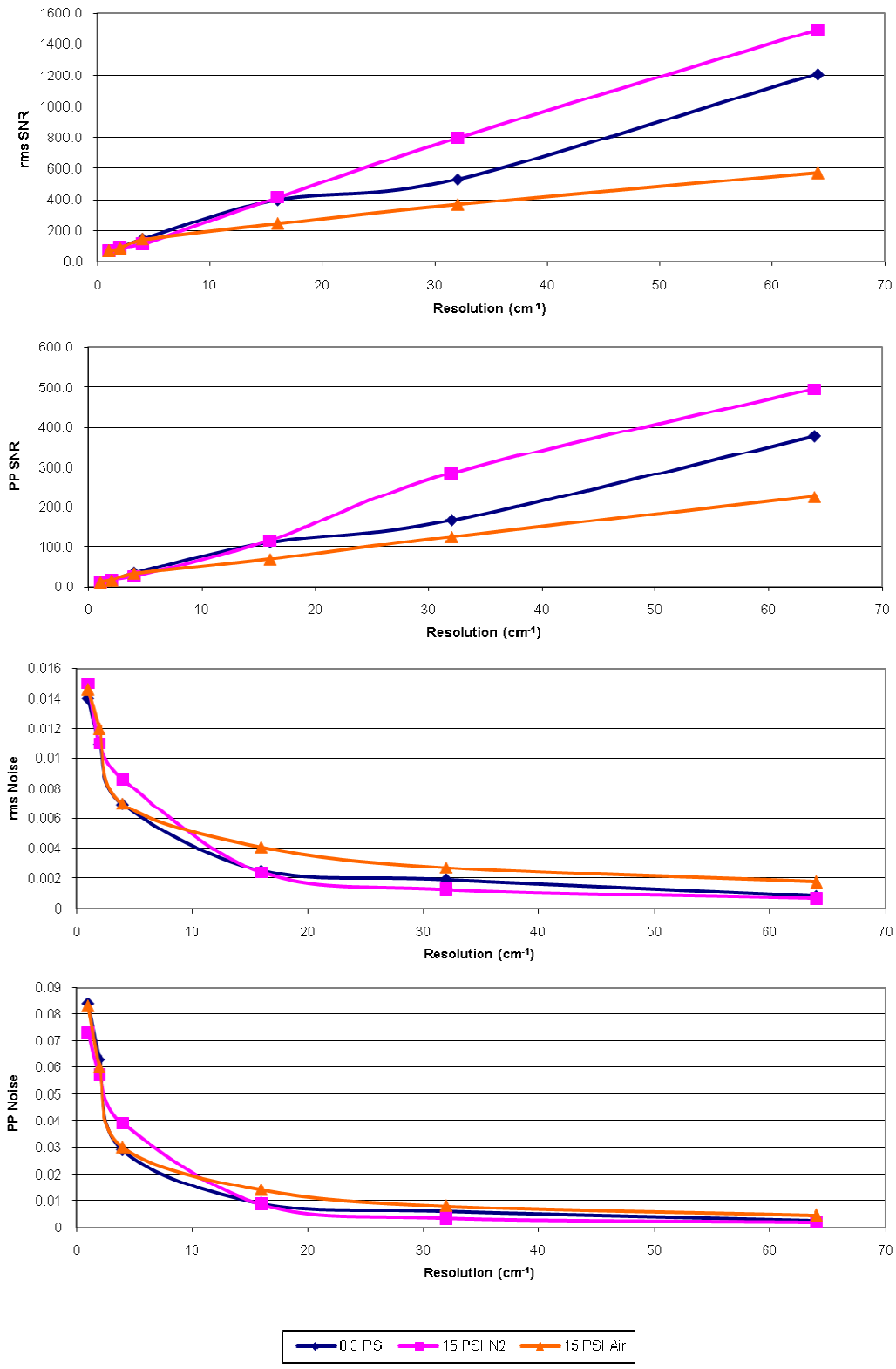

Figure 4.8. RMS and PP SNR and noise ratio versus spectral resolution (cm^{-1}) for three samples. Each spectrum was collected over 16 scans and ratioed with a like spectrum to illustrate system stability.

allows the FTIR to analyze the sample from a controlled excess flow instead of the entire flow output from the gas cell supply pump, which can produce sporadic fluctuations in flow rate. Two types of pressure sensors monitor the gas cell bypass flow. The first is a stainless steel mechanical dial pressure gauge placed upstream of the back-pressure controller. This device allows real-time systems monitoring during initial setup, lab testing, and field inspection. The second is an electronic pressure transducer from Omega Engineering, Inc. (Stamford, CT) downstream of the pressure controller, which allows remote monitoring of the gas cell exhaust pumpperformance. An RH sensor monitors the water vapor content in the flow that enters the gas cell, assuming that the RH is the same in the gas cell flow and its bypass flow. This measurement verifies that the dilution has been done correctly. Finally, a safety relief valve prevents potential damage to the supply pump and other sensitive components if plugging occurs downstream.

The trap bypass (Path 4 in Figure 4.2) serves a similar purpose for the cryotrap by housing several analytical sensors for the flow into the cryotrap. Both pressure sensors offer real-time and remote monitoring of the health and safety of the cryogenic system. RH measurements are important prior to entry into the cryotrap, to determine the dilution required to protect the gas cell from internal condensation. The back-pressure controller stabilizes the pressure in the trap during the collection process to ensure reproducible deposition in the trap for a given analyte at a given partial vapor pressure in the ambient atmosphere.

As described in §IV.*a*, the preconcentration system is the key unique component to the Phoenix design methodology. The preconcentration subsystem integrates a cryogen-free Stirling cryocooler from Q-Drive (Troy, NY) with a custom in-house

cryotrap. The cryocooler has a cooling capacity of 10 Watts at the desired cryotrapping temperature of 100 K. Estimated cooling time to reach 100 K is ~12 minutes as listed by the manufacturer. However, because of parasitic heat loads on the cryocooler cold head and the thermal inertia of the heat sink, that time is increased to ~12 hours. This is not an issue, because once the operational temperature is achieved, the thermal inertia of the heat sink avoids the need for continual cycling, so the system does not need to continually cool to 100 K.

Following conditioning of the ambient flow in the inline H_2O and CO_2 traps, the sample flow stream continuously enters the cryotrap housed inside a vacuum-sealed cryostat from Nor-Cal Products, Inc. (Yreka, CA). Water vapor has a very broad spectral footprint in the IR spectrum mainly between 1200 – 2200 cm^{-1} with another window between 3500 – 4000 cm^{-1}. If excessive H_2O is present in the analyzed sample, many of the target analytes with key peaks in that same range will be obscured (i.e., acetaldehyde at 1750 cm^{-1}) and the ambient concentrations could additively contribute to lesser absorption features. This condition would degrade the accuracy of the concentration calculations. Second, if the total H_2O burden reached the packed cryotrap, that trap would quickly plug. Third, if excessive H_2O passes into the gas cell, it would condense in the cell, where it would cause critical damage to sensitive precision optical surfaces. Removing this variable mitigates one error source and a potential source of long, costly repairs.

Similarly, the Ascarite trap removes CO_2 from the sample stream. Carbon dioxide has two strong absorption windows in the mid-IR between 600-800 cm^{-1} and 2200-2400 cm^{-1}. If CO_2 remained in the sample stream, these two ranges would have limited or

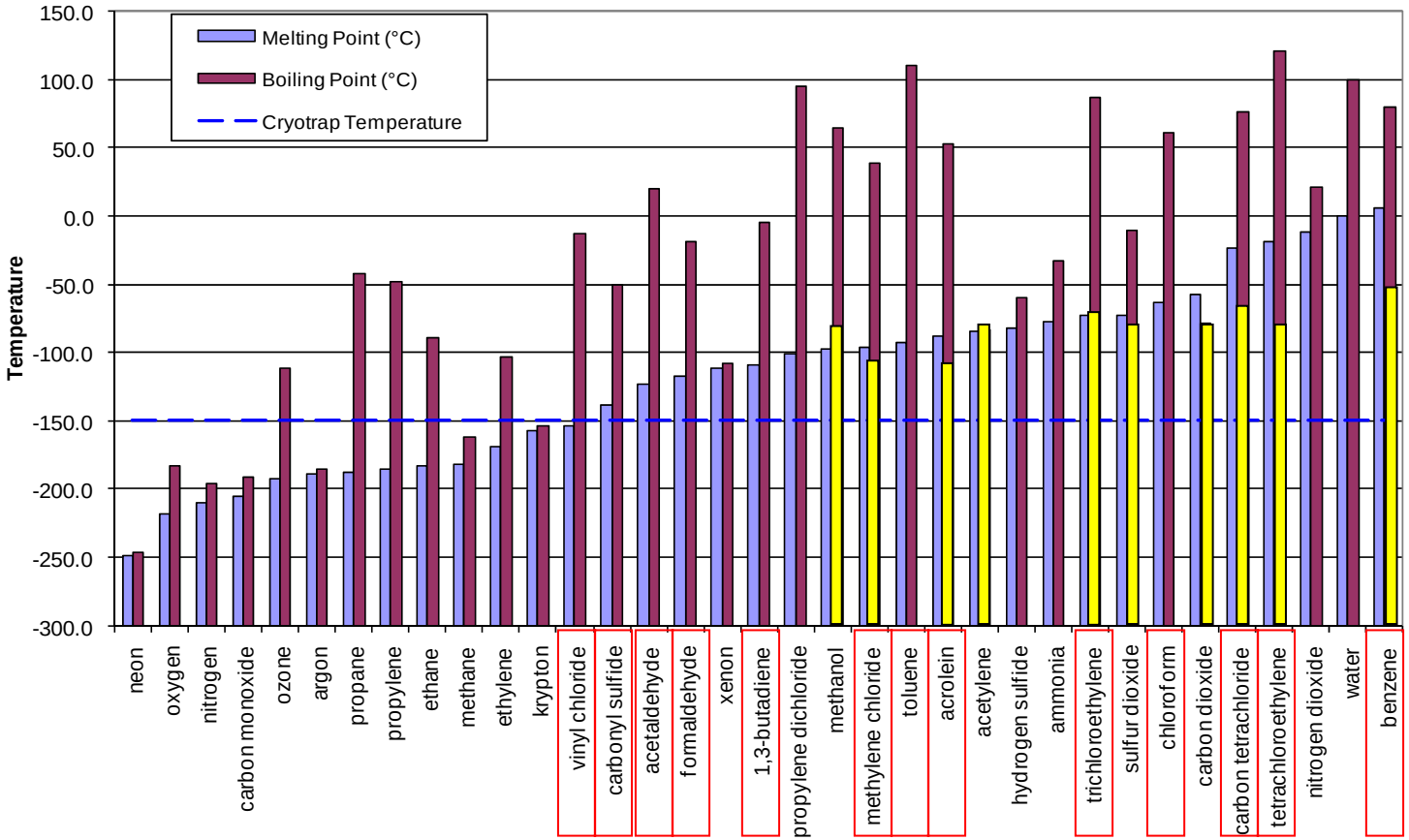

Figure 4.9. Experimental cryotrap temperatures. The cryotrap preconcentrates each analyte sampled by Phoenix at -150 °C. Every compound is trapped at this temperature with the exception of eight compounds on the far left of the chart. The yellow ranges represent the condensation temperatures of the compounds shown. The compounds highlighted in red are those in Table 4.1.

no use in spectral quantification. The total CO_2 burden would not condense in the gas cell, but could plug the cryotrap over long periods

With two key major gases managed, the sample flows into the cryotrap, which is maintained at -150 °C during sample concentration. At this temperature, many atmospheric constituents change phase from gas to liquid as shown in Figure 4.9.

Inside the cryotrap, inert silanized glass beads (Ohio Valley Specialty, Marietta, OH) provide adequate surface area for the condensation of the target analytes at a flow rate of 2 LPM for a four hour cycle. Total flow through is 480 L; however, 99% of this sample is atomic oxygen (O_2) and nitrogen (N_2) which will not trap at this temperature. After the sample collection is complete, resistive heaters (Watlow Electronics, St. Louis, MO) warm the trap to 100 °C to desorb the trapped analytes into the gas cell. UHP N_2 purges the trap and brings the gas cell up to 1 atm for sample analysis.

Two other components of the fluid subsystem are the vacuum and exhaust manifolds. The vacuum manifold channels the vacuum pump flow to various portions of the system. The first is the cryostat, which is maintained at soft vacuum (~10 hPa) to reduce parasitic heat loss to the walls of the cryostat via convection and to prevent H_2O from condensing in the cryostat. If H_2O comes in contact with the cryocooler coldhead, it would form an ice bridge on the coldhead. This bridge would increase parasitic heat loss from the nearest cryostat wall surface. If the ice bridge reached the wall, it would create a thermal short that dramatically increases the parasitic heat load on the cryocooler. If an ice bridge were to melt, say during an extended line power outage that shut off the cryocooler, an electrical short could occur, which would damage the cryocooler. Vacuum flow is also channeled to the gas cell to assist in purging the gas cell for background

spectrum collection and preparation for sampling insertion. The exhaust manifold collects effluents from the gas cell and trap bypass, vacuum pump exhaust, and safety relief valves before they are vented back to ambient.

The final component of the fluid subsystem is the QA/QC manifold. This manifold was custom built for Phoenix by Swagelok. The QA/QC manifold performs on-board quality assurance by periodically collecting spectra of known analytes from on-board calibration gas bottles. Current calibration gases available for QA/QC are 1 ppb benzene / 1,3-butadiene mix (Spectra Gases, Inc., Stewartsville, NJ), and 100 ppm toluene (Mesa Specialty Gases, Santa Ana, CA). A pressurized bottle houses each calibration gas with a vendor's certification of that concentration for a 12-month operational life. A series of pneumatically actuated shut off valves opens and closes certain portions of the flow path. Double block-and-bleed stream selector valves open the desired QA/QC gas bottles, while preventing upstream cross-contamination of these critical calibration flowstreams.

Figure 4.10 shows a mechanical drawing of the QA/QC manifold.

3) Computer

The operational PC controls a PCI-6225 card from National Instruments (Austin, TX). This PCI card is a multifunction data acquisition (DAQ) device with 80 16-bit analog input (AI) channels, two 16-bit analog output (AO) channels, and 24 8-bit digital I/O channels. These channels control the signal conditioning boards which include a shielded I/O connector block containing 68 AI channels and a powered multiport signal condition extension for instruments (SCXI) chassis along with a terminal block with 50 AI/AO/DI/DO channels and a 32-channel isothermal thermocouple amplifier and

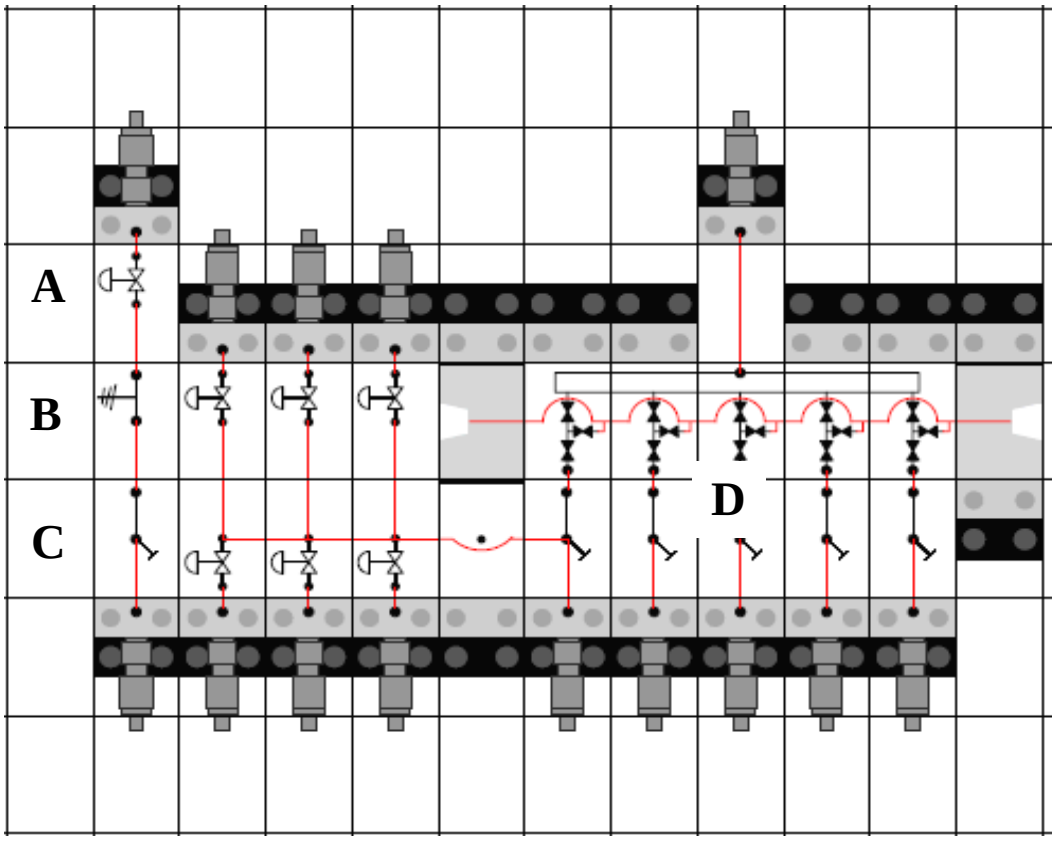

Figure 4.10. Flow schematic overlaid on base mechanical drawing for the Phoenix QA/QC manifold. The left portion of the manifold houses seven pneumatic switching valves (A), a relief valve (B), and a pressure transducer (C). The right portion contains an array of five pneumatic double-block-and-bleed selection valves (D) which direct the flow of five calibration analytes into the analytical flow path for quality assurance purposes.

multiplexer. These devices combine to process the information collected by a series of sensors monitoring pressure, relative humidity, and temperature as well as system status indicators, shutoff and pneumatic controls for the QA/QC manifold and flow selection, and mass flow devices.

The NI DAQ uses customized software developed using LabVIEW version 9.0 (NI) to control data collection, system communication, and subsystem control for the entire Phoenix system. This software has been developed and tested over the course of system development and assembly with the purpose of operating Phoenix autonomously in the field. The primary system control virtual instrument (VI) integrates 61 sub-VIs to orchestrate and organize the data acquisition and process control algorithms, including FTIR analysis, flow control and selection, fault indication, and safety constraints.

A series of IDL (Visual Information Systems, Boulder, CO) programs provides additional data analysis, post processing, and visualization tools, including health and safety data, spectral files, and data visualization and analysis. These programs are customizable depending upon the final output destination, whether for scientific presentation or troubleshooting.

4) Auxiliary

The auxiliary subsystem makes up the remainder of the Phoenix operation components. It includes the electrical and mechanical portions of the system. The main electrical supply comes from four Acopian power supplies (Easton, PA). One 24 V DC, 2.1 A supply powers the many pressure transducers and relative humidity sensors. A second 24 V DC, 5 A drives the exhaust, gas cell, and cryotrap pumps. A ± 15 V DC, 2.5 A supply provides power to the MFCs and MFMs. Finally, the 24 V DC, 2.5 A mini-

encapsulated power supply feeds power to the solenoid valve islands which drive the pneumatic valves that select the various flow paths within the system. Digital panel meters on the exterior of the transport cart as well as by the DAQ continually monitor the power supplies. These redundant systems ensure the system is operating safely.

External AC power outlets provide power to several other devices on Phoenix. An 8-port power strip proves power for the Valco valves, the heater controller banks, the cryocooler, and cascading power strips. These cascading strips have multiple filters minimizing EMI/RFI on the most critical electronic elements, including the FTIR. A universal power supply (UPS) backup battery provides another failsafe for Phoenix. In the event of a power failure, the backup will provide 15 minutes of reserve battery power to complete any data collection and allow the automation software to detect the problem and safely power down without data loss.

A custom-built mechanical transport constructed with aluminum T-slot extrusions (80/20, Inc., Columbia City, IN) houses every subsystem element mentioned above. This wheeled transport is 0.93 x 0.76 x 1.3 m, well suited for deployment into the field. Vertical dividers separate the transport into three compartments. The electronics compartment holds the computer, one-Terabyte remote hard drive, and UPS as well as the power supplies and relays. The cryogenic compartment houses the cryocooler and the QA/QC cylinders. The FTIR compartment contains the optical subsystem components. The top panel of the transport houses the DAQ and SCXI, all fluid elements including the pumps, valves, and plumbing, sensor junction boxes, and the heater controllers.

c. Safety Constraints

During full systems testing in October 2009, the QDrive cryocooler speed relay control box (SRC) overheated due to excessive power load, and caught fire, causing extensive damage to the cryocooler and all on-board devices. This event lead to the overhauling of all major Phoenix systems, and lead to the integration of numerous safety measures. First, the cryocooler SRC received 10 W of fusing in order to prevent overload and subsequent overheating. One 5 W fuse was installed by the manufacturer (CFIC, Inc.) inside the SRC. A second after-market 5 W fuse was placed in line with AC power. Additionally, exhaust fans prevent recirculation of cryocooler exhaust air into the air-cooling inlet for the cryocooler compressor.

Second, Phoenix has an array of thermocouples along several critical points in the system, including the SRC, the cryocooler inlet and exhaust ports, the trap and gas cell metal bellows pumps, the vacuum pump, and the operations PC. These sensors provide critical data to the process control algorithm to ensure the system is operating properly. If a sensor indicates a temperature beyond the nominal operational range, the process control algorithm begins recording that sensor. If this value remains outside of the first threshold after one minute, or if the sensor reads a second critical value, the system performs a soft shut down and notifies the user. This ensures proper operations and prevents the system from overheating again, causing further damage to the system.

Third, in-line pressure transducers monitor pressure throughout the fluid subsystem. To prevent over pressurizing and monitor for leaks and blockages, the process control algorithm has threshold ranges much like those for the thermocouples. If a

transducer records a pressure over a threshold value, the data acquisition system records these values, and if the value remains outside the first threshold or exceeds a second critical value, Phoenix shuts down and notifies the operator.

CHAPTER V

DATA ANALYSIS

a. Whole Air Samples

In order to verify Phoenix observations and collect a short-term picture of VOCs in Huntsville, AL WAS were collected and analyzed. The sampling began 5 May 2011 at 0600 CDT and ended 7 May at 800 CDT with a 12-hour data gap due to Phoenix process control algorithm malfunction. WAS were collected every hour while Phoenix collected samples every 4 hours through a Teflon inlet located 2 meters above the NSSTC roof at 225 m above sea level. The WAS were shipped to UNH for analysis utilizing methods previously outlined [*Sive et al.*, 2005; *White et al.*, 2008; *Zhou et al.*, 2005; *Zhou et al.*, 2008]. Briefly, WAS were analyzed within a week of receipt at UNH on a three GC setup using two FIDs, two ECDs, and an MS for a selected list of VOCs and halocarbons. Each sample is analyzed by trapping 1000 cm^3 of the sample onto silanized glass beads housed within a SS loop immersed in LN_2. After trapping, the operator removes the loop from the cold bath, heats the loop to 80 °C, and injects the sample into the analytical system. Helium carrier gas flushes the trap contents and a manifold splits the flow stream into five separate GC columns, which direct the sample to one of the five analytical detectors. Analytical precision varies from 0.1 to 12% [*Zhou et al.*, 2005] and detection thresholds range from 0.01 – 10 pptv [*Colman et al.*, 2001] depending on the compound.

b. Meteorological Measurements and Field Measurement Context

Dr. Kevin R. Knupp has fitted the NSSTC Berm at UAHuntsville with an array of meteorological instrumentation (Berm Elevation: 212 m). The Berm is 100 m to the southwest of the sample inlet location. Two Vaisala (Woburn, MA) Model HMP-45C Probes measure temperature and RH at 2 m and 10 m. A platinum resistance temperature (PRT) detector measures temperature at +/- 1% accuracy. A Vaisala Humicap H-chip monitors RH at +/- 3% accuracy in high humidity conditions and 0.5 second response time. One R. M. Young (Traverse City, MI) Model 05103 propeller anemometer measures wind speed and direction at +/- 1% wind speed accuracy and +/- 3° direction accuracy. One Vaisala Model PTB201B barometer measures pressure using Vaisala's Barocap sensor with an accuracy of +/- 0.30 hPa. One Eppley (Philadelphia, PA) Precision pyranometer measures incoming solar radiation with an overall accuracy of +/- 1%. One dual tipping bucket rain gage measures rain fall amounts in 0.01" increments with an accuracy of +/- 1%. Finally, the NSSTC Berm is fitted with a 2000 Hz Doppler Sodar capable of measuring acoustic backscatter power and three-component wind speed and direction with 25 m gate spacing, starting at 40 m and reaching heights of 700 m depending on the amount and type of scatters present in the beam. The backscatter power gives insight into the temperature and height of the boundary layer (BL). The information from these sensors provides the meteorological and dynamical context in which we collected the field measurements. The Berm was not operating from 1800 CDT 4 May to 1755 CDT 5 May. Except for the Sodar data, which resumed operations at 1600 CDT 5 May, the Berm data were not available for the initial WAS data collection period (0600-1755 CDT 5 May). The accompanying figures are the following meteorological

analysis cover the period from 1800 CDT 5 May to 1800 CDT 7 May, which includes the remaining WAS collection period.

Figure 5.1 shows the data from the 2 m and 10 m HMP-45Cs. The 2 m temperature provides an understanding of the surface conditions during the time of the observations. The minimum surface temperature between 1800 CDT 5 May and 0600 CDT 6 May was 48 °F with a dew point temperature of 47 °F. This dew point depression is typical of early spring in Huntsville. Following the transition of stable nocturnal boundary layer (NBL) to unstable daytime boundary layer, the temperature on 6 May peaked out at 73 °F with rapid fluctuations indicative of small-scale turbulent eddies generating local increases in wind speed and direction (Figure 5.2a,b). Large dew point depressions during the afternoon of 6 May indicate a low likelihood of near-surface heterogeneous chemistry and the formation of SOA [i.e., *Ambrose et al.*, 2007; *Jacob*, 2000; *Riemer et al.*, 2003; *Salawitch et al.*, 1994; *Ziemba et al.*, 2010]. However, the opposite is true in the stable NBL particularly in the early part of the morning on both 6 and 7 May.

Broken cloud cover indicated in Figure 5.2d limited diurnal heating on 6 May, thus reducing generation of turbulent eddies and vertical transport and possibly maintaining a relatively low boundary layer height. Additionally, Figure 5.3b,c indicate vertical wind direction favors downward motion prior to system shut down. This vertical wind direction suggests limited upward mixing of surface emissions of 6 May. On 7 May turbulent fluctuations seem more prevalent during the early morning (Figure 5.2a) with cloud cover limiting surface heating in the afternoon (Figure 5.2d and Figure 5.1).

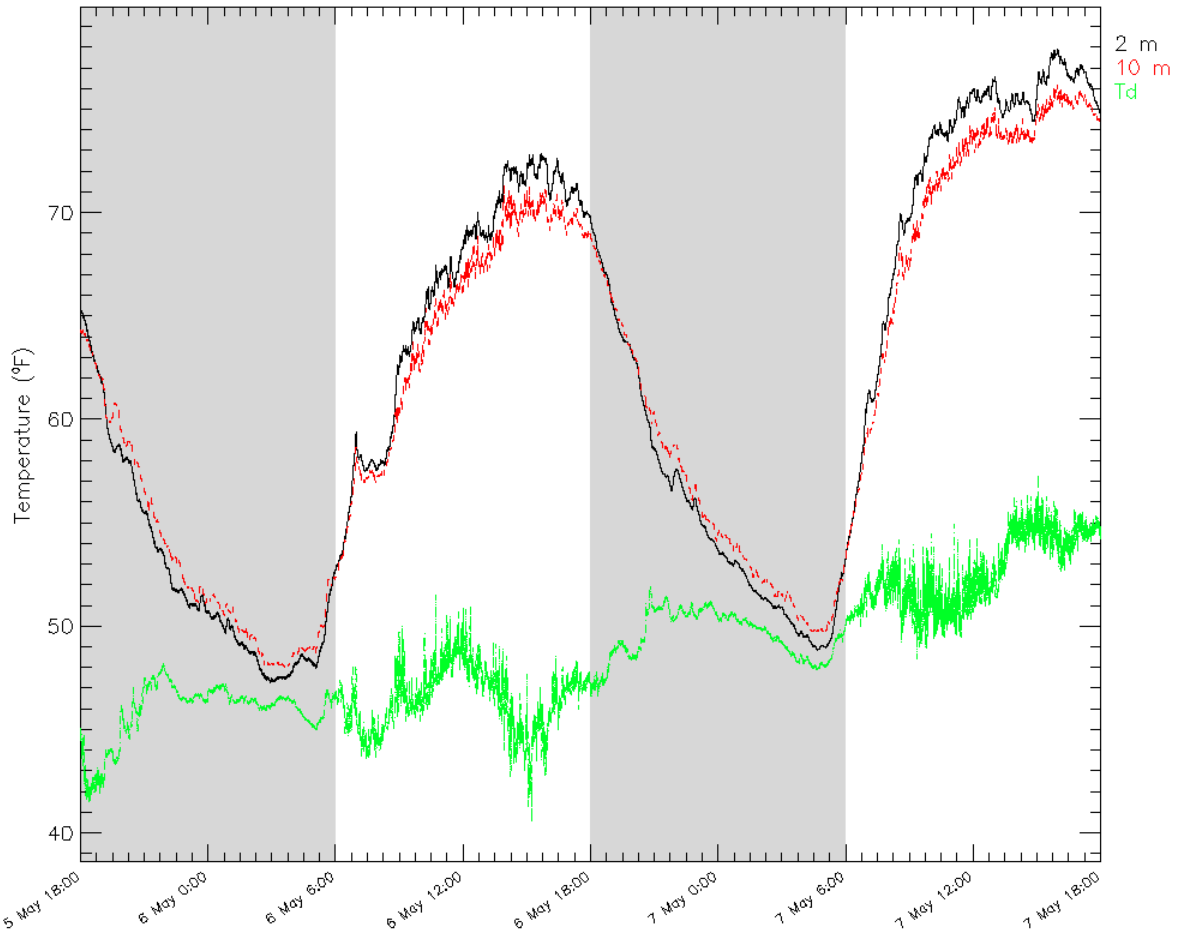

Figure 5.1. 2 m temperature (black) and dew point (green) and 10 m temperature (red) recorded at the NSSTC Berm from 1800 CDT on 5 May 2011 (0000 UTC on 6 May) to 1800 CDT on 7 May (0000 UTC 8 May). All three parameters are reported at 0.2 Hz as averages of 1 Hz data. Grey shading indicates nighttime hours (1800-600 CDT).

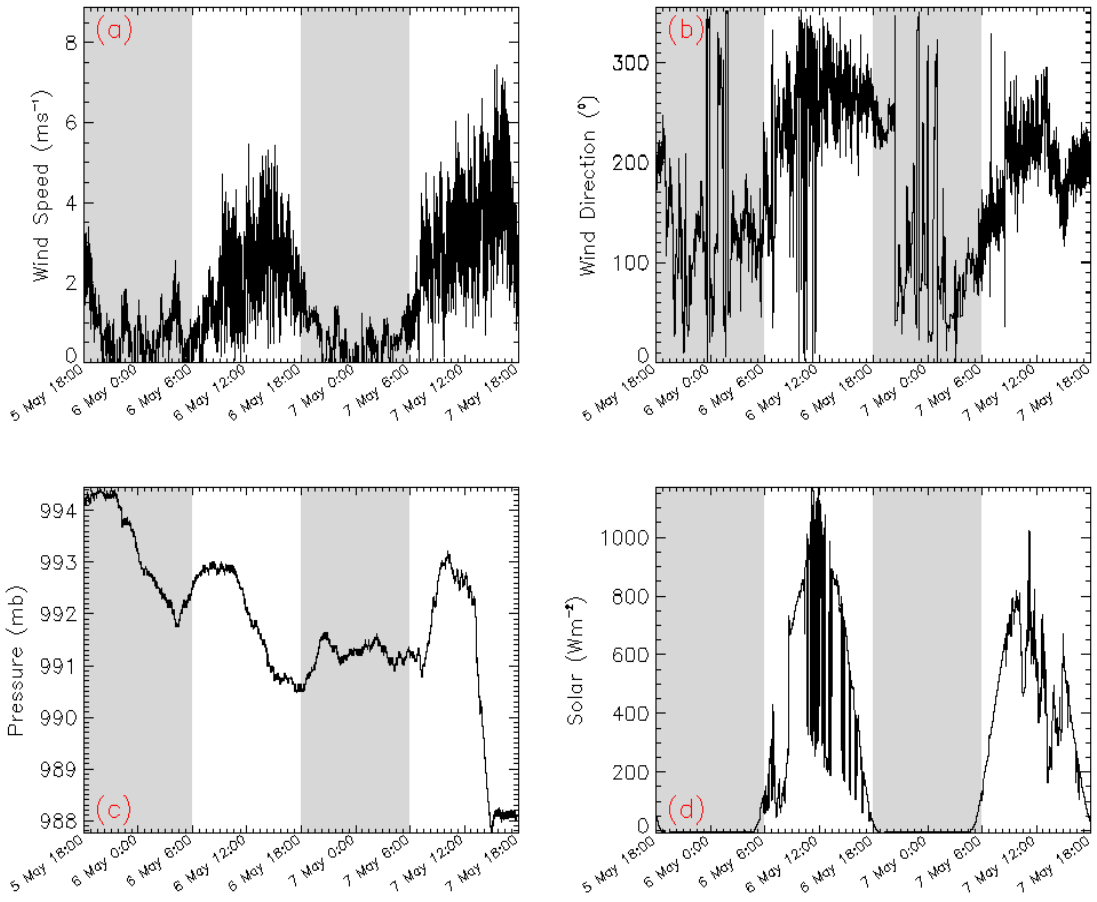

Figure 5.2. Wind speed (a), wind direction (b), pressure (c), and incoming solar radiation (d) recorded at the NSSTC Berm from 1800 CDT on 5 May 2011 (0000 UTC on 6 May) to 1800 CDT on 7 May (0000 UTC 8 May). All four parameters are reported at 0.2 Hz as averages of 1 Hz data. Grey shading indicates nighttime hours (1800-600 CDT).

Figure 5.4a from the Sodar backscatter indicates a turbulent layer height of roughly 250 m, offering additional mixing volume. However, vertical motions appear to favor downward motion (Figure 5.4b,c), again limiting upward mixing of surface emissions.

c. Surface Ozone Observations

The City of Huntsville's Division of Natural Resources under the guidance of the Alabama Department of Environmental Management and the EPA reports average hourly O_3 at a monitoring site on Airport Road in Southeast Huntsville, 7 km SW from the WAS sample collection and the Berm at the NSSTC. A Thermo Scientific (Milwaukee, WI) Model 49*i* U.V. Photometric Ozone Analyzer collects these measurements. The manufacturer of this instrument reports 1 ppb precision, but performance varies from site to site and analyzer to analyzer depending on up keep and calibration frequency. This data, provided by Ms. Deborah Hopson, allows us to put the WAS measurements into an additional chemical context. However, recent research showing horizontal variability between surface ozone measurements at the Airport Road site (Site 014) and the NSSTC can affect this comparison.[2] This research shows a correlation coefficient (R^2) of ~0.78 between the EPA surface O_3 measurements and the average boundary layer (0.3-2.5 km) O_3 measured by ozonesondes during IONS06 with decreasing correlation above the boundary layer. Also, correlation between the lowest ozonesonde measurement recorded and the sonde boundary layer average is 0.86, indicating the boundary layer is not always well mixed as is often assumed [e.g., *Couach et al.*, 2003; *Kuang et al.*, 2011; *Newchurch et al.*, 2011] (see Figure 5.5). This discrepancy causes inconsistencies when using the

[2] Personal Communications with G. Huang and W. Cantrell, 2011

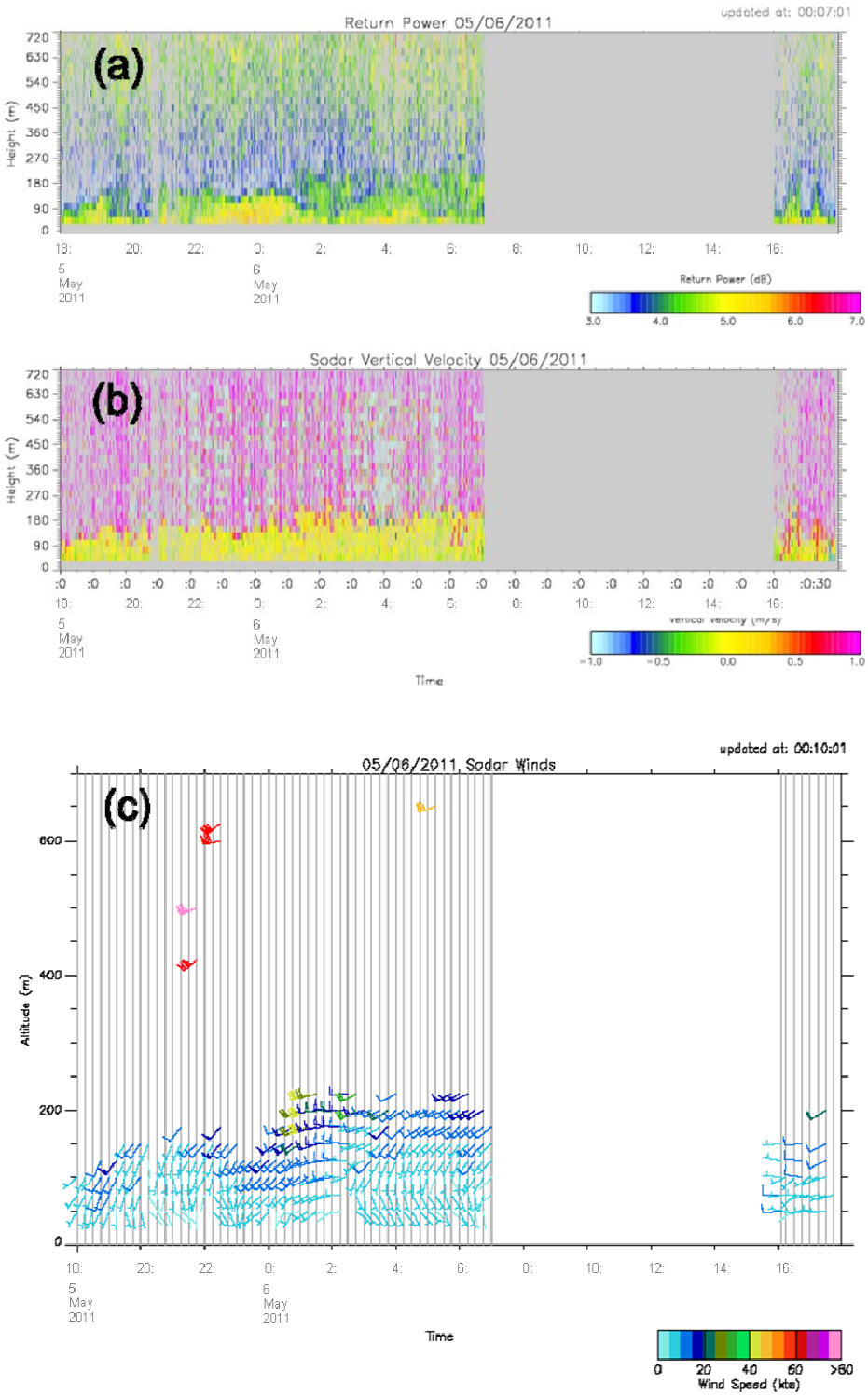

Figure 5.3. NSSTC Berm Sodar backscatter return power (a), vertical velocity (b), and vertical wind profiles (c) from 1800 CDT on 5 May 2011 (0000 UTC on 6 May) to 1755 CDT on 6 May (2355 UTC 6 May). All parameters are reported every 15 minutes as averages of 0.02 Hz data.

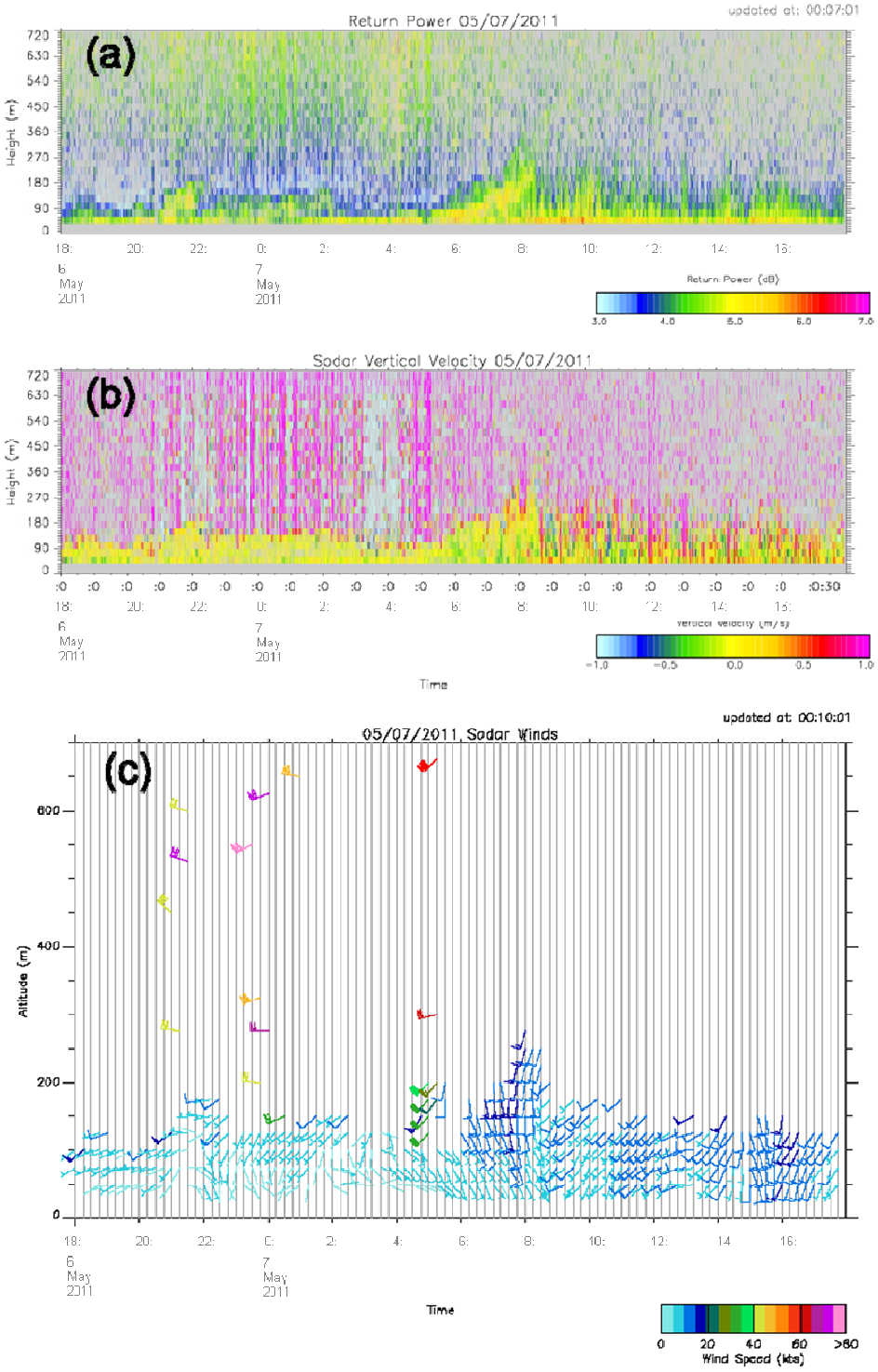

Figure 5.4. NSSTC Berm Sodar backscatter return power (a), vertical velocity (b), and vertical wind profiles (c) from 1800 CDT on 6 May 2011 (0000 UTC on 7 May) to 1755 CDT on 7 May (2355 UTC 7 May). All four parameters are reported every 0.2 Hz as averages of 1 Hz data.

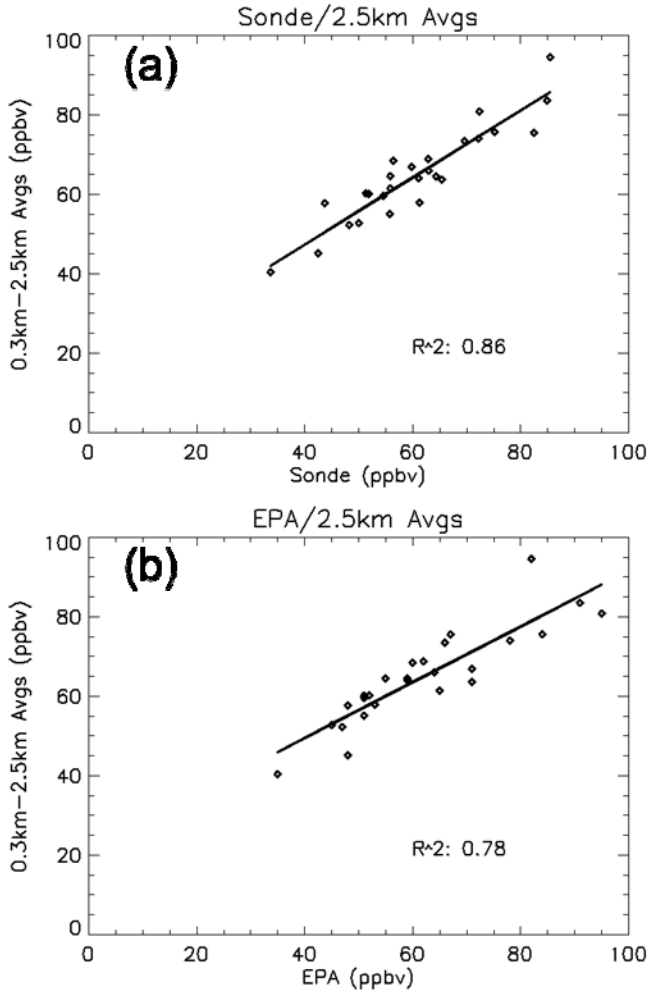

Figure 5.5. Surface O_3 measurements from the UAHuntsville Ozonesonde Station (a) and EPA Site 014 (b) compared to the average mixing ratio between 0.3-2.5 km (BL) from the ozonesondes collected between 1-31 August 2006 during the IONS-06 campaign. Typical measurement time is 1300 CDT. Figure courtesy of W. Cantrell. EPA Site 014 courtesy of D. Hopson.

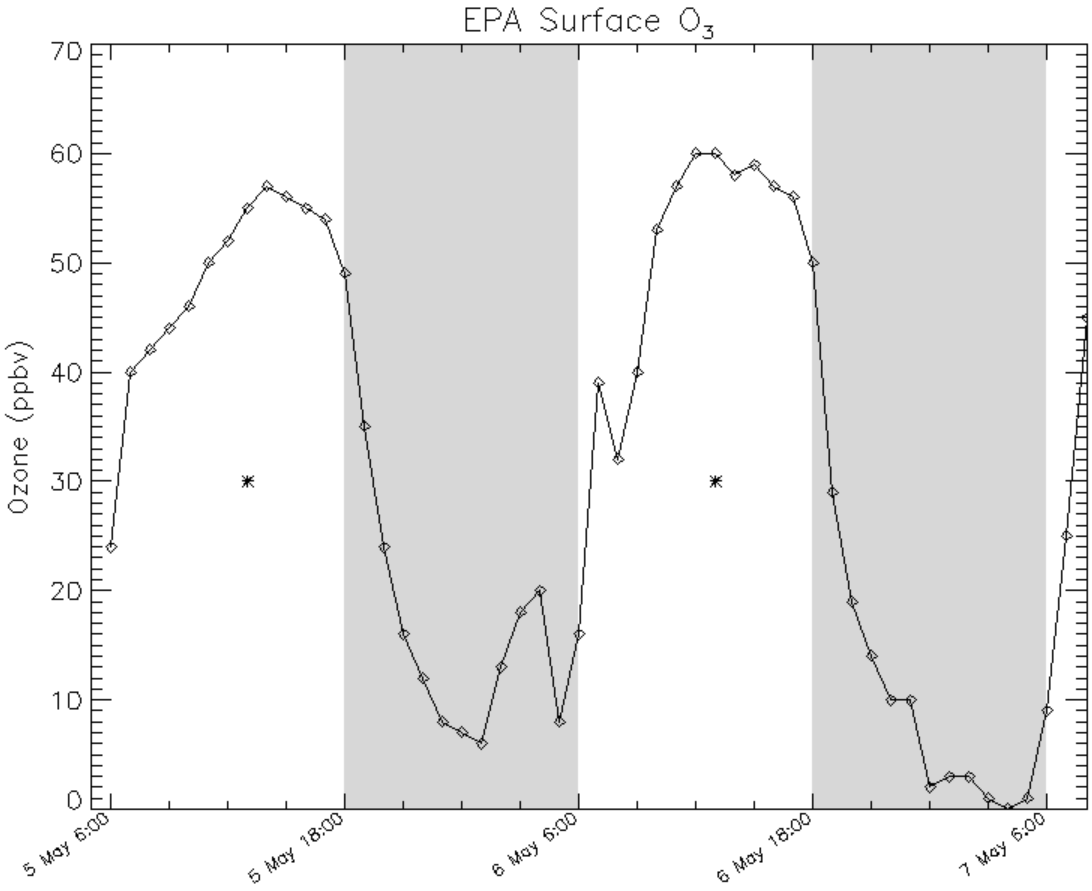

Figure 5.6. EPA Site 014 surface O_3 data from 1800 CDT on 5 May 2011 (0000 UTC on 6 May) to 1800 CDT on 7 May (0000 UTC 8 May). O_3 mixing ratio is reported as one hour averages of 0.0167 Hz data. Stars at 1300 CDT indicate average O_3 mixing ratio in May 2011 at the Huntsville Ozonesonde Station. Grey shading indicates nighttime hours (1800-600 CDT). EPA Site 014 courtesy of D. Hopson.

hourly average O_3 from Site 014 to assess the VOC-O_3 relationship in the measurements collected at the NSSTC. Additional concern arises given the strong wind speeds recorded at the Berm (Figure 5.2a) which are indicative of strong horizontal and turbulent vertical mixing.

Surface ozone at Site 014 shows the typical diurnal maximum, nocturnal minimum during the measurement period [i.e., *Blanchard et al.*, 2010; *Bloomer et al.*, 2010]. O_3 mixing ratio rises rapidly in the early morning as N_2O_5 quickly photolyzes to NO_3 and NO_2, nitric acid (HONO) photolyzes to OH and NO, and NO_x emissions provide sources for O_3 production. NO_3 photolyzes to generate additional NO_2 and $O(^3P)$. Additionally, NO_2 photolyzes to NO and $O(^3P)$. $O(^3P)$ combines with O_2 to produce O_3. NO reacts rapidly with O_3 to produce O_2 and NO_2. This catalytic cycle rapidly reaches photoequilibrium. However, depending upon NBL height and stability and availability of VOCs and NO_x, O_3 rises rapidly in the morning as NO_x mixing ratios increase and VOC mixing ratios decrease as the BL height increases.

$$NO_2 + NO_3 \leftrightarrow N_2O_5 \tag{5.1}$$

$$HONO + h\nu \rightarrow NO + OH \quad \lambda < 405 \text{ nm} \tag{5.2}$$

$$N_2O_5 + h\nu \rightarrow NO_3 + NO_2 \quad \lambda < 1250 \text{ nm} \tag{5.3}$$

$$NO_3 + h\nu \rightarrow NO_2 + O(^3P) \quad \lambda < 580 \text{ nm} \tag{5.4}$$

$$NO_2 + h\nu \rightarrow NO + O(^3P) \quad \lambda < 420 \text{ nm} \tag{2.5}$$

$$O(^3P) + O_2 + M \rightarrow O_3 + M \tag{2.6}$$

$$NO + O_3 \rightarrow NO_2 + O_2 \quad (5.5)$$

The hourly data from EPA Site 014 does not adequately capture the temporality of this effect; however, it is important to note as the measurements on 0600 and 0700 CDT on 5 May increase from 24 ppbv to 40 ppbv in one hour, a rise rate of 0.27 ppbv per minute. This rise in mixing ratio decreases to 0.040 ppbv per minute as NO_x and O_3 reach early morning photoequilibrium and sources of NO_x and BVOCs and the BL height increases. On 5 May, the peak O_3 mixing ratio is 57 ppbv at 1400 CDT due to a increase in cloud cover or the afternoon which might have limited afternoon temperatures (high of 67 °F recorded at Huntsville International Airport). Following this increase in cloud cover, O_3 mixing ratios leveled off and slightly decreased throughout the remainder of the day on 5 May and then rapidly decreased following sunset (1936 CDT). The average loss rate from 1800 CDT on 5 May to 0100 on 6 May was -0.11 ppbv per minute with the minimum reached at 0100 on 6 May of 6 ppbv.

At night, when O_3 and NO_x photochemistry ceases, O_3 reacts with NO and NO_2 to produce NO_2 and NO_3, respectively. NO_2 and NO_3 participate in a reversible reaction to form N_2O_5, a loss mechanism for O_3, which occurs more slowly than the early morning photolysis of N_2O_5. An interesting feature occurred between 0100 and 0400 CDT, when O_3 mixing ratios increased from 6 ppbv to 20 ppbv. This event coincided with an increase in Sodar backscatter power shown in Figure 5.3a, which might indicate horizontal transport of polluted air from another source, possible Houston, TX or Birmingham, AL. Additional research is required to confirm this hypothesis. This increase rapidly drops of to near background levels just prior to sunset.

Following sunset on 6 May, O_3 experiences a rapid increase from 0600 to 0700 from 16 ppbv to 39 ppbv, a rise rate of 0.38 ppbv per minute, slightly higher than the morning of 5 May, possibly due to the increased availability of NO_x generated from the influx of O_3-rich air during the early morning hours. A slight dip in O_3 mixing ratio at 0800 CDT coincides with a decrease in incoming solar radiation (Figure 5.2d), which then clears out around 0900 CDT and both temperatures (Figure 5.1) and O_3 mixing ratio (Figure 5.5) rebound. Surface O_3 mixing ratio peaks at 60 ppbv at 1300 CDT and decreases slightly in the hours that follow. This event coincides with broken cloud cover, which would have limited photolytic O_3 formation. Broken clouds persist throughout the remainder of the daylight hours and turbulent motions persist.

Following sunset (1936 CDT), O_3 mixing ratios decrease rapidly from 50 ppbv at 1800 CDT 6 May to 2 ppbv at 0000 CDT 7 May, an average loss rate of 0.17 ppbv per minute. Additional loss dropped the O_3 mixing ratio below the MDL of the instrument, indicating sufficient NO_x available for O_3 destruction and a stable NBL with limited horizontal wind speed (Figure 5.2a).

Similar to 5 and 6 May, O_3 mixing ratios rapidly increase from ~1 ppbv at 0500 CDT to 44 ppbv at 0800 CDT, an average rise rate of 0.24 ppbv per minute, which is comparable to the days prior. A steady increase in incoming solar radiation (Figure 5.2d) led to rapid generation of turbulent eddies (Figure 5.2a) and 2 m and 10 m temperature (Figure 5.1). These observations coincide with the final VOC observations made with both the WAS canisters and Phoenix.

d. Analysis of WAS for Local Background Values

WAS and Phoenix samples were collected from the fourth-story roof at the NSSTC. We selected this location for ease of operation and installation in support of preliminary instrument validation, and not for scientific data purity, knowing the emissions from the roof would affect the measurements. The WAS canisters were filled every hour on the hour to coincide with the Phoenix sampling configuration. Following the completion of the sampling, the filled cans were shipped to Dr. Barkley Sive at UNH to perform the GC/ECD/FID/MS analysis described in §V.*b*. Dr. Sive analyzed the canisters for C_2-C_5 alkanes (ethane, propane, i-butane, n-butane, i-pentane, and n-pentane), C_2-C_3 alkenes (ethene and propene), C_6-C_7 aromatics (benzene and toluene), ethyne, carbonyl sulfide (OCS), chloroform, carbon tetrachloride, trichloromethane, tetrachloroethylene, and dichloromethane. Both the WAS method and Phoenix monitor benzene, toluene, and the halocarbons These measurements occurred between 0600 CDT on 5 May and 0800 CDT on 7 May with a gap between 1800 5 May and 0600 6 May due to a necessary system reset on Phoenix.

Figure 5.7-14 show the results of the analysis on the WAS canisters. Overall, hydrocarbon mixing ratios were higher than those of the halocarbons, which is expected due to a lack of a strong halogen source in Huntsville and the proximity to the tar on the roof as a source of hydrocarbons. Ethane had the highest mean mixing ratio of 2.7 ppbv followed by propane (1.3), ethene (1.1), ethyne (1.1), and i-pentane (0.97). These light weight hydrocarbons emissions are possibly due to mobile sources such as motor vehicles and gasoline vapor [i.e., *Blanchard et al.*, 2010; *Olson et al.*, 2009] or the tar pitch used on the NSSTC roof. Additionally, long-lived compounds such as ethane and propane

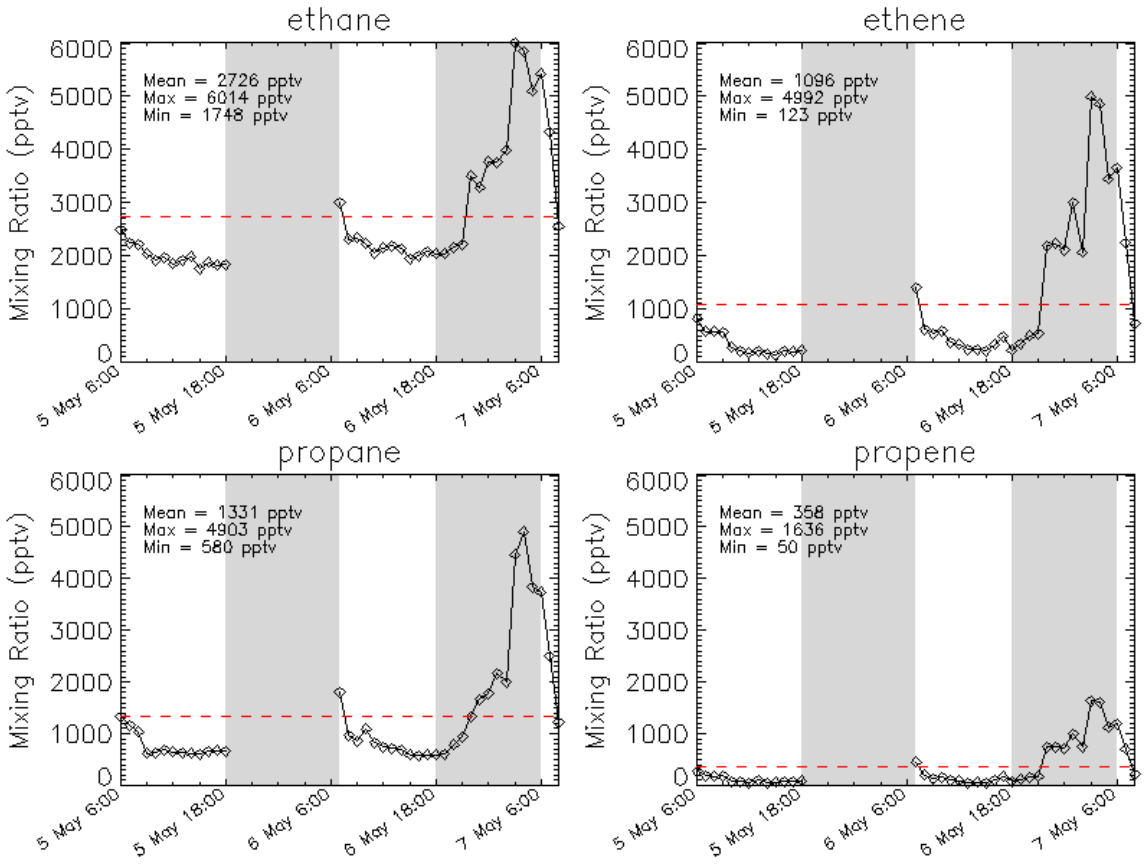

Figure 5.7. Hourly canister measurements of ethane, ethene, propane, and propene. Red dashed line indicates the average mixing ratio during the sampling period. Grey shading indicates nighttime hours (1800-600 CDT).

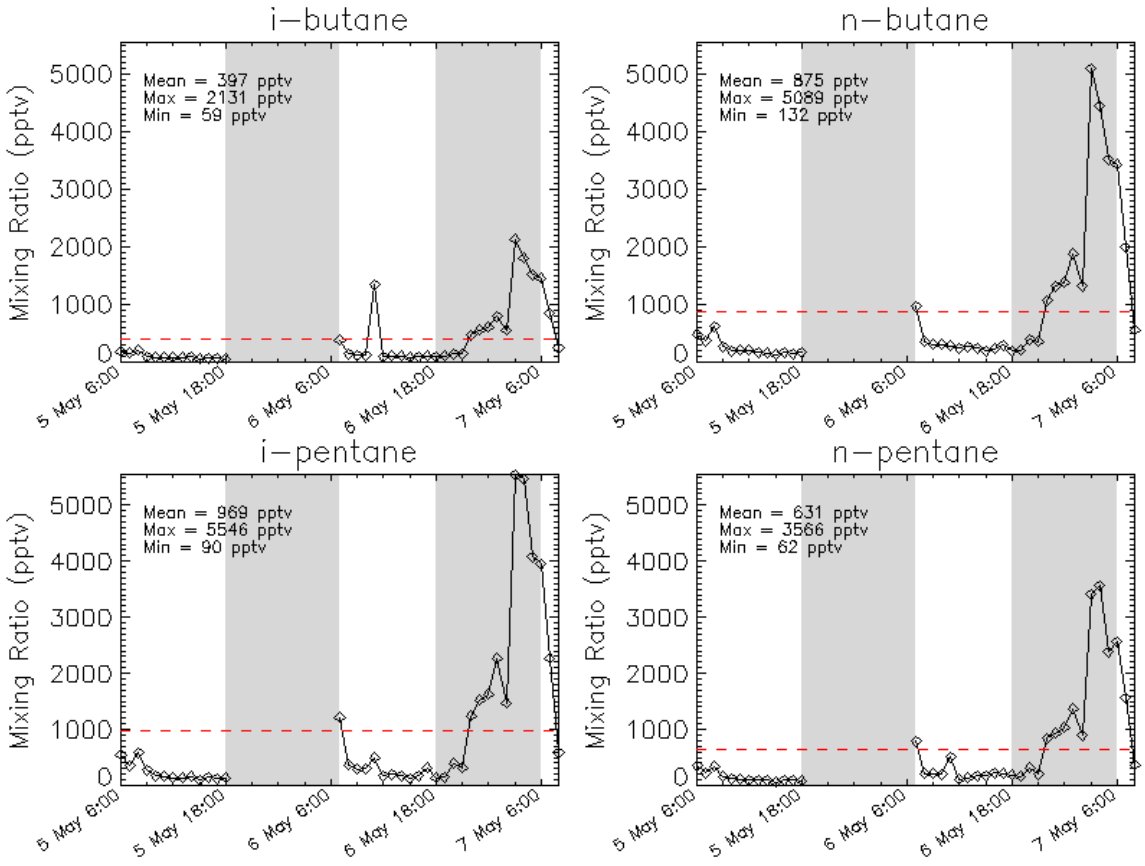

Figure 5.8. Hourly canister measurements of i-butane, n-butate, i-pentane, and n-pentane. Red dashed line indicates the average mixing ratio during the sampling period. Grey shading indicates nighttime hours (1800-600 CDT).

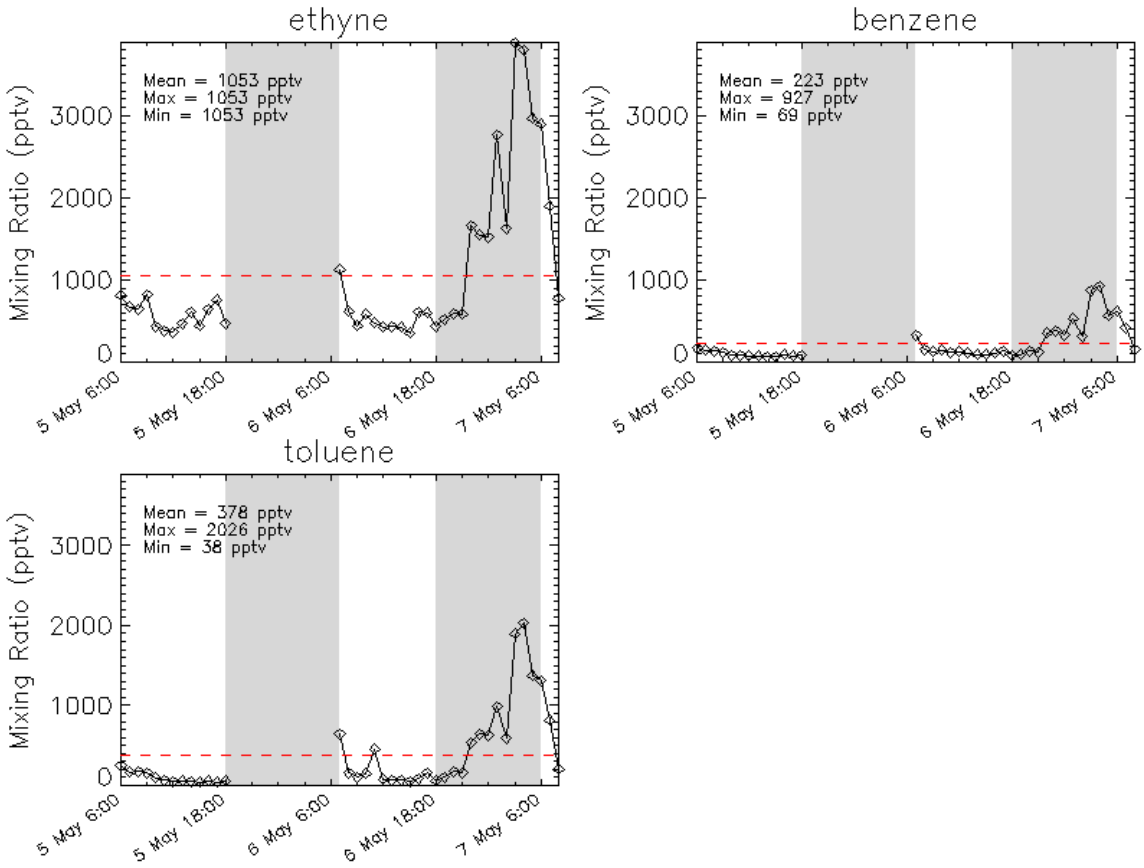

Figure 5.9. Hourly canister measurements of ethyne, benzene, and toluene. Red dashed line indicates the average mixing ratio during the sampling period. Grey shading indicates nighttime hours (1800-600 CDT).

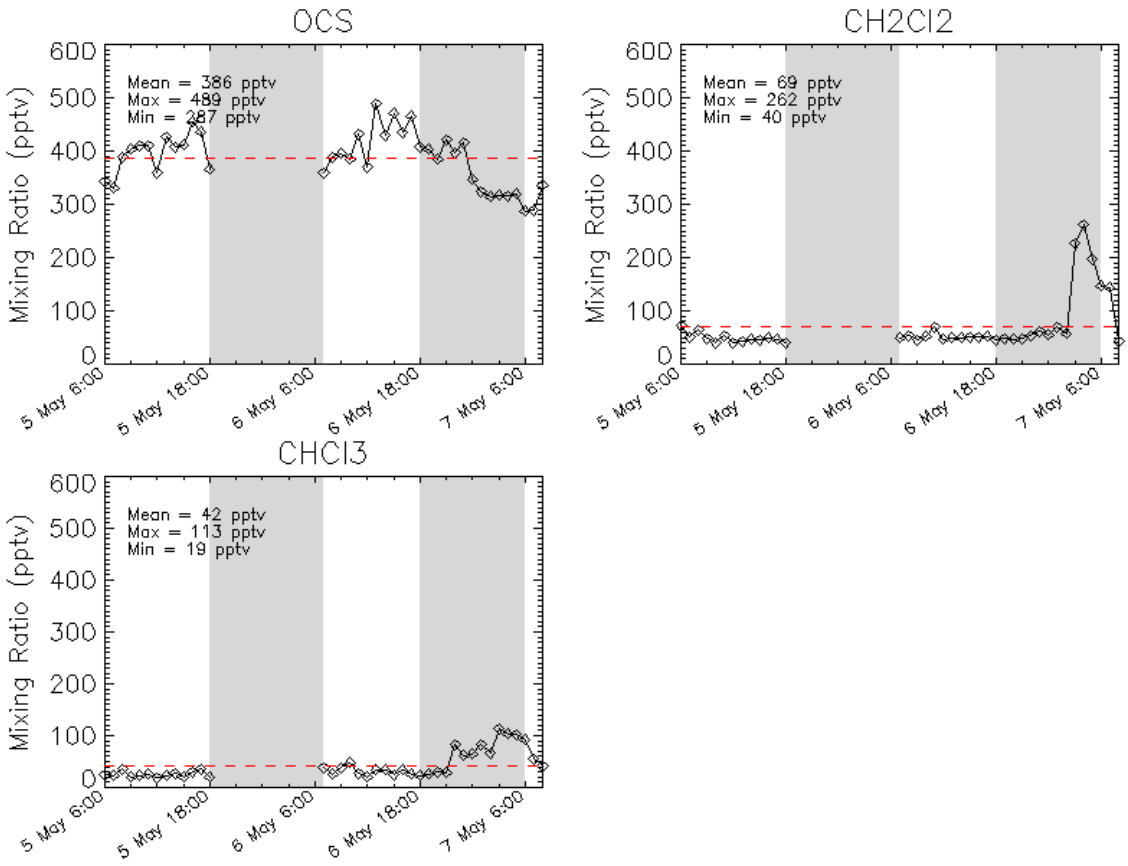

Figure 5.10. Hourly canister measurements of OCS, dichloromethane, and chloroform. Red dashed line indicates the average mixing ratio during the sampling period. Grey shading indicates nighttime hours (1800-600 CDT).

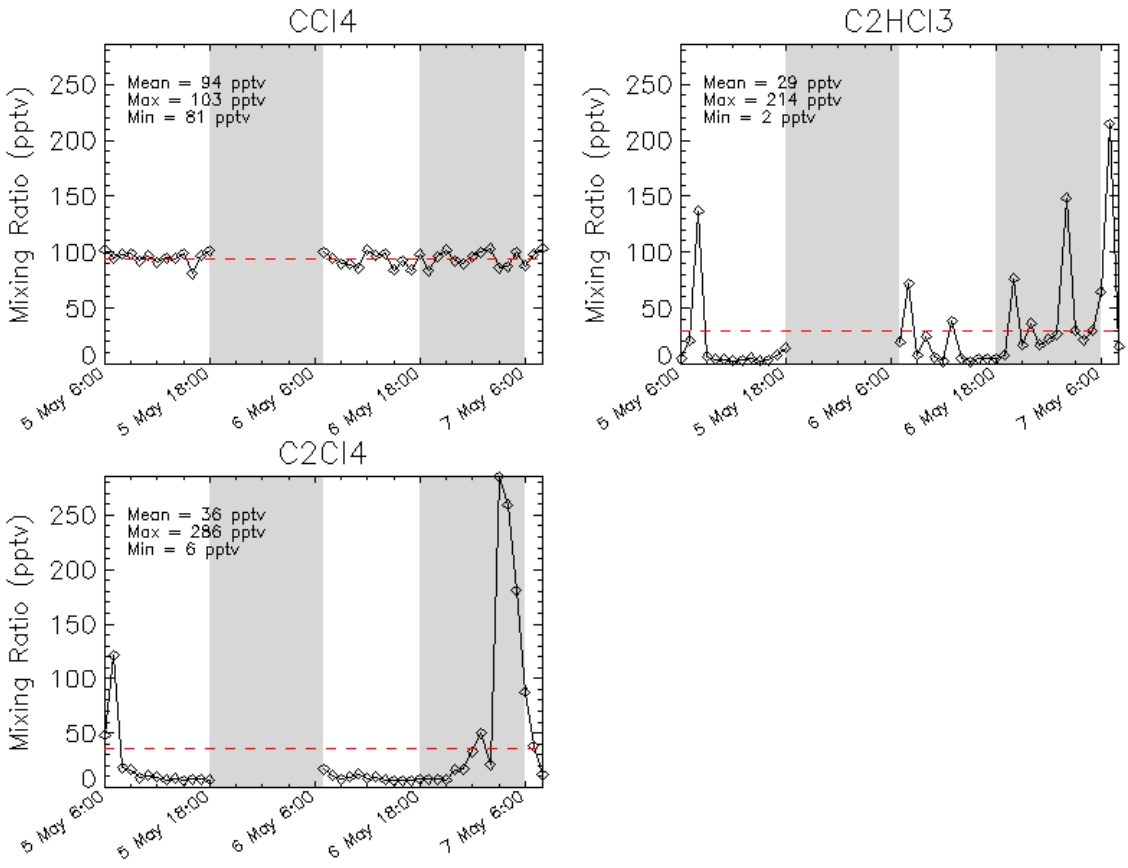

Figure 5.11. Hourly canister measurements of carbon tetrachloride, trichloromethane, and tetrachloroethylene. Red dashed line indicates the average mixing ratio during the sampling period. Grey shading indicates nighttime hours (1800-600 CDT).

could be horizontally transported over appreciable distances [*de Gouw et al.*, 2005; *Goldan et al.*, 2004]. With this information, it is clear that Phoenix should certainly observe these light- weight non-methane hydrocarbons in its analysis. Again, ethane had the highest peak mixing ratio of 6.0 ppbv followed by i-pentane (5.5 ppbv), n-butane (5.1), ethene (5.0), and propane (4.9). These maxima occurred coincident with the lowest O_3 mixing ratio observation at 0300-0400 CDT 7 May. With little to no O_3 available to oxidize C_2-C_5 hydrocarbons into light-weight OVOCs such as formaldehyde, NO_x chemistry dominates. Primarily, NO_3 reacts with unsaturated hydrocarbons forming mostly organic nitrates, which results in production of additional hydrocarbons depending upon the initial concentration of O_3, which produces NO_2 and NO_3 after sunset and the speed of the low-level nocturnal jet maximum [*Stutz et al.*, 2010; *Talbot et al.*, 2005].

Overall, during the daylight hours all compounds measured remain nearly constant with a few exceptions. At 1000 6 May, a number of hydrocarbons exhibit daytime maxima, including toluene (0.46 ppbv), ethyne (0.48), i-pentane (0.49), n-pentane (0.50), and i-butane (1.3). The daytime mean for these compounds on 6 May were 0.17, 0.55, 0.33, 0.25, and 0.23 ppbv, respectively. A shift in the surface wind direction occurred at this same time (Figure 5.2b) from primarily out of the SW to WNW where it remained throughout the remainder of the day. Further analysis is required to determine the source of this daytime maximum, but it is certainly of note.

With respect to halogens, OCS had the highest mean mixing ratio during the sampling period of 0.39 ppbv with the remainder of the halocarbons being carbon tetrachloride (0.094), dichloromethane (0.69), chloroform (0.042), tetrachloroethylene

(0.036), and trichloromethane (0.029). These values are one to two orders of magnitude less than the hydrocarbons, yet the C_6-C_7 aromatics (benzene (0.22 ppbv) and toluene (0.38)) fall within the range of these means. Also, OCS exhibits little variability throughout the sampling period with a mean of 0.39 ppbv, a maximum of 0.49 ppbv, and a minimum of 0.29 ppbv. These factors indicate a lack of local sources for these compounds. We hypothesize that given the sampling location the background values in Huntsville for the halocarbons and aromatics would be even lower. Additional sampling is required to test this hypothesis.

Nighttime maxima of tetrachloroethylene (0.26 ppbv), trichloromethane (0.030), and dichloromethane (0.26) coincide with the 0300-0400 CDT 7 May maximum in several hydrocarbons. This evidence indicates the possibility of nocturnal horizontal transport from a like source to the NNE (Figure 5.2b and Figure 5.4c). Verification of this hypothesis would require back trajectory analysis.

e. Phoenix Batch Sample Analysis

During the same sampling period, Phoenix collected batch samples coincident to the canister samples described in §IV.*a*. However, due to several instrument- and process control-level malfunctions, these measurements did not prove useful for comparison. Therefore, to characterize and quantify the capabilities of Phoenix additional ambient samples from the NSSTC rooftop will be required to provide critical proof-of-concept data. Measurements of carbon tetrachloride provide internal calibration as the ambient mixing ratio of this compound experiences little variability. Figure 5.11 shows during the 5-7 May sampling period CCl_4 ranged between 81-103 pptv with little variability (variance = 38.1 pptv).

Phoenix autonomously collected batch samples on 12-18 September 2011 from the NSSTC roof via Teflon® inlet tube into the RACPD laboratory. Water and CO_2 trapping took place prior to insertion into the cryotrap maintained at -150 °C. The cryotrap collected samples for four hours at the hours of 200, 600, 1000, 1400, 1800, and 2200 CDT prior to thermal desorption at 100 °C into the gas cell via UHP N_2 carrier to a pressure of ~760 torr. Thermocouples monitored cryogenic, valve, gas cell, and ambient temperatures for safety and operational set points. The FTIR collected one five-minute co-added background spectrum every 24 hours and one five-minute co-added cryotrapped specturm every four hours at 1 cm^{-1} resolution with Boxcar apodization and Mertz 2x zerofilling. Refer to the Appendix for all the spectral files collected during the sampling period. Mass flow controllers and meters controlled and monitored the pertinent flow rates for quantification. Pressure transducers monitored gas cell and flow pressures for safety and process repeatability.

Figures 5.12-5.15 presents the derived mixing ratio data for the 12-18 September sampling period. In general, a diurnal pattern is immediately evident. Maximum observed values occur during the nighttime hours when a shallow nocturnal boundary layer reduces vertical mixing and horizontal transport and a decrease in O_3 due to NO_x chemistry removes O_3 and OH, key hydrocarbon oxidants. Minimum observed values occur during the day time hours when the convective boundary layer encourages vertical mixing and horizontal transport and increases in O_3 and O_3 photolysis provides oxidants for hydrocarbon removal (see R1-R8 in §II.*a*).

Specifically, Figure 5.12 groups the alkene observations into one figure. All three compounds share similar observational structure with correlations coefficients (R^2)

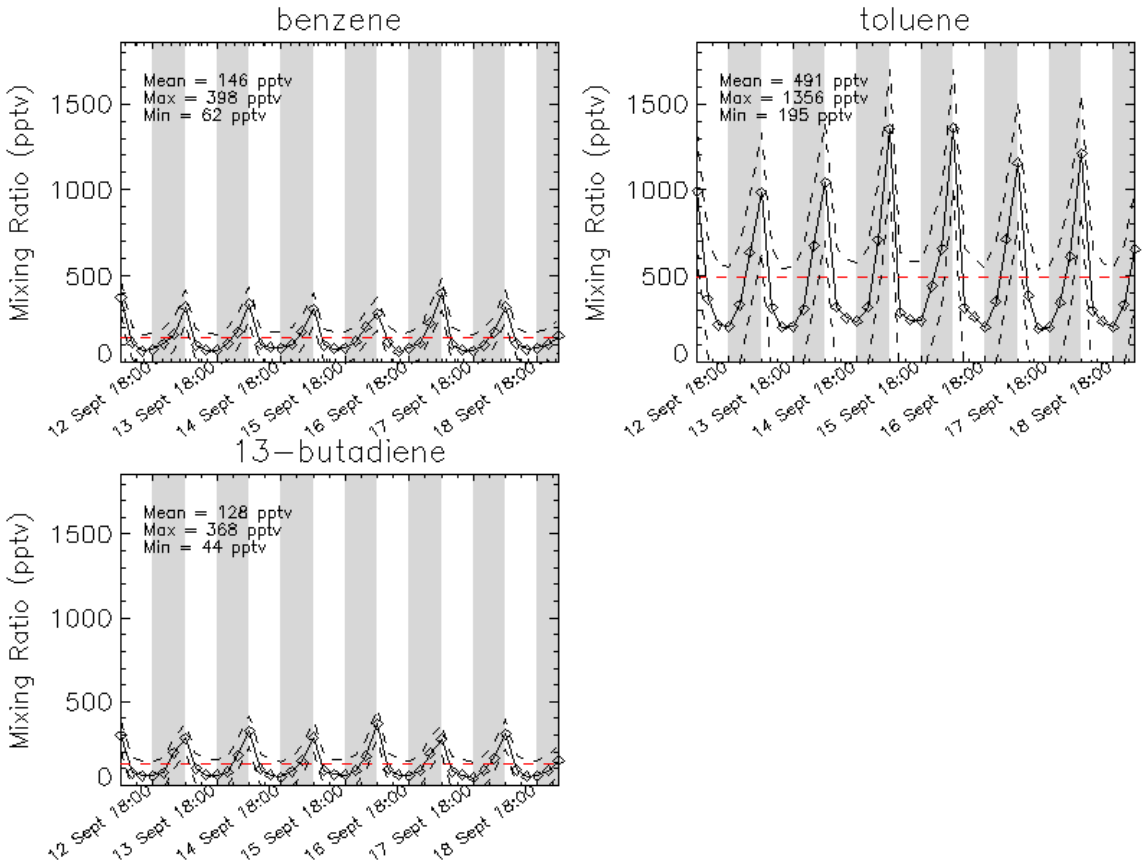

Figure 5.12. Phoenix batch sample measurements of benzene, toluene, and 1,3-butadiene on 12-18 September 2011. Red dashed lines indicate the average mixing ratio during the sampling period. Black dashed lines represent +/-1σ standard deviation. Grey shading indicates nighttime hours (1800-600 CDT).

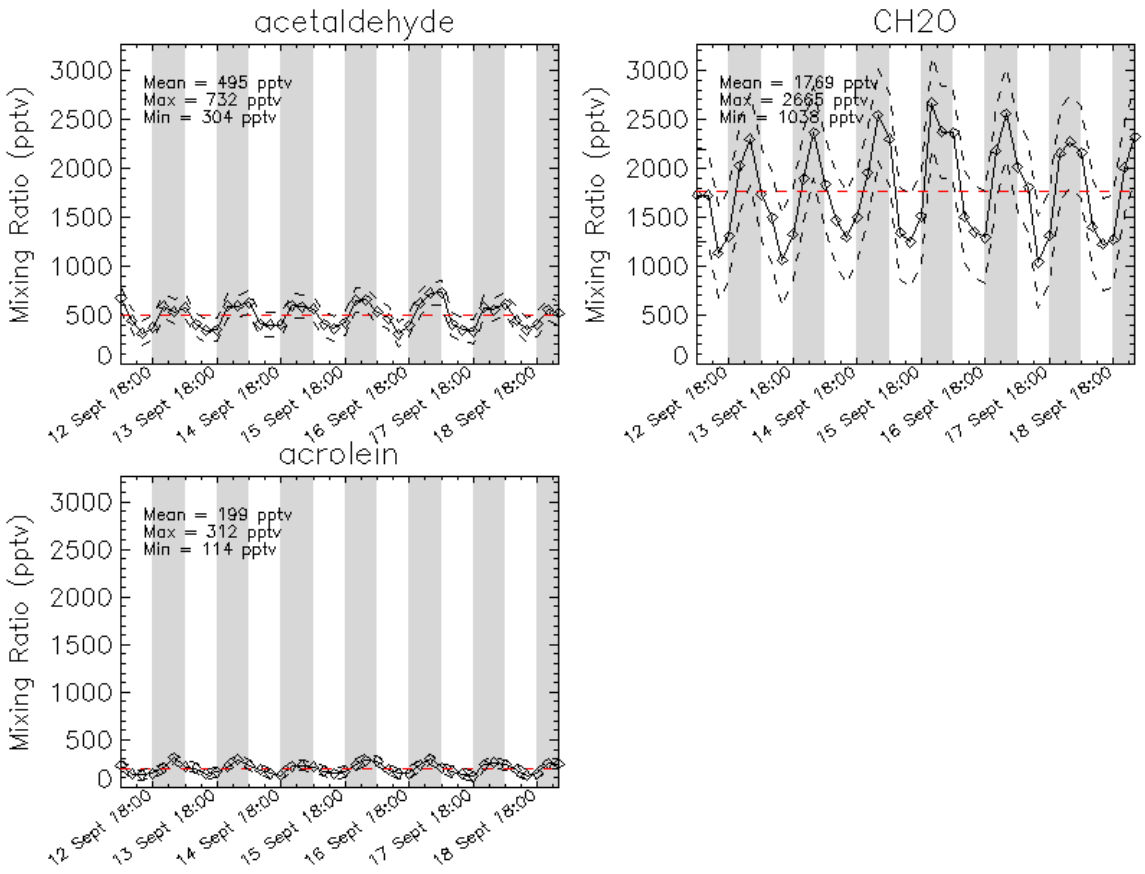

Figure 5.13. Phoenix batch sample measurements of acetaldehyde, formaldehyde, and acrolein on 12-18 September 2011. Red dashed lines indicate the average mixing ratio during the sampling period. Black dashed lines represent +/-1σ standard deviation. Grey shading indicates nighttime hours (1800-600 CDT).

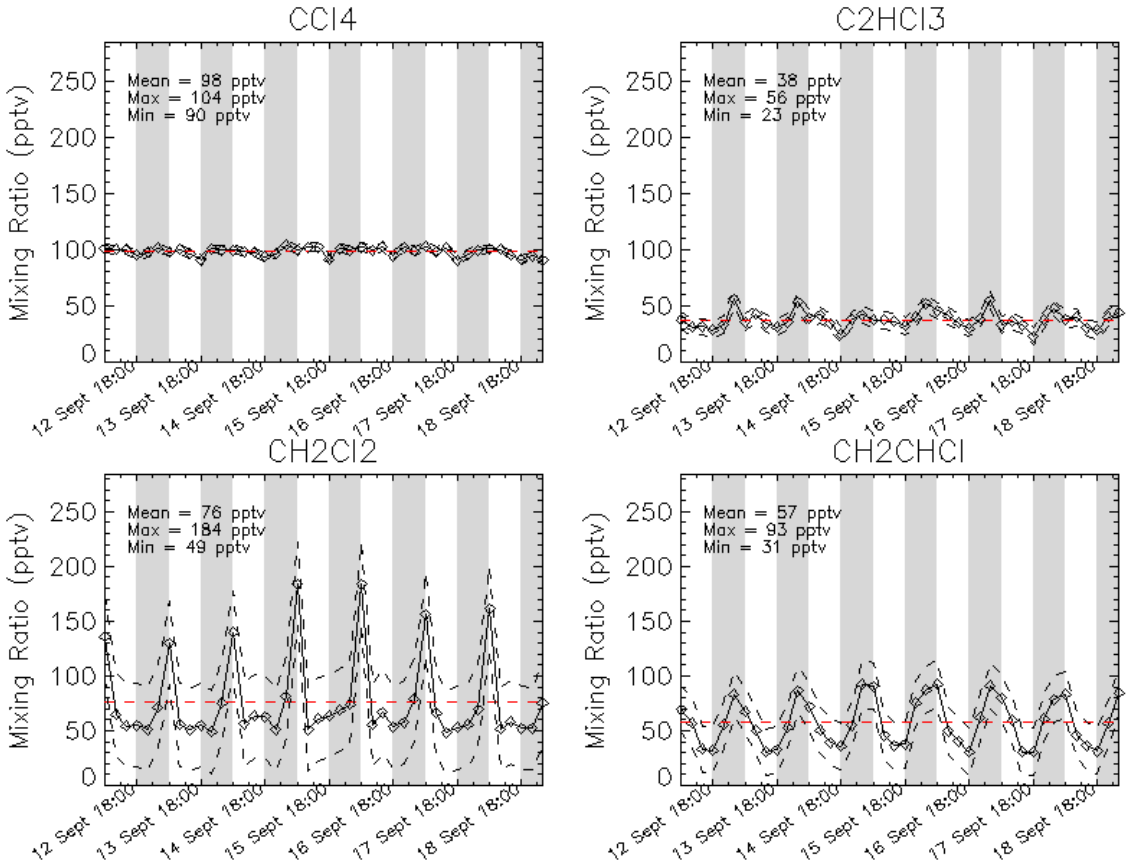

Figure 5.14 Phoenix batch sample measurements of carbon tetrachloride, trichloromethane, dichloromethane, and vinyl chloride on 12-18 September 2011. Red dashed lines indicate the average mixing ratio during the sampling period. Black dashed lines represent +/-1σ standard deviation. Grey shading indicates nighttime hours (1800-600 CDT).

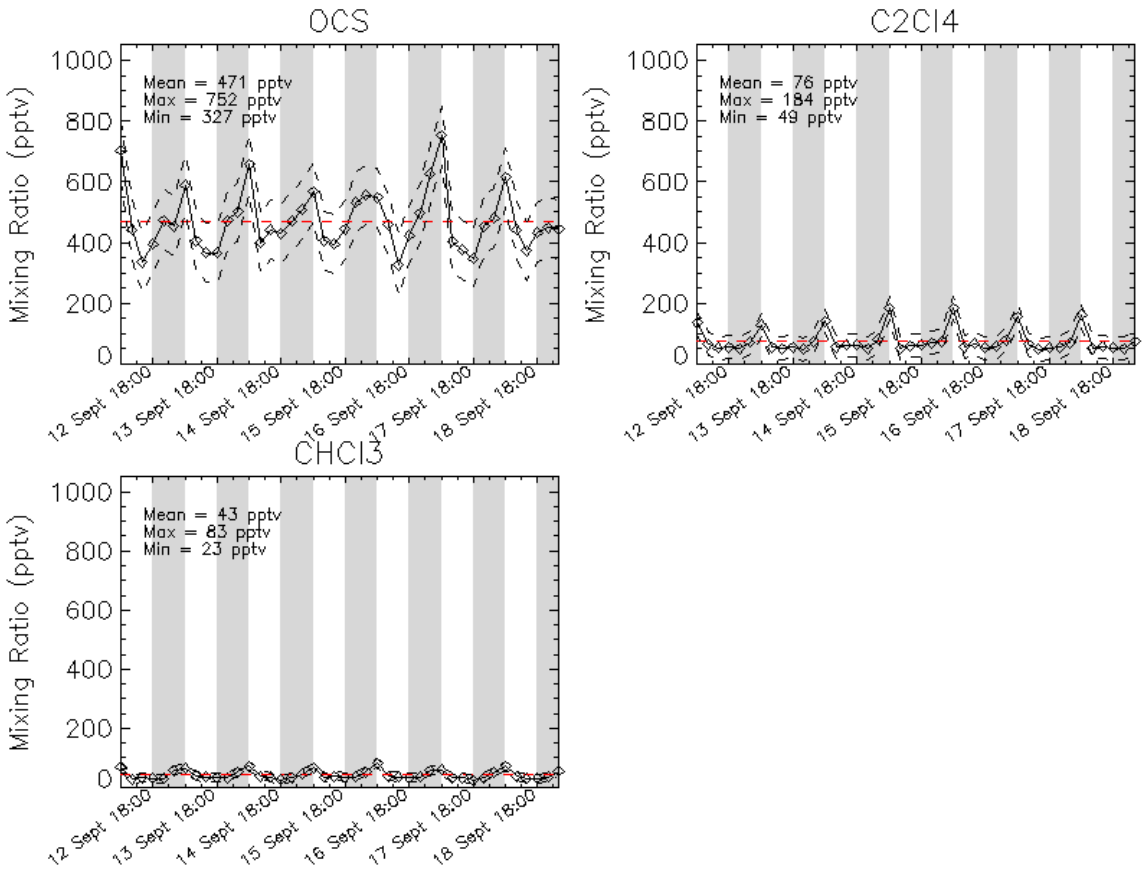

Figure 5.15. Phoenix batch sample measurements of carbonyl sulfide, tetrachloroethylene, and chloroform on 12-18 September 2011. Red dashed lines indicate the average mixing ratio during the sampling period. Black dashed lines represent +/-1σ standard deviation. Grey shading indicates nighttime hours (1800-600 CDT).

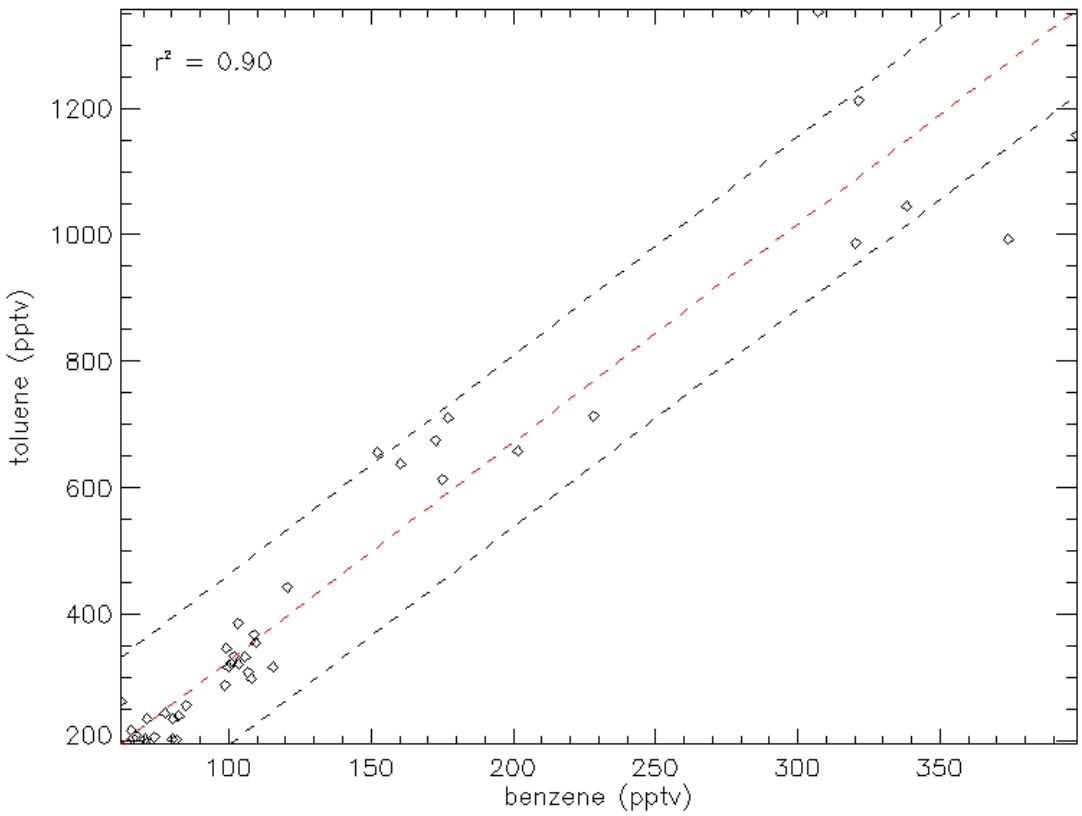

Figure 5.16. Scatter plot comparing Phoenix batch sample observations of toluene and benzene mixing ratio for 12-18 September 2011. The red dashed line represents the 1:1 line of the scatter plot. Black dashed line represents +/- 1-σ standard deviation. The correlation coefficient (R^2) is indicated in the upper left.

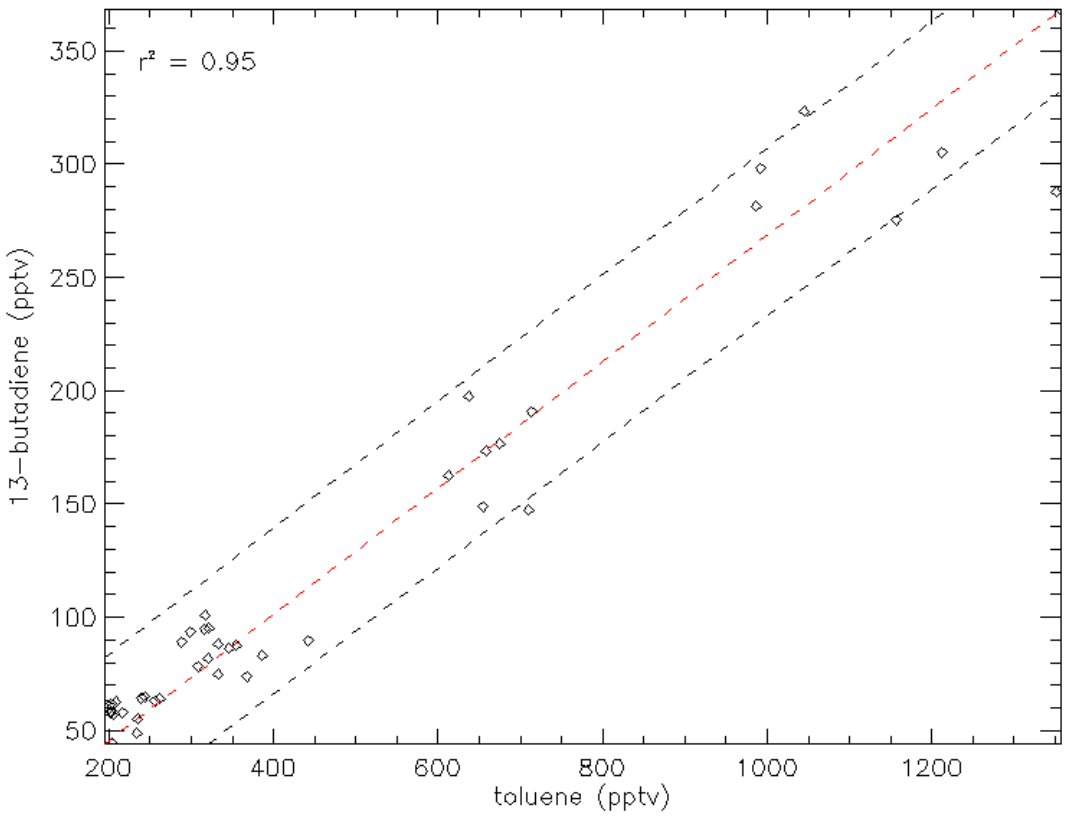

Figure 5.17. Scatter plot comparing Phoenix batch sample observations of 1,3-butadiene and toluene mixing ratio for 12-18 September 2011. The red dashed line represents the 1:1 line of the scatter plot. Black dashed line represents +/- 1-σ standard deviation. The correlation coefficient (R^2) is indicated in the upper left.

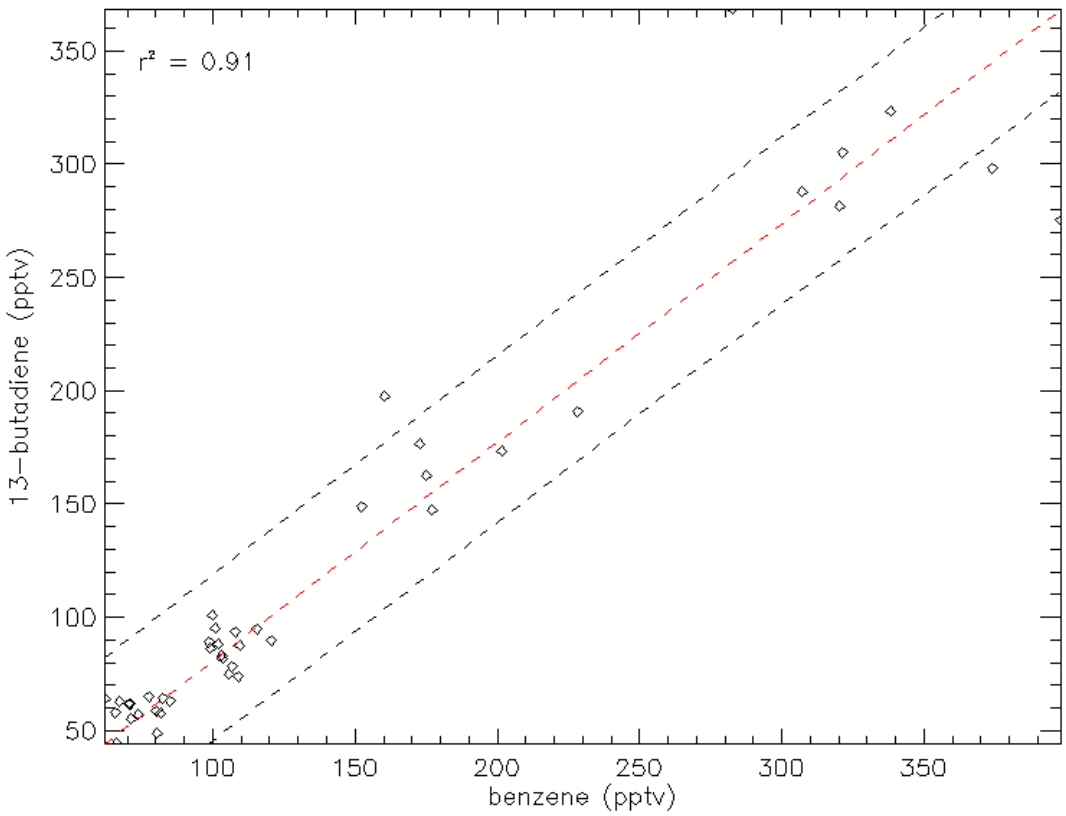

Figure 5.18. Scatter plot comparing Phoenix batch sample observations of 1,3-butadiene and benzene mixing ratio for 12-18 September 2011. The red dashed line represents the 1:1 line of the scatter plot. Black dashed line represents +/- 1-σ standard deviation. The correlation coefficient (R^2) is indicated in the upper left.

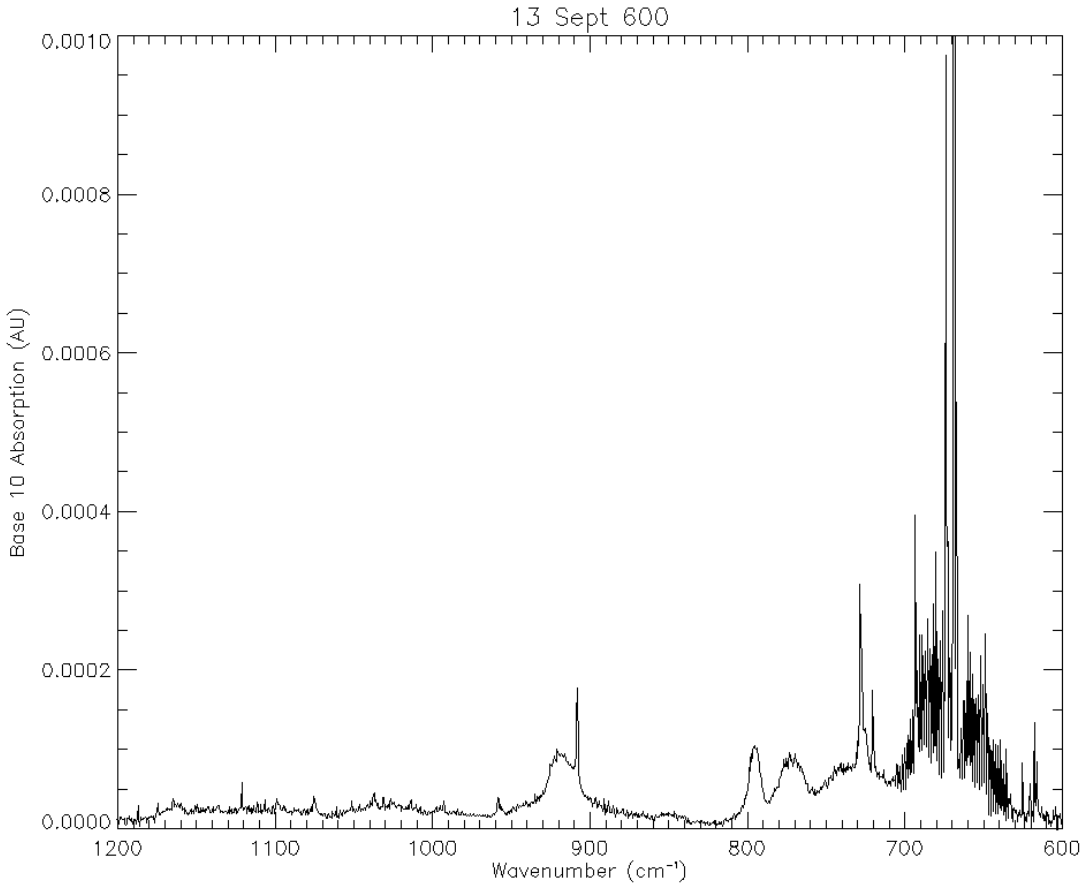

Figure 5.19. Observed IR spectrum between 1200-600 cm^{-1} for the batch sample collected on 17 September 2011 at 600 CDT. The ν_2 C-O bend dominates the 700-600 cm^{-1}band, which is used for benzene quantification.

of 0.90 for benzene and toluene (Figure 5.16), 0.95 for 1,3-butadiene and toluene (Figure 5.17), and 0.91 for 1,3-butadiene and benzene (Figure 5.18). Such high R^2 values suggest a common source, possibly direct emission from the tar roof top. Comparatively, the R^2 of the5-7 May 2011 canister samples was 0.98. A detailed source analysis is beyond the scope of this dissertation. Inspection of Figure 5.19 shows the C-O bending feature from untrapped CO_2 creates spectral interference in the 700-600 cm^{-1} range, even after spectral subtraction to reduce these effects. This interference reduces the accuracy for benzene retrievals at 674 cm^{-1} and for other alkenes with nearby spectral quantification features (Table 4.1). However, despite interference from the C-O bending feature, the correlations between alkenes is strong.

Figure 5.13 groups the OVOCs, specifically carbonyls, into one figure. Again, all three show similar observation structure with formaldehyde (CH_2O) dominating the total OVOC observations with a mean value 3.5 times greater than acetaldehyde and 8.9 times greater than acrolein. R^2 amongst the carbonyls are not as high as the alkenes. The R^2 between CH_2O and acetaldehyde is 0.70 (Figure 5.20), between CH_2O and acrolein is 0.78 (Figure 5.21), and between acetaldehyde and acrolein is 0.67 (Figure 5.22). Additionally, CH_2O mixing ratios exhibit more variance than the other two carbonyls observed, 2.2×10^5 pptv versus 1.5×10^4 pptv for acetaldehyde and 2.9×10^3 pptv for acrolein. This pattern is indicative of VOC oxidation leading ultimately to the formation of CH_2O and eventually H_2O and CO_2. However, OVOCs, particularly CH_2O, are difficult to observe using extractive methods, because of their propensity to adhere to plumbing surfaces and to react in the presence of co-collected oxidants. Passivation and cleaning reduces adhesion effects, but reactivity within the fluid system during desorption

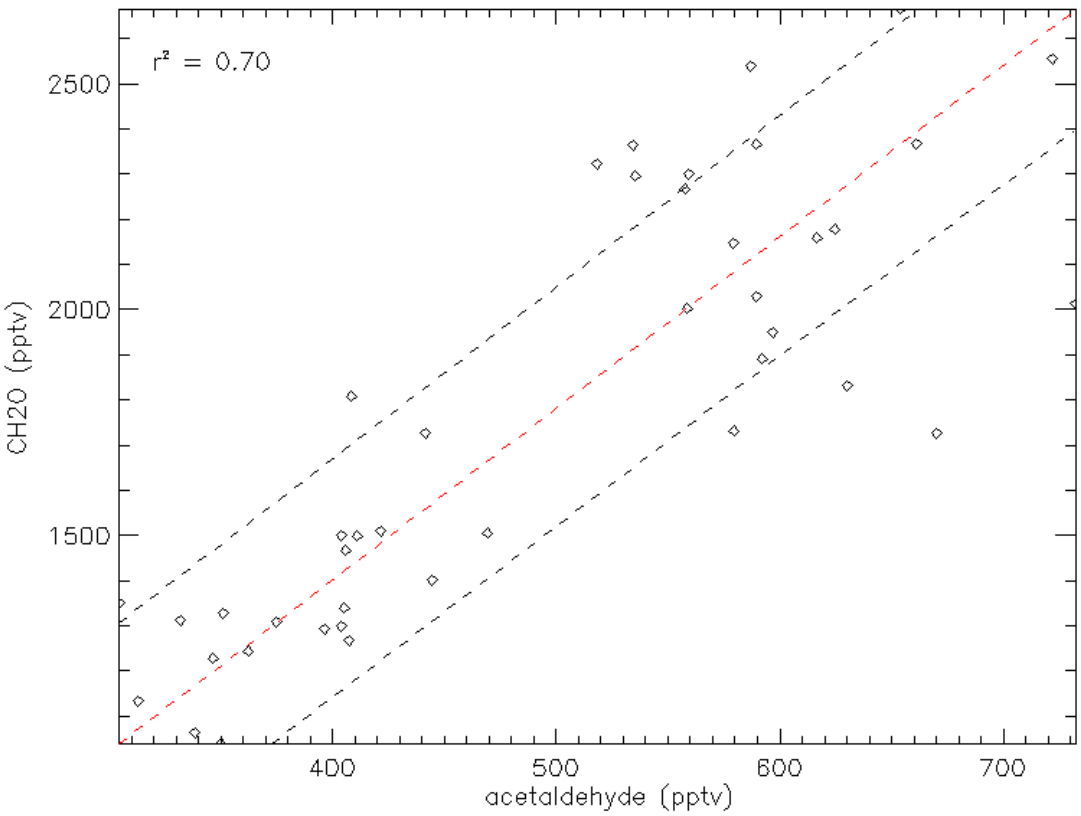

Figure 5.20. Scatter plot comparing Phoenix batch sample observations of CH_2O and acetaldehyde mixing ratio for 12-18 September 2011. The red dashed line represents the 1:1 line of the scatter plot. Black dashed line represents +/- 1-σ standard deviation. The correlation coefficient (R^2) is indicated in the upper left.

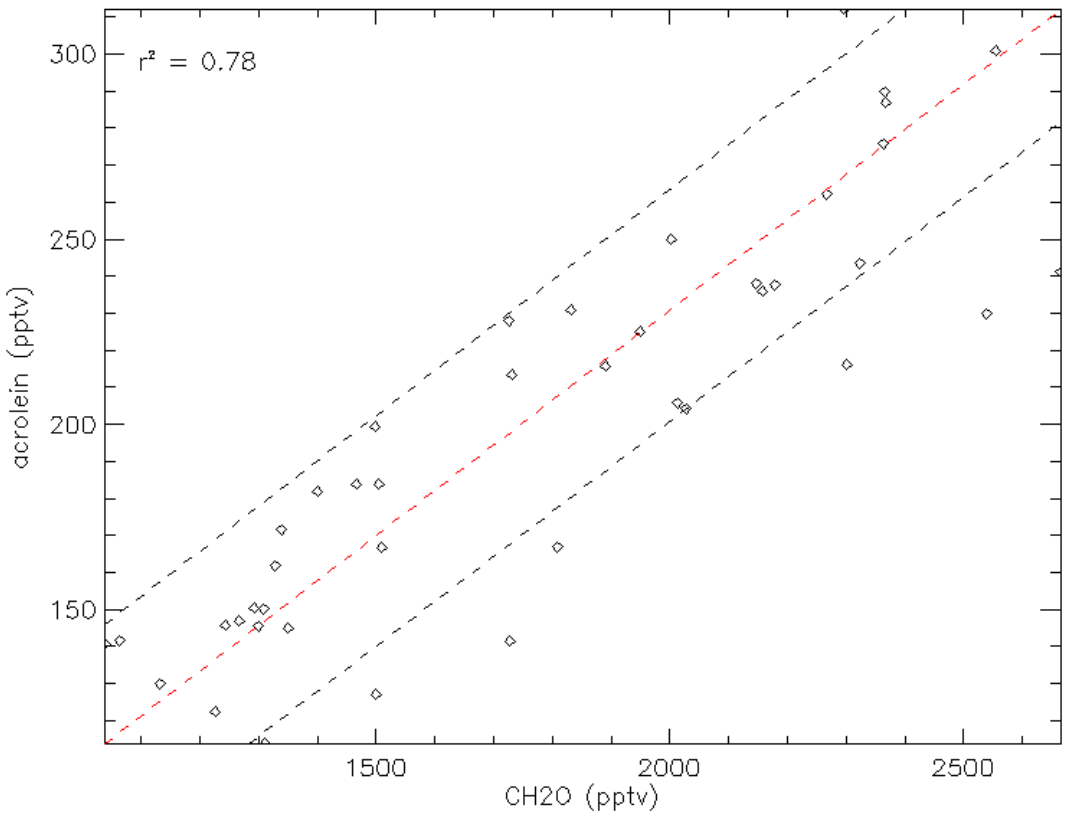

Figure 5.21. Scatter plot comparing Phoenix batch sample observations of acrolein and CH_2O mixing ratio for 12-18 September 2011. The red dashed line represents the 1:1 line of the scatter plot. Black dashed line represents +/- 1-σ standard deviation. The correlation coefficient (R^2) is indicated in the upper left.

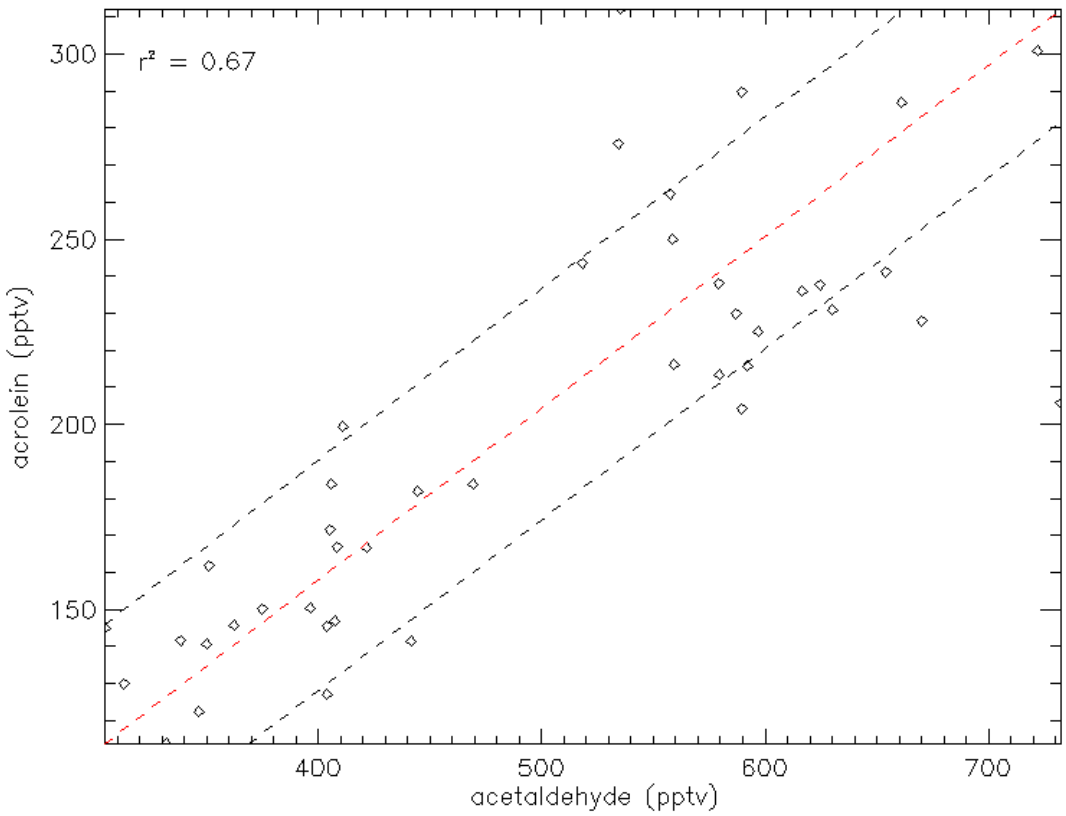

Figure 5.22. Scatter plot comparing Phoenix batch sample observations of acrolein and acetaldehyde mixing ratio for 12-18 September 2011. The red dashed line represents the 1:1 line of the scatter plot. Black dashed line represents +/- 1-σ standard deviation. The correlation coefficient (R^2) is indicated in the upper left.

has not yet been accurately quantified. Additional testing with UHP CH_2O standards is required to quantify and minimize this source of error prior to full autonomous field operations.

Figure 5.14 groups four C_1-C_2 halocarbons, specifically carbon tetrachloride (CCl_4), trichloroethylene (C_2HCl_3), dichloromethane (CH_2Cl_2), and vinyl chloride (CH_2CHCl). All four exhibit low mixing ratios indicating a lack of local source (e.g., local marine emissions, biomass burning). Dichloromethane exhibits the widest range of observations with a variance of 1440 pptv, compared to 451 pptv for vinyl chloride, 56.4 pptv for trichloroethylene, and 13.9 pptv for carbon tetrachloride. Figure 5.15 shows the remaining C_1-C_2 halocarbons, tetrachloroethylene (C_2Cl_4) and chloroform ($CHCl_3$) and one sulfur compound, carbonyl sulfide (OCS). Carbonyl sulfide exhibits the highest observation range of the compounds in Figure 5.15, with a mean mixing ratio of 471 pptv and a variance of 9.5×10^3 pptv. The variance of the observations of the remaining halocarbons is 1.7×10^3 pptv for tetrachloroethylene and 219 pptv for chloroform.

To perform internal calibration, Dr. Sive suggested comparing the entire carbon tetrachloride time series during the 12-18 September observations to the WAS measurements taken 5-7 May. As shown in Figure 5.11 the canister observations of carbon tetrachloride exhibit little variance (38.1 pptv) over a narrow range of observations (81-103 pptv) with a 1-σ standard deviation of 6.2 pptv. These observations suggest the absence of local emission sources. Therefore, the range observed in the canister measurements represents the background mixing ratio of carbon tetrachloride in Huntsville, AL. The same statistical analysis on the Phoenix observations of carbon tetrachloride between 12-18 September shows the observational range to be analogous

(90-104 pptv) with a 1-σ standard deviation of 3.7 pptv and a variance of 13.9 pptv, both slightly lower than the canister measurements. These comparable statistics indicate Phoenix is functioning properly with adequate selectivity. However, in order to accurately quantify the agreement between Phoenix batch samples and a well-established observational technique such as canister collection and analysis by GC/ECD/FID, both methods need to collect data at the same time in the same air mass.

f. Error Analysis

In order to perform a thorough error analysis on the current Phoenix system, the first step was to convert the PNNL library spectra into the units appropriate for this method. PNNL reports absorption cross sections in units of ppm^{-1} m^{-1} in base-10, which needs to be converted to cm^2 $molecule^{-1}$ to be compatible with Beer's Law. The appropriate conversion comes from the inverse of Loschmidt's constant at 25 °C and 1 atm. Loschmidt's constant is defined as

$$n_0 = \frac{p_0}{k_B T_0}, \tag{5.6}$$

where k_B is the Boltzmann Constant of 1.381 x 10^{-23} J K^{-1}.

$$n_0 = \frac{1.01325x10^5 Pa}{1.381x10^{-17} Pa \cdot cm^{-3} * 298\ K} = 2.5x10^{19} molec \cdot cm^{-3}. \tag{5.7}$$

For a mixing ratio in ppmv and converting mixing ratio to concentration yields a value of 4.0 x 10^{16}, of which the inverse is desired. Therefore, the PNNL unit conversion is 4.0 x 10^{-16}. Applying this conversion factor to the PNNL library spectrum

$$\sigma(cm^2 molec^{-1}) = \sigma(ppm^{-1} m^{-1}) * 4.0x10^{-16}$$

produces a base-10 absorption cross section profile in units of cm^2 $molecule^{-1}$.

However, the FTIR used to collect the PNNL-derived cross sections is not identical to the Phoenix FTIR. The PNNL FTIR is a high-resolution, vacuum-purged Bruker IFS 66v/s fitted with wedged KBr, KCl, or ZnSe windows to prevent interference from cross-parallel windows, a photoconductive MCT detector, and a 19.94 cm gas cell fitted with gold plated windows. In short, the instrument line shape (ILS) of the PNNL spectrometer is fundamentally different than the ILS of the Phoenix FTIR.

In order to use the PNNL spectral library with the Phoenix spectra, the PNNL cross section profiles need to be deresolved to match the Phoenix resolution. First a Gaussian convolution algorithm degrades the spectral resolution to the desired value of 1.0 cm^{-1}. Once deresolved, the Phoenix ILS is applied to account for the inherent absorption of the components of the Phoenix FTIR. The Phoenix algorithm obtains the ILS by evacuating the gas cell and collecting a background and sample spectrum with minimal interference (purged and desiccated optical path, no lights on in the lab, air handlers shut off). This process reduces the PNNL library spectra to Phoenix resolution and applies Phoenix instrument characteristics. However, this method causes 'smearing' of the major absorption features presenting error into the analysis method.

With the deresolution error characterized, it becomes a correction applied to the quantitative algorithm. To quantify the error associated with deresolving the PNNL spectra, a comparison between the PNNL toluene spectrum at 0.1 cm^{-1} to a deresolved spectrum at 1.0 and 4.0 cm^{-1} was performed. Figure 5.23 shows these results across the entire spectral range. Upon cursory glance, the library and deresolved spectra look very similar, especially in the C-H stretching feature around 3000 cm^{-1}. However, closer

inspection reveals strong narrow absorption features at high resolution become weaker and broader at coarse resolution (Figure 5.23 inlay). The maximum absorption cross

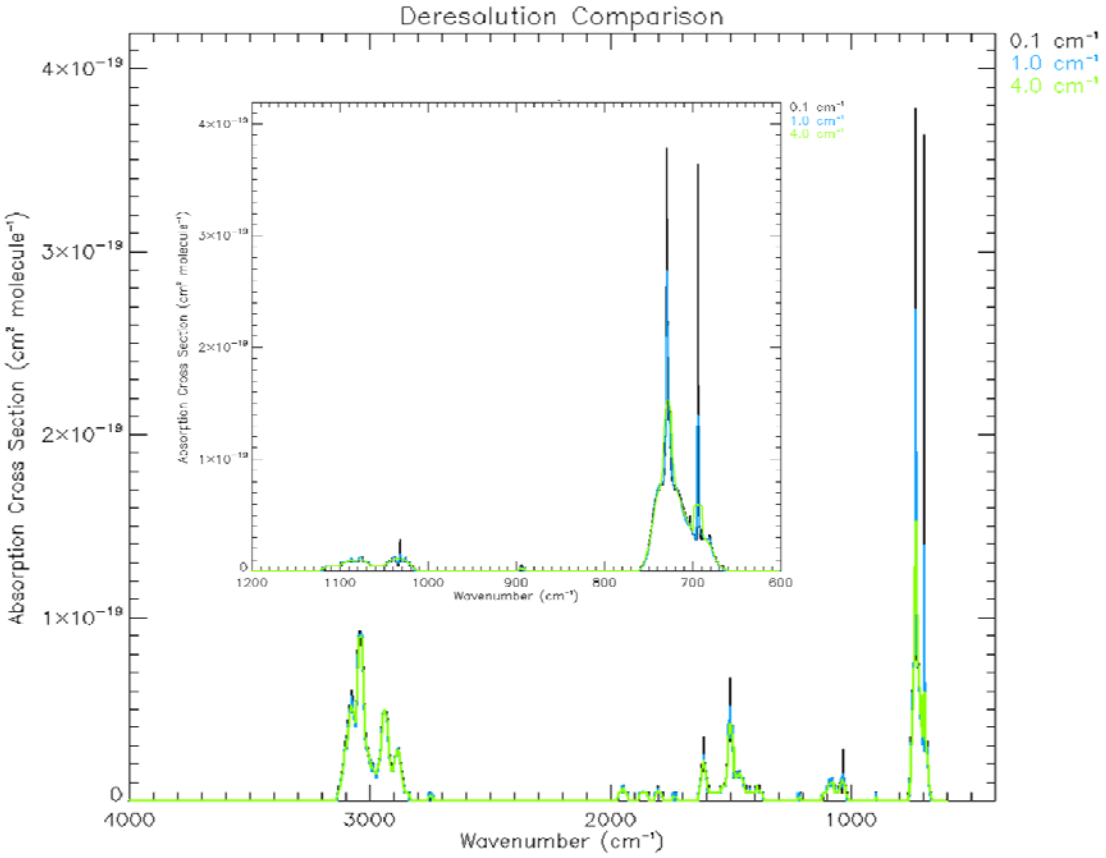

Figure 5.23. Results of deresolving the PNNL 0.1 cm^{-1} spectral files to 1.0 cm^{-1} (blue trace) and 4.0 cm^{-1} (green trace). Inlaid is the same information zoomed in to 1200-600 cm^{-1}.

section in base-10 between 745-720 cm^{-1} for the PNNL 0.1 cm^{-1} spectrum is 4.2 x 10^{-19} cm^2 $molecule^{-1}$. For the 1.0 and 4.0 cm^{-1} deresolved spectra the maximum absorption cross section in base-10 between the same spectra range is 3.7 x 10^{-19} and 2.8 x 10^{-19} cm^2 $molecule^{-1}$, respectively. The location of the absorption cross section maximum in each case is coincident at 694 cm^{-1}. Assuming the absorption at 694 cm^{-1} is 0.2 AU for a measured spectrum, the concentration calculation using Beer's Law would work out to be

$$C_{0.1cm} = \frac{0.2}{0.42x10^{-18}}\frac{1}{1000} = 4.8x10^{14}\ molecules\ cm^{-3}$$

$$C_{1.0cm} = \frac{0.2}{0.37x10^{-18}}\frac{1}{1000} = 5.4x10^{14}\ molecules\ cm^{-3}$$

$$C_{4.0cm} = \frac{0.2}{0.28x10^{-18}}\frac{1}{1000} = 7.1x10^{14}\ molecules\ cm^{-3}$$

Using the PNNL 0.1 cm^{-1} library spectrum as 'truth', the difference in concentration between the 'truth' and the 1.0 cm^{-1} spectrum is 6.4 x 10^{13} molecules cm^{-3} and between the 'truth' and the 4.0 cm^{-1} spectrum is 2.4 x 10^{14} molecules cm^{-3}. This represents a percent difference of 14% for the 1.0 cm^{-1} deresolved spectrum and 50% for the 4.0 cm^{-1} deresolved spectrum. From this analysis it is clear the best method would be to obtain instrument-specific library spectra for all of the compounds listed in Table 4.1. However, this was not tractable at the time of this analysis. Therefore, it is critical to account for this difference in each individual compound. For toluene, a correction of 11.9% is applied in the quantification algorithm. For the remaining deresolution corrections, see Table 5.1.

Realistic assessments of this spectral analysis algorithm require complicated spectra with overlapping features from diverse trace gas mixtures similar to those in the

Table 5.1. List of corrections resulting from deresolution of PNNL 0.1 cm^{-1} spectra to 1.0 cm^{-1} Phoenix resolution for use in the quantitative algorithm.

	1,3-Butadiene	Benzene	Acrolein	Acetaldehyde	Carbon Tet
Wavenumber Peak (cm^{-1})	908	674	959	1103	795
Library α (x $10^{-18}cm^2\,molec^{-1}$)	0.613	5.43	0.22	0.032	2.16
1.0 cm^{-1} α (x $10^{-18}cm^2\,molec^{-1}$)	0.48	2.42	0.14	0.032	2.14
Difference (x $10^{-18}cm^2\,molec^{-1}$)	0.133	3.01	0.08	0	0.02
Percent Difference	21.7%	55.4%	36.4%	0.0%	0.9%

	OCS	Chloroform	Dichloromethane	Formaldehyde
Wavenumber Peak (cm^{-1})	868	772	750	1121
Library α (x $10^{-18}cm^2\,molec^{-1}$)	0.012	1.08	3.34	0.032
1.0 cm^{-1} α (x $10^{-18}cm^2\,molec^{-1}$)	0.008	1.08	3.34	0.024
Difference (x $10^{-18}cm^2\,molec^{-1}$)	0.004	0	0	0.008
Percent Difference	33.3%	0.0%	0.0%	25.0%

	Tetrachloroethylene	Trichloroethylene	Toluene	Vinyl Chloride
Wavenumber Peak (cm^{-1})	916	851	726	942
Library α (x $10^{-18}cm^2\,molec^{-1}$)	0.57	0.43	0.42	0.35
1.0 cm^{-1} α (x $10^{-18}cm^2\,molec^{-1}$)	0.57	0.44	0.37	0.34
Difference (x $10^{-18}cm^2\,molec^{-1}$)	0	-0.01	0.05	0.01
Percent Difference	0.0%	-2.3%	11.9%	2.9%

real atmosphere. However, Phoenix did not provide usable data during the 5-7 May validation runs with the WAS canisters. In the absence of FTIR data from the real atmosphere, the best alternative is creating synthetic spectra representative of the real atmosphere. Creation of such spectra is straightforward, using a modified version of Equation (3.3) with measured mixing ratios from the WAS canisters and deresolved absorption cross section spectra from PNNL. In order to represent the range of high and low mixing ratios observed during the sampling period, this exercise uses the mixing ratios from 1200 CDT 6 May to represent a noon-time observation and 0000 CDT 7 May to represent a midnight observation. To avoid additional confusion, only compounds coincident to Dr. Sive's canister observations and the Phoenix algorithm were utilized. Table 5.2 lists these compounds and their mixing ratios. A synthetic spectrum algorithm applies the mixing ratios in Table 5.1 divided by five to the PNNL spectra which *Sharpe et al.* [2004] generate at an average mixing ratio of 5 pptv. The algorithm produces base-10 absorption spectra devoid of water vapor to simulate ideal trapping conditions. Figure 5.24 shows the 1200 6 May and 0000 7 May synthetic spectra.

It is obvious from Figure 5.24 there is spectral overlap, which presents difficulties in quantifying dichloromethane (CH_2Cl_2), trichloroethylene (C_2HCl_3), and chloroform ($CHCl_3$). By subtracting tetrachloroethylene (C_2Cl_4), carbonyl sulfide (OCS), and carbon tetrachloride (CCl_4) from the absorption spectrum, the quantitative algorithm is able to better discern the remaining halocarbons. Applying the Phoenix spectral algorithm produces the results listed in Table 5.3. From the results shown in Table 5.3 Phoenix has the capability to accurately quantify a complex mixture of atmospheric VOCs at pptv levels.

Table 5.2. Mixing ratios from 1200 CDT 6 May (Column 3) and 0000 CDT 7 May (Column 4) canisters analyzed by Dr. Sive. The compounds listed are coincident with the Phoenix quantitative algorithm. Mixing ratios are in pptv.

Compound	Symbol	1200 LT MR	000 LT MR
benzene	C_6H_6	125	329
toluene	C_7H_8	77	626
dichloromethane	CH_2Cl_2	46.1	54.5
trichloroethylene	C_2HCl_3	2.2	22.4
chloroform	$CHCl_3$	19.8	64.3
tetrachloroethylene	C_2Cl_4	8.5	32.5
carbonyl sulfide	OCS	370	347
carbon tetrachloride	CCl_4	102	96

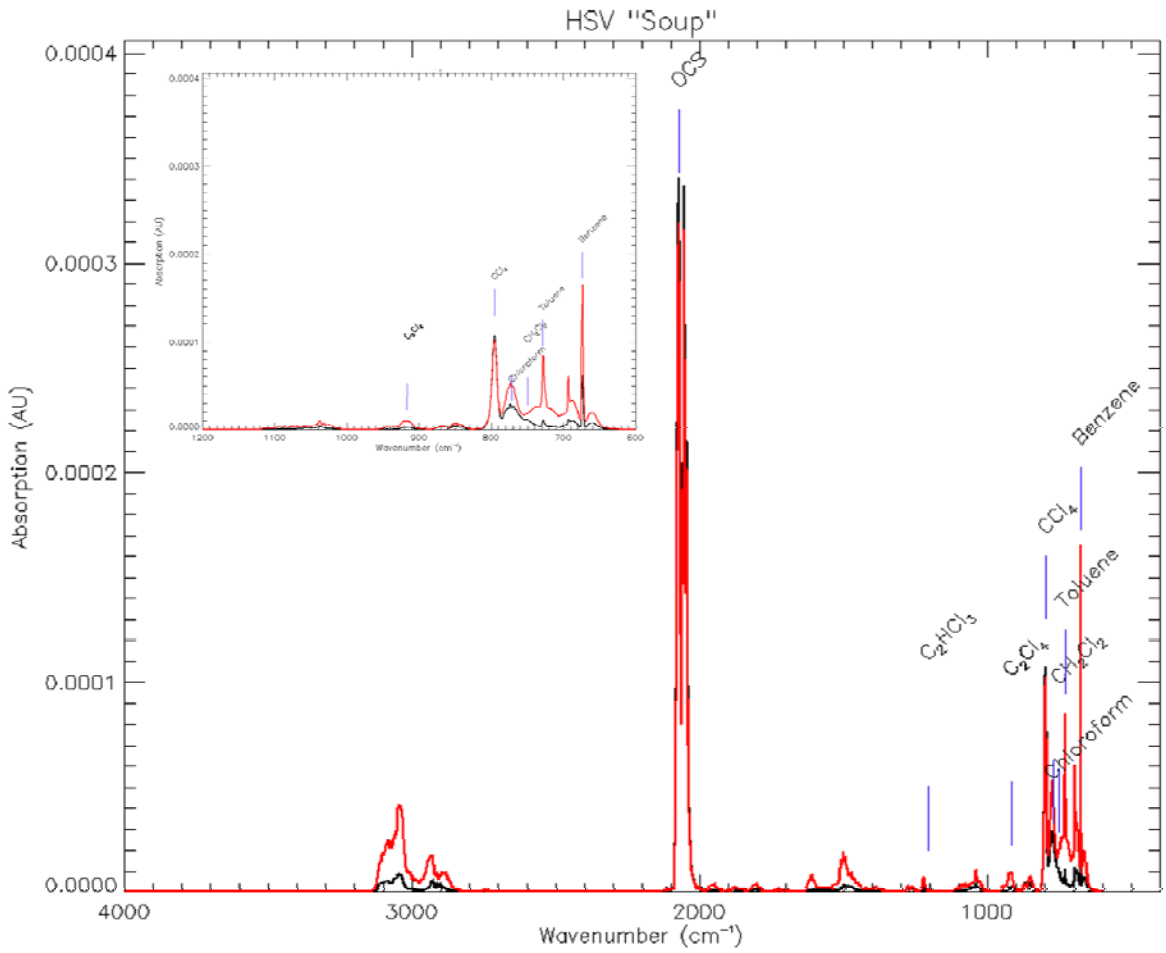

Figure 5.24. Absorption in base 10 versus wavenumber from synthetic spectra built using the mixing ratios derived from the ambient canister samples from 1200 LT 6 May (black trace) and 0000 LT 7 May (red trace). Compound labels correspond to the individual compound-specific peaks. Inlaid is a zoom between 1200-600 cm^{-1}.

Table 5.3. Results of applying the Phoenix quantification algorithm to synthetic spectra generated using mixing ratios in Table 5.2 and PNNL library spectra for each compound. Columns 2, 3, 5, and 6 list mixing ratios in pptv. Percent difference is $(\eta_{canister} - \eta_{phoenix}) / \eta_{canister}$.

Compound	1200 LT MR - Sive	1200 LT MR - Phoenix	Percent Diff	000 LT MR - Sive	000 LT MR - Phoenix	Percent Diff
cabonyl sulfide	370	369.7	-0.1%	347	346.7	-0.1%
benzene	125	126.5	1.2%	329	335.4	1.9%
tetrachlor.	8.5	8.6	1.2%	32.5	33.4	2.8%
carbon tetrachloride	102	103.4	1.4%	96	98.5	2.6%
toluene	77	81.1	5.3%	626	634.8	1.4%
dichlorometh.	46.1	52.8	14.5%	54.5	63.1	15.8%
chloroform	19.8	24.5	23.7%	64.3	69.5	8.1%
trichloroeth.	2.2	2.8	27.3%	22.4	28.2	25.9%

The next step in assessing the overall accuracy of the quantitative algorithm is to apply it to known concentrations of several target compounds. The current Phoenix quantitative algorithm works using peak fitting. Ideally, the quantitative algorithm would use the entire spectral range using a non-linear least squares approach similar to the approach described in §III.*c*. However, due to unavoidable time constraints, the quantitative methodology was simplified to peak fitting.

First, the absorption cross section profile in base-10 for each compound in Table 4.1 is derived using the method described earlier in this section. The algorithm locates the peak absorption cross section and the corresponding peak wavenumber, and applies Beer's law using these quantities. The first use of the Phoenix quantitative algorithm calculated mixing ratios for a mixture of 1 ppbv 1,3-butadiene (C_4H_6) and benzene (C_6H_6) in N_2. This calibration mixture came from Spectra Gases (Stewartsville, NJ) with +/- 10% accuracy. The calibration procedure input the gas directly into the gas cell for spectral analysis at 4 cm^{-1} resolution for five minute co-addition. Figure 5.25 shows the results of this analysis. The location of the absorbance peak associated with benzene is 673 cm^{-1} and with 1,3-butadiene is 909 cm^{-1}. The peak absorbance is 0.0182 AU and 0.0073 AU for benzene and 1,3-butadiene respectively. From Table 4.1 the absorption cross section, σ, for benzene is 2.4 x 10^{-18} cm^2 $molecule^{-1}$ and the absorption cross section for 1,3-butadiene is 4.8 x 10^{-19} cm^2 $molecule^{-1}$. In both cases the path length, *b*, of the gas cell is 1000 cm. Applying these values to Beer's Law gives

$$C_{C6H6} = \frac{A_{C6H6}}{\sigma_{lib}} * \frac{1}{b} = \left(\frac{0.0182}{2.42x10^{-18}}\right) * \frac{1}{1000} = 7.52x10^{12} molecules\ cm^{-3}$$

$$C_{C4H6} = \frac{A_{C4H6}}{\sigma_{lib}} * \frac{1}{b} = \left(\frac{0.0073}{0.48x10^{-18}}\right) * \frac{1}{1000} = 1.52x10^{13} molecules\ cm^{-3}$$

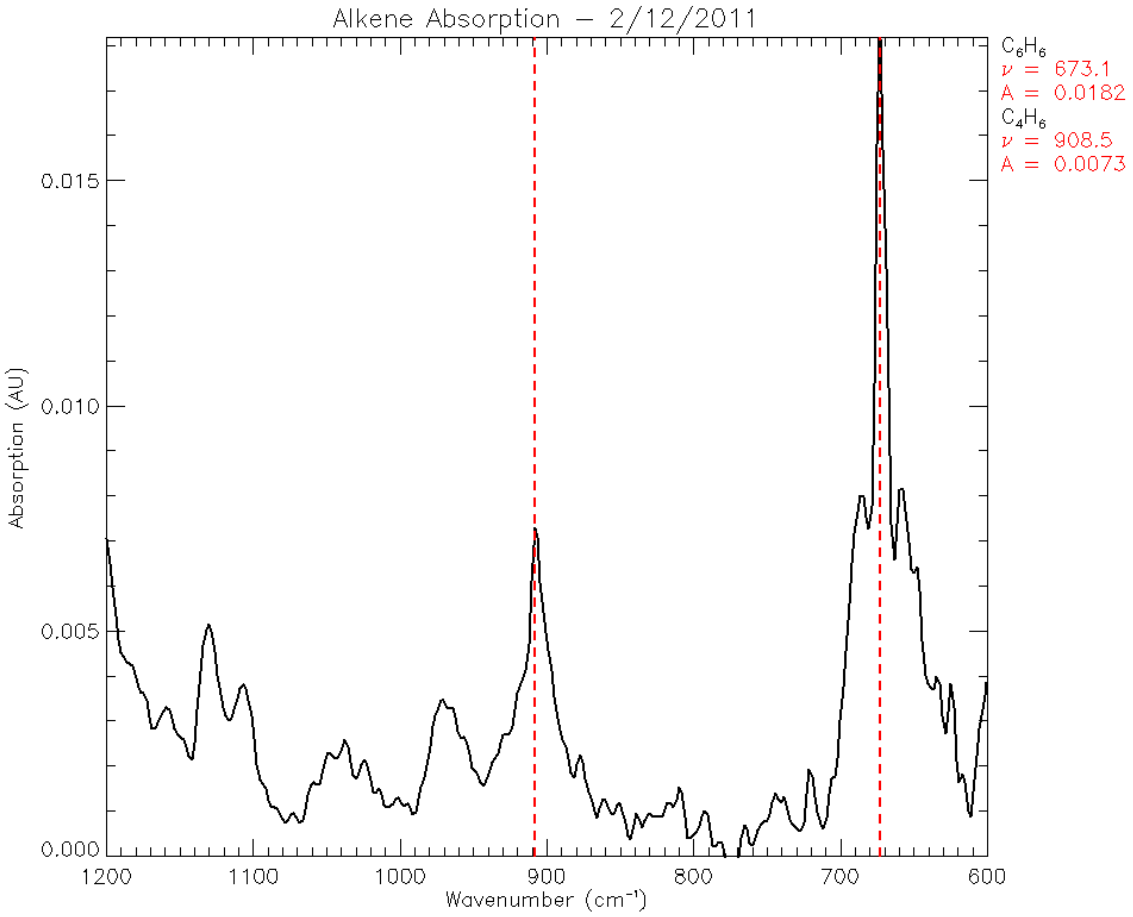

Figure 5.25. Base 10 absorption versus wavenumber for observations of calibration gas containing 1 ppbv of 1,3-butadiene (C_4H_6) and benzene (C_6H_6) in N_2. The vertical dashed lines indicate the location of the spectra peak used for quantification. The wavenumber (ν) in cm^{-1} of the peak and the peak base 10 absorption (A) in AU are listed on the right for each compound.

Converting to mixing ratio assuming $C_{air} = 2.5x10^{19} molecules\ cm^{-3}$ at 1 atm pressure and 25 °C

$$\eta_{C6H6} = \frac{C_{C6H6}}{C_{air}} = \frac{7.52x10^{12}}{2.5x10^{19}} = 0.301\ ppb$$
$$\eta_{C4H6} = \frac{C_{C4H6}}{C_{air}} = \frac{1.52x10^{13}}{2.5x10^{19}} = 0.608\ ppb$$
$$\eta_{total} = \eta_{C6H6} + \eta_{C4H6} = 0.909\ ppb$$

Calculating the percent error compared to the expected bottle concentration of 1 ppbv yields an error of 9.1%, which is within the accuracy range sited by the manufacturer. A preconcentrated measurement of this mixture would be ideal; however, the contents of the bottle emptied before that was possible.

Therefore, a second calibration gas bottle containing 100 ppmv toluene (C_7H_8) in air was obtained. The manufacturer (MESA Specialty Gases, Santa Ana, CA) sited an accuracy of +/- 2%. The calibration procedure input the gas directly into the gas cell for spectral analysis at 4 cm^{-1} resolution for five minute co-addition. Figure 5.26 shows the results of this analysis. The location of the absorbance peak associated with toluene is 3034 cm^{-1}. The peak absorbance is 0.22 AU. From Table 4.1 the absorption cross section of toluene is 0.09 x 10^{-18} cm^2 $molecule^{-1}$. Again, applying Beer's Law yields a concentration of

$$C_{C7H8} = \frac{A_{C7H8}}{\sigma_{lib}} * \frac{1}{b} = \left(\frac{0.22}{0.09x10^{-18}}\right) * \frac{1}{1000} = 2.49x10^{15} molecules\ cm^{-3.}$$

Converting to mixing ratio yields

$$\eta_{C7H8} = \frac{C_{C7H8}}{C_{air}} = \frac{2.49x10^{15}}{2.5x10^{19}} = 99.56\ ppm$$

which corresponds to a percent error of 0.44%, well within the manufacturer's reported

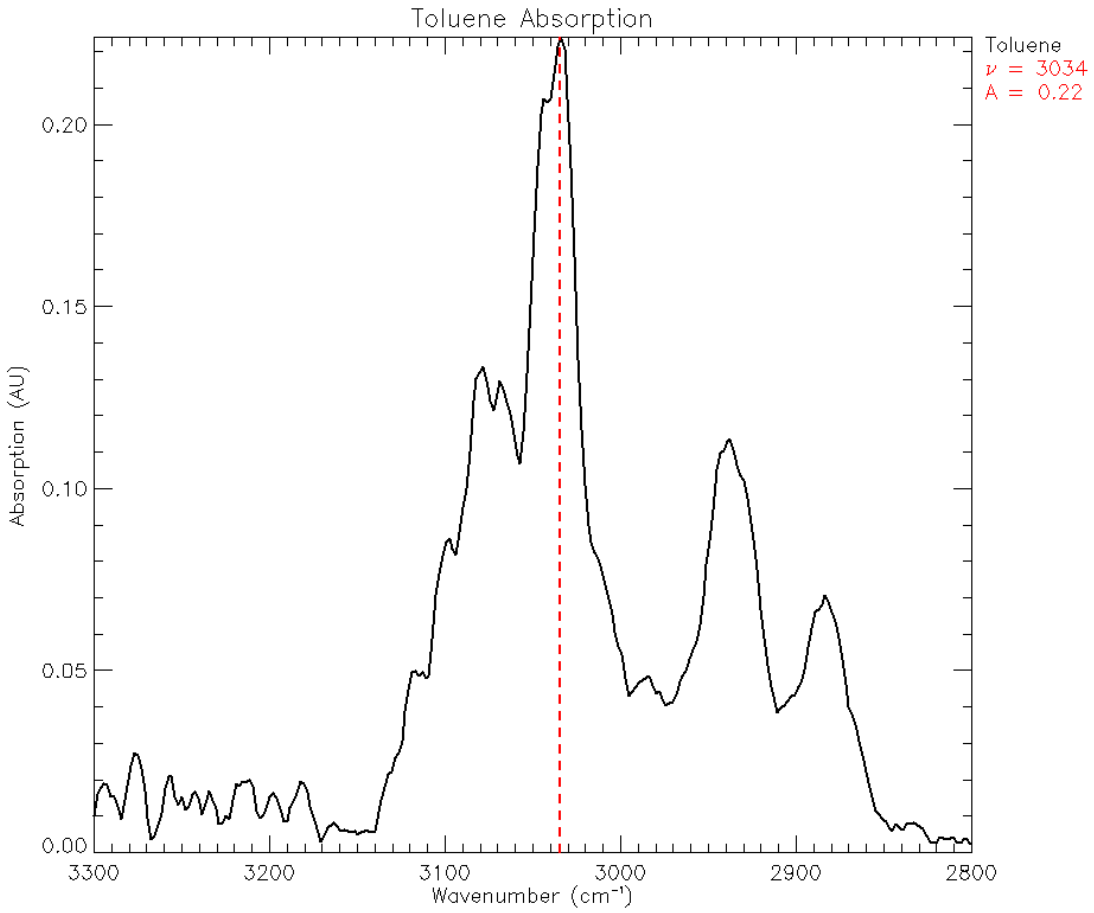

Figure 5.26. Base 10 absorption versus wavenumber for observations of calibration gas containing 100 ppmv of toluene (C_7H_8) in air. The vertical dashed lines indicate the location of the spectra peak used for quantification. The wavenumber (ν) in cm^{-1} of the peak and the peak base 10 absorption (A) in AU are listed on the right.

accuracy. It is clear from these calibration tests, the optical subsystem is observing the expected base 10 absorption spectrum, and the quantitative algorithm is accurately deriving the expected concentration within the accuracy sited by the manufacturer.

In order to quantify the repeatability of the Phoenix cryotrapping and desorption process, the calibration process control algorithm collected multiple preconcentrated spectra using the same toluene gas bottle diluted to 100 pptv using UHP N_2. The diluted toluene flowed through the -150 °C cryotrap for four hours, bypassing any water or CO_2 trapping in-line with the ambient inlet. After four hours, the heaters warmed the trap to 100 °C to revolatilize the sample, and UHP N_2 desorbed the trap into the gas cell until the cell pressure reached 760 torr. The FTIR obtained a five minute co-added spectrum at 1.0 cm^{-1}. The calibration algorithm repeated this same procedure four times. Figure 5.27 shows the results of this analysis. The mean mixing ratio across all four measurements is 107 pptv resulting into a mean percent error of 6.97 %. The variance is 1.51 pptv and the standard deviation 1.23 pptv. Again, the measurement accuracy is within the accuracy of the calibration bottle. Figure 5.28 shows the ratio of sample one (black trace) in Figure 5.27 to the mean of the remaining three spectra to illustrate the minor differences among the sample spectra. The central portion of Figure 5.28 shows relatively small variations about the 100% line, indicative of minor fluctuations in system noise. The larger deviations at larger and smaller wavenumbers indicate variations in trace gas (H_2O and CO_2) contamination in the external optical path from run to run.

To quantify the cryogenic efficiency, each sample shown in Figure 5.27 is compared to a 'truth' spectrum using the PNNL spectral library. Recall, the PNNL generates their spectral library using pure gas samples of 5 pptv. Figure 5.29 shows the scatter plot

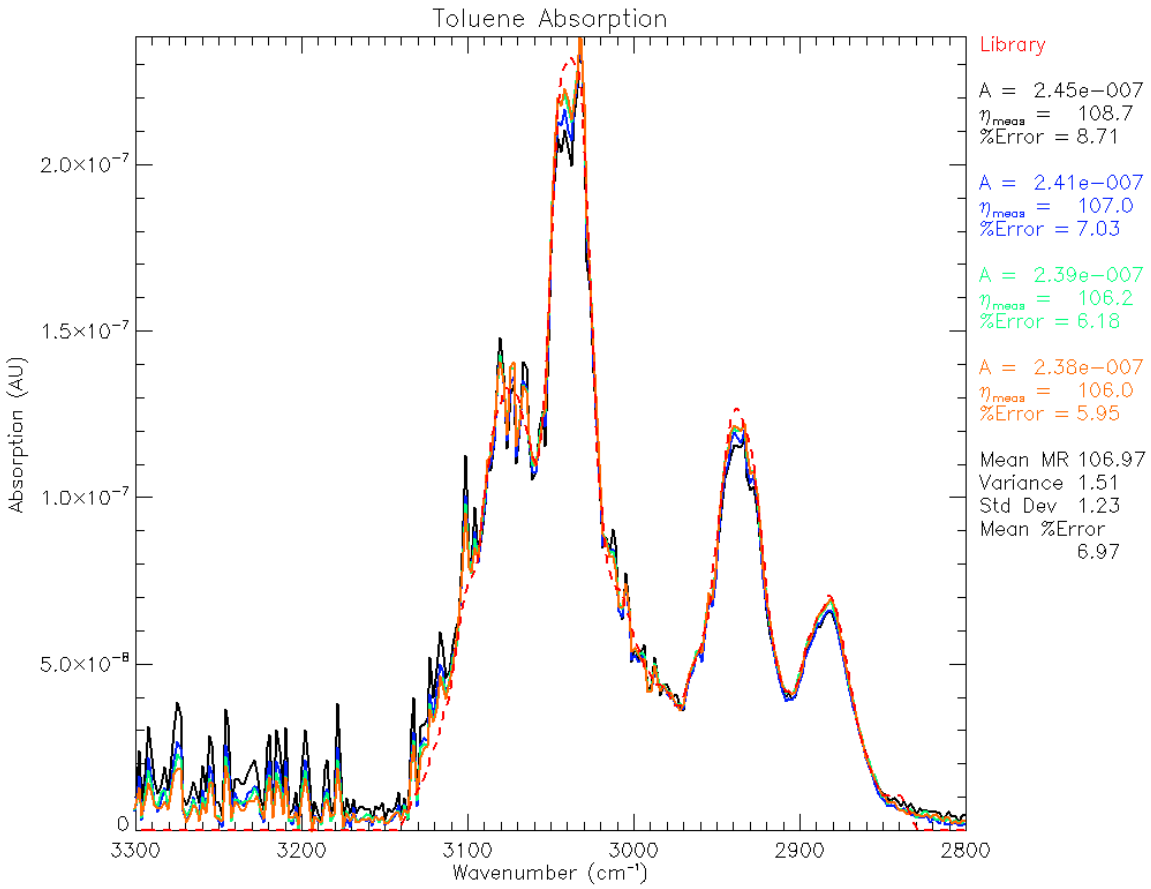

Figure 5.27. Base 10 absorption versus wavenumber for multiple observations of four-hour preconcentrated toluene spectra with library spectrum (red dashed trace) overlaid. Each color trace represents a different measurement. Key statistics for each measurement are listed at the right and color coded corresponding to the trace.

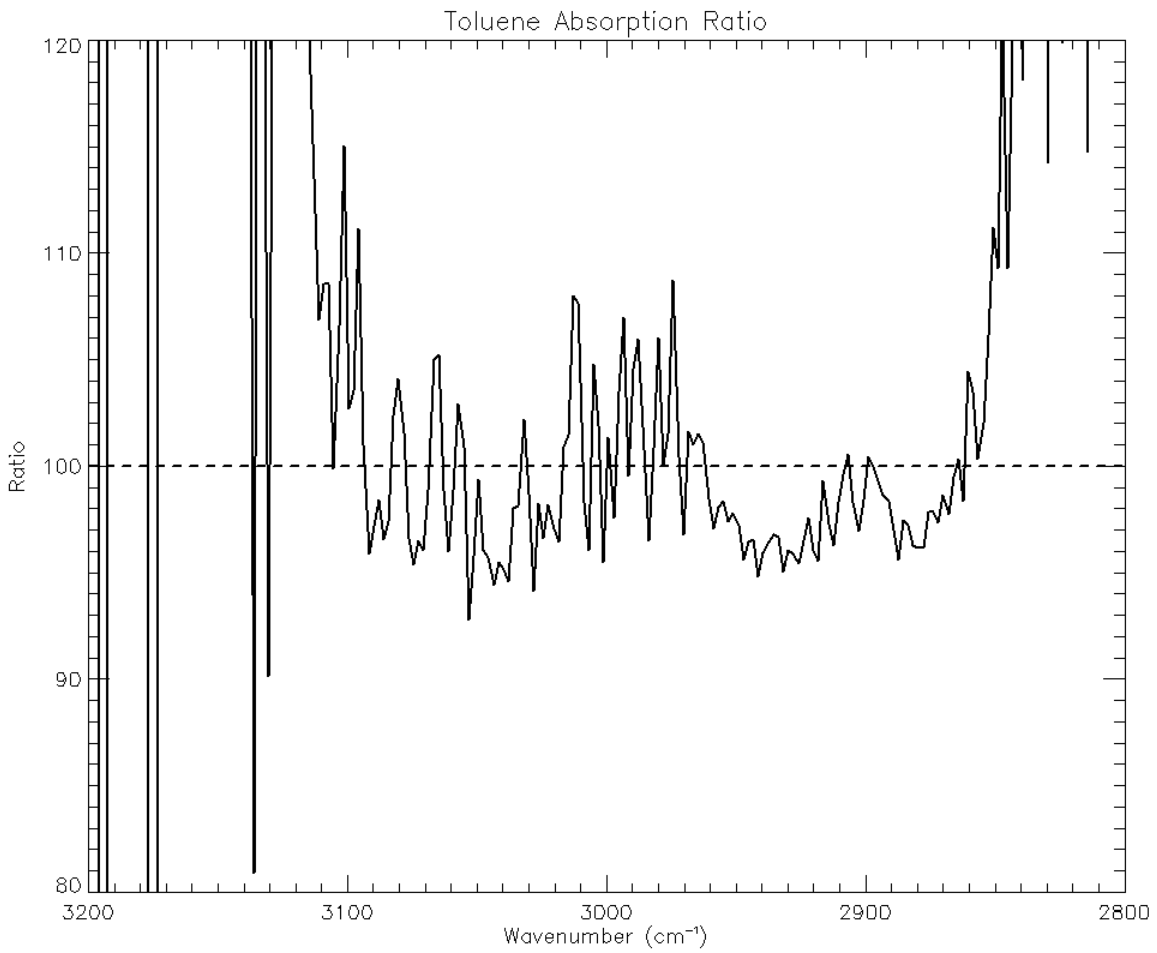

Figure 5.28. Ratio of base 10 absorption for sample one from Figure 5.27 to the mean of base 10 absorption for the remaining three spectra. The black dashed line is the 100% line.

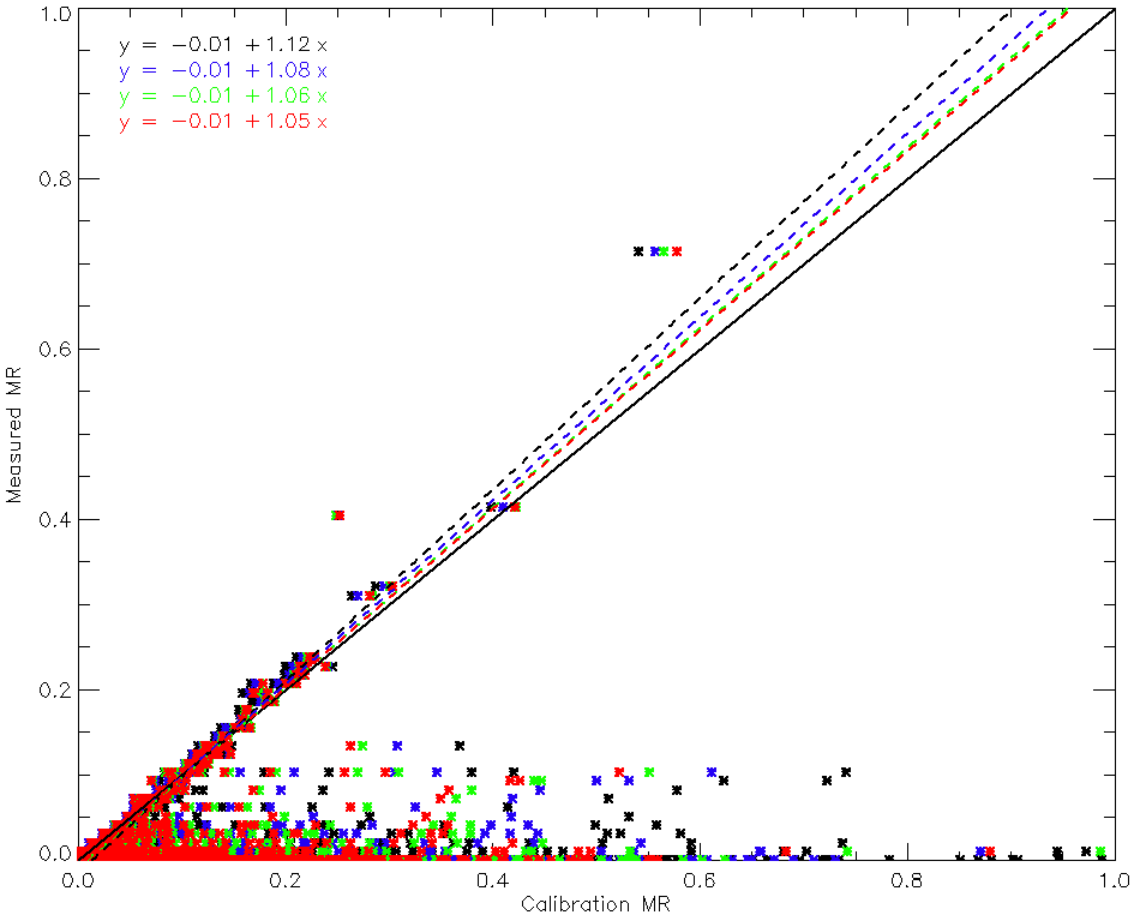

Figure 5.29. Scatter plot of 100-pptv toluene 'truth' spectrum absorption in base 10 compared with absorption from the observed spectra in Figure 5.27. Sample one, two, three, and four correspond to black, blue, green, and red, respectively. The linear regressions for each comparison are shown in the upper left, with the mean as y = -0.01 +1.09x.

comparing the 'truth' spectrum derived from the PNNL library spectrum and the four samples in Figure 5.27 across the entire spectral range. These results show strong agreement on the order of 1:1 with an intercept near zero in all cases, and a mean slope of 1.09 pptv.

Outliers are likely due to impurities in the calibration or purge gas bottle and the presence of trace amounts of H_2O and CO_2 as mentioned previously. If the spectral range considered in the scatter plot is reduced to 3200-3000 cm^{-1}, the density distribution of the points within 10% agreement is 64%, 26% contained in the origin indicating exact agreement with the 'truth' spectrum. The remaining 36% of the scatter points fall within 24% accuracy.

Finally, to quantify the trapping/desorption efficiency, a ratio was taken between a spectrum of unconcentrated 100 pptv toluene and a preconcentrated spectrum from Figure 5.27. Figure 5.30 shows the results of this ratio. The idealized trapping enrichment factor would be 240. Figure 5.30 shows that at least for the toluene absorption range, the mean enrichment factor is 236 with a median value of 238. Larger fluctuations past 3120 cm^{-1} dominate the variance of 182 and are the result of water vapor in the calibration or purge gas bottle and in the external optical path. During these calibration runs, the trapping/desorption efficiency was 100 +/- 2%.

In summary, the PNNL-derived peak-fitting quantification algorithm performs well on synthetic spectra generated using ambient mixing ratios. Retrievals from unconcentrated calibration gas standards fall within the manufacturer's accuracy specifications for both a mixture of alkenes in N_2 and a single alkene in air. Multiple preconcentration runs showed a high degree of consistency from run to run and when compared to a 'truth' spectrum.

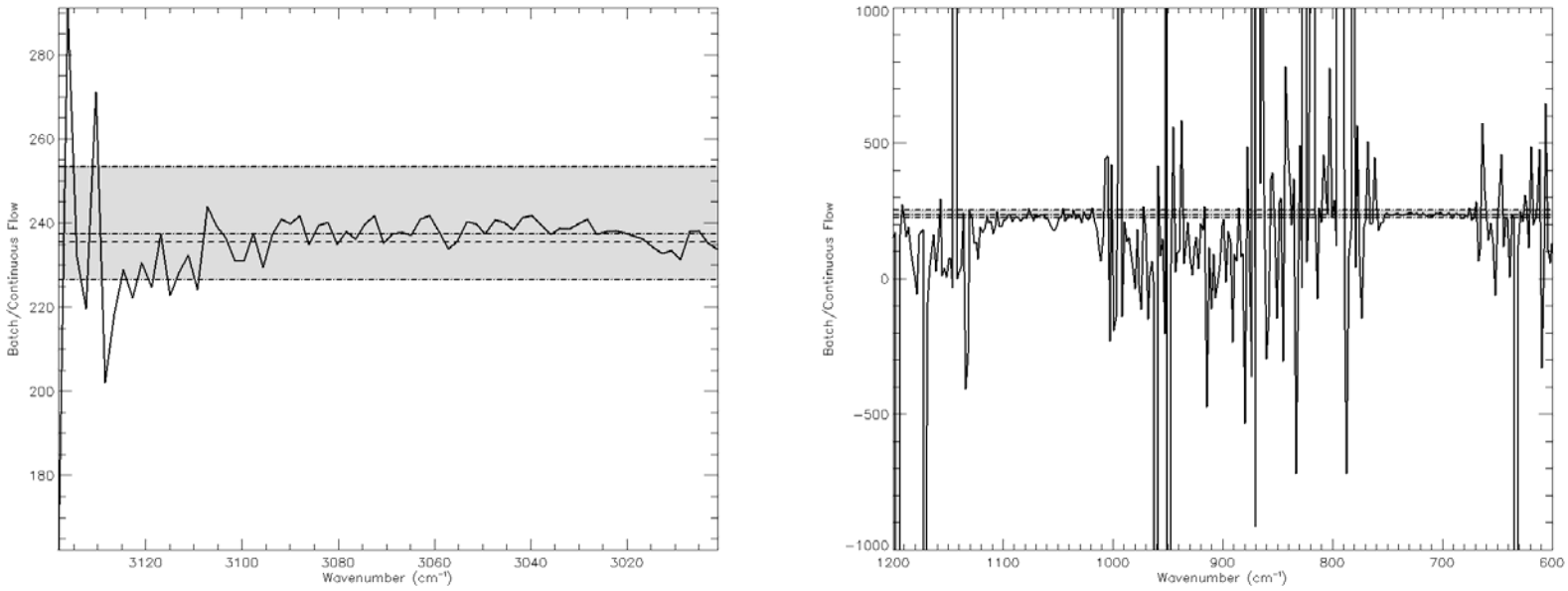

Figure 5.30. Ratio of preconcentrated to unconcentrated base 10 absorption for observed spectra of 100 ppt toluene. The panel on the left shows the toluene quantification range between 3200-3000 cm^{-1}. The mean ratio is the dashed line. The median ratio is the dot dashed line. The 1-σ standard deviation envelope is shown by the grey box. The values for these statistics are shown in the upper left. The panel on the right shows the same ratio within the H=C stretch range between 1200-600 cm^{-1}.

Comparing concentrated and unconcentrated spectra shows a high trapping/desorption efficiency when using calibration gas standards.

Additional sources of error not yet quantified deserve mentioning here to document the complexity involved in collecting highly accurate ambient observations in the field. Of constant concern with the optical system is the presence of trace gas contamination in the external optical path from source to detector. The Phoenix FTIR interferometer and detector compartments are purged and desiccated; however the sample compartment is not. If ambient air infiltrates the optical window shrouds, spurious H_2O and CO_2 appear in the measured spectrum. Background subtraction cancels much of thes trace gas contamination, except for slight changes from background to sample, because the time between background and sample is greater than four hours.

Additionally, slight changes in air temperature and water content modify the refractive index of the air in the FTIR interferometer. Refractive index changes, in turn, modify the optical path length for the metrology laser in the interferometer. These perturbations shift the spectral registration, change the ILS, reduce the SNR, and degrade measurement accuracy. Thermally stabilizing the FTIR and desiccating the interior will minimize these artifacts.

Finally, EMI/RFI and vibration will create spectral noise which degrades system SNR. Potential EMI/RFI sources include nearby cell phones, fluorescent lights, dimmer switches, air handlers, laboratory electronics, and electrical devices on the Phoenix instrument cart. Mechanical and acoustical vibration will also degrade the SNR. Potential sources include several large air handlers above the lab ceiling, personnel activity in and near the lab, and motors on the Phoenix instrument cart. EMI/RFI and vibration conditions at field

stations could be even worse than in the laboratory. As a part of the instrument hardening prior to field deployments, the entire system will be tested to assess its susceptibility to these noise sources and to define simple, practical, and inexpensive mitigation methods. For example, EMI/RFI mitigations could use nested Faraday cages around the instrument cart and the FTIR.

CHAPTER VI

FUTURE WORK

a. Subsystem-Level Improvements

As laboratory and field work continues, additional improvements are highly desirable. In particular, testing thus far has demonstrated simplification of the fluid, cryogenic, and electrical subsystems is critical prior to full, autonomous field operations are possible.

As originally designed, Phoenix had two replicate cryotraps as well as parallel routes for batch and continuous flow through the gas cell modes. Although these additional channels are desirable for on-board QA/QC, they require a large number of flow passages and plumbing connections. These conditions create packaging problems, increase leak potential, and increase the difficulty in debugging and leak detection. Phoenix would benefit from fewer flow passages and joints if the replicate cryotrap and/or parallel continuous flow channel were removed.

As the cryogenic method is improved, simplified, and optimized, the temporal resolution term (Δt_{trap}) of the preconcentration factor can be decreased by increasing the flow rate. Additional work will be required to determine the optimal flow rate to reduce the sampling time while maintaining or improving the detection thresholds across all target analytes.

Laboratory results collected during this Dissertation period indicated a simpler cryostat design will reduce the parasitic heat loads on the cryocooler, improve the overall data quality, and extend Phoenix measurement capabilities. In particular, omitting the replicate cryotrap, offloading the water and CO_2 traps, and reducing the thermal mass in the

cryotrap heat sink was required to obtain useful cool-down times and coldhead tempatures. Numerous heat sink designs were tested during the laboratory work presented within, however, additional research in this and related areas is required to obtain the target cryotrapping temperature of 100 K. The cryocooler is capable of reaching this temperature in its current configuration; however, the heat load placed on the coldhead by the heat sink and trap assembly reduces the minimum obtainable temperature. Achieving the desired reduction in temperature would expand the measurement capabilities of Phoenix by trapping compounds the current system cannot. Minimizing the heat load while maximizing trapping and desorption efficiency improves the detection limits as well as extends the capabilities of this technology.

Finally, simplifying the electrical subsystem is critical prior to full unattended operations during field deployment. Improved connectors, fewer electrical connections, and streamline cabling layout will simplify debugging and clean up the overall design. This is a critical step, not only for aesthetics, but also for reducing cross talk between devices, removing noise and sensor error. In addition, descoping the fluid and cryogenic subsystems, will reduce the number of sensors and flow meters/controllers. These systematic simplifications will eventually lead to a smaller, more-compact design and reduce the time required to debug and address issues with the system.

b. Improvements to the Quantitative Algorithm

At present, the Phoenix quantitative algorithm uses the peak fitting method described in §5.*f*. This method is sufficient for single-component samples or, to some extent, for non-overlapping multi-component samples. For Phoenix to adequately quantify the complex atmosphere the quantitative algorithm should contain a combination of a linear and non-

linear least squares fitting similar to those found in *Stutz and Platt* [1996] and *Spinei et al.* [2010]. For adequate application, additional research is required. However, research shows the non-linear nature of Beer's Law in the presence of small absorbers (Rayleigh scattering) requires NLLS rather than a simple linear regression fit.

c. Additional Validation

With proof-of-concept complete, additional method validation is required. The canister validation measurements were unsuccessful due to automation programming errors at the time of these measurements. It has been proposed to take Phoenix to Appalachian State University (ASU) to perform multiple validation tests. The objective of these tests would be to demonstrate Phoenix can provide the highest quality data for accurate measurements for a comprehensive suite of gases. It is absolutely critical that the techniques employed by any investigator be able to accurately measure the "true" composition of the atmosphere so the results obtained can be defended quantitatively. Using the resources and facilities at ASU, we would have the unique capability to rigorously test Phoenix against proven VOC measurements and techniques in the laboratory and the ambient atmosphere. Previous research shows measurements in the real atmosphere are the weak link in the overall process of accurately measuring VOCs. ASU has a proven track record in multi-scale calibration of VOCs, another critical factor in the process.

d. Field Measurements

Following system optimization and rigorous validation is complete, a comprehensive field shakedown is required to demonstrate the Phoenix technology in the real atmosphere. One possibility is field operations in Huntsville, AL. Site 014, a local EPA monitoring site, is situated in a valley with hills and a park to the south, a small residential area to the north, and

a four-lane highway to the east. This area experiences moderate vehicle traffic and often shows influences from the highway given the proper meteorological conditions. Site 014 is a NAAQS site currently monitoring particulate matter and O_3. Performing a long-term monitoring campaign at this site would be the most comprehensive study on VOCs in Huntsville to date. These measurements would demonstrate Phoenix as a high-quality VOC monitoring method and provide new insights on VOC mixing ratios in a moderately populated city in the Southeastern United States. Additional compounds would be added to the spectral algorithm to emphasize and categorize the effects of BVOCs on local O_3 mixing ratios and secondary VOC production.

A second possible field monitoring option is additional collaboration with Dr. Sive at ASU to perform long-term field measurements of BVOCs. The Appalachian Atmospheric Interdisciplinary Research (AppalAIR) is a high-altitude NOAA Global Monitoring site in Boone, North Carolina (36.20° N, 81.70° W, elevation 1100 m ASL). The site is equipped with chemical and meteorological instrumentation and is surrounded by forests. A detailed vegetation survey has been completed, and the species include northern red oak (*quercus rubra*), white oak (*quercus alba*), eastern white pine (*pinus strobes*), and yellow poplar (*liriodendron tulipifera*). The site is impacted by a variety of air mass types and compositions including urban emissions from Atlanta, GA to the south and Nashville, TN. and Ashville to the west, with relatively clean air masses to the east and north.

Continuous measurements of important chemical constituents and meteorological parameters in the atmosphere would be monitored at AppalAIR, including O_3, CO, CO_2, CH_4, NO, NO_y, SO_2, and Hg. Complementary bi-hourly data are available from Phoenix specifically measuring OVOCs (methanol, ethanol, acetone, MBO, isoprene,

methylvinylketone, and methacrolein). Hourly data are available from an automated *in situ* five channel GC system measuring C_2-C_{10} nonmethane hydrocarbons (NMHCs), including monoterpenes, halocarbons, and alkyl nitrates [*Sive et al.*, 2005], as well as high time resolution measurements using a PTR-MS for NMHCs, including total (i.e., non-speciated) monoterpene, and OVOCs [*Ambrose et al.*, 2007; *Jordan et al.*, 2010; *Talbot et al.*, 2005; *White et al.*, 2008]. This suite of measurement capabilities makes AppalAIR an invaluable location to carry out the proposed validation and quantification research.

Following the collection of an array of ambient measurements at various atmospheric locations, source apportionment and 1-D box modeling is the next logical step. To identify the sources for the observed VOCs, Lagrangian trajectory analysis such as HYSPLIT [*Draxler and Hess*, 1998] will provide source apportionment and identification capabilities to the data collection and analysis. Additionally, box modeling such as the NCAR Master Mechanism [*Madronich and Calvert*, 1989] would provide valuable insight into the validity of high-temporal-resolution data and its integration into 1-D chemical models. Current chemical models define their initial and boundary conditions using emissions inventories, which researchers have shown to be significantly lower than the observed emissions in most cases. Assimilation of actual VOC measurements with adequate temporal resolution would produce more atmospherically representative results than the emission inventories currently allow. This research could facilitate the building and deployment of additional Phoenix sensors to provide initial conditions and data assimilation into a local model, such as around the city of Birmingham, AL.

CHAPTER VII

CONCLUSIONS

The work contained within this Dissertation summarize over five years of work and study on the development, design, deployment, and demonstration of a complex analytical device capable of monitoring low-concentration VOCs in the atmosphere. The results from extensive laboratory studies and preliminary field data collection clearly demonstrate that Phoenix displays excellent capabilities, with potential for application in a wide array of atmospheric environments. With a trapping efficiency of 100 +/- 2% and an accuracy estimate of 10%, Phoenix could serve as a replacement or improvement on the current EPA standard monitoring technologies used for monitoring VOCs. Phoenix dramatically improves temporal resolution by a factor of six, and temporal resolution by either 36 times in the case of one in six sampling or 72 times in the case of one in twelve sampling. These sampling features make it capable of capturing important nocturnal/diurnal variability cycles critical for the prediction of O_3 and primary and secondary VOCs. Following further improvements on the cryogenic trapping system and simplification of the fluid and electrical subsystems, Phoenix would provide valuable scientific data to assess the effects of VOCs in a vast array of environments over long periods of uninterrupted operations.

As the focus of the American public turns more toward the contents of the air they breathe on a daily basis, the EPA will need to present more accurate near-real-time data to its customers and provide better predictions of the environment in which we live. With the EPA continually focused on regulations, it is critical to bring to light many of the atmospheric constituents the EPA does not currently monitor on a day to day basis and cannot capture in a

diurnal sense. Specifically, as citizens of the United States and around the world seek answers and accountability, Phoenix would offer rapid setup and autonomous operations, which would prove particularly advantageous in the case of the recent EPA School Air Toxics Monitoring Initiative and follow up monitoring after the discovery of several sampling deficiencies.[3]

With several other real-time monitoring techniques available, particularly GC methods, it is critical Phoenix participate in cross validation studies with either canisters or the currently existing real time methodologies to quantify the correlation and accuracy of Phoenix compared to other accepted methodologies. This critical venture would highlight the advantages and disadvantages of this method, and how to address any currently unknown errors in the system. Following the procurement of funding, this work should begin immediately.

[3] Personal communication with David Dayton (ERG) and Mike Jones (EPA)

APPENDIX:

OBSERVED SPECTRA

Contained within this appendix are the IR spectra from the 12-18 September 2011 observations collected by Phoenix. Phoenix collected all spectra at 1 cm^{-1} resolution using Boxcar apodization. The average RMS SNR during the sampling period was 322:1 with RMS noise being 1.8 x 10^{-6}. The average peak to peak SNR was 36.2:1 with peak to peak noise being 1.6 x 10^{-5}. To identify spectral features, please refer to Table 4.1 and Figure 4.1. The predominant feature between 600-700 cm^{-1} is from the C=O stretch caused by the remaining CO_2 in the cryocooled sample. This feature limits our spectral observation range using the peak fitting technique, which will be accounted for in future work.

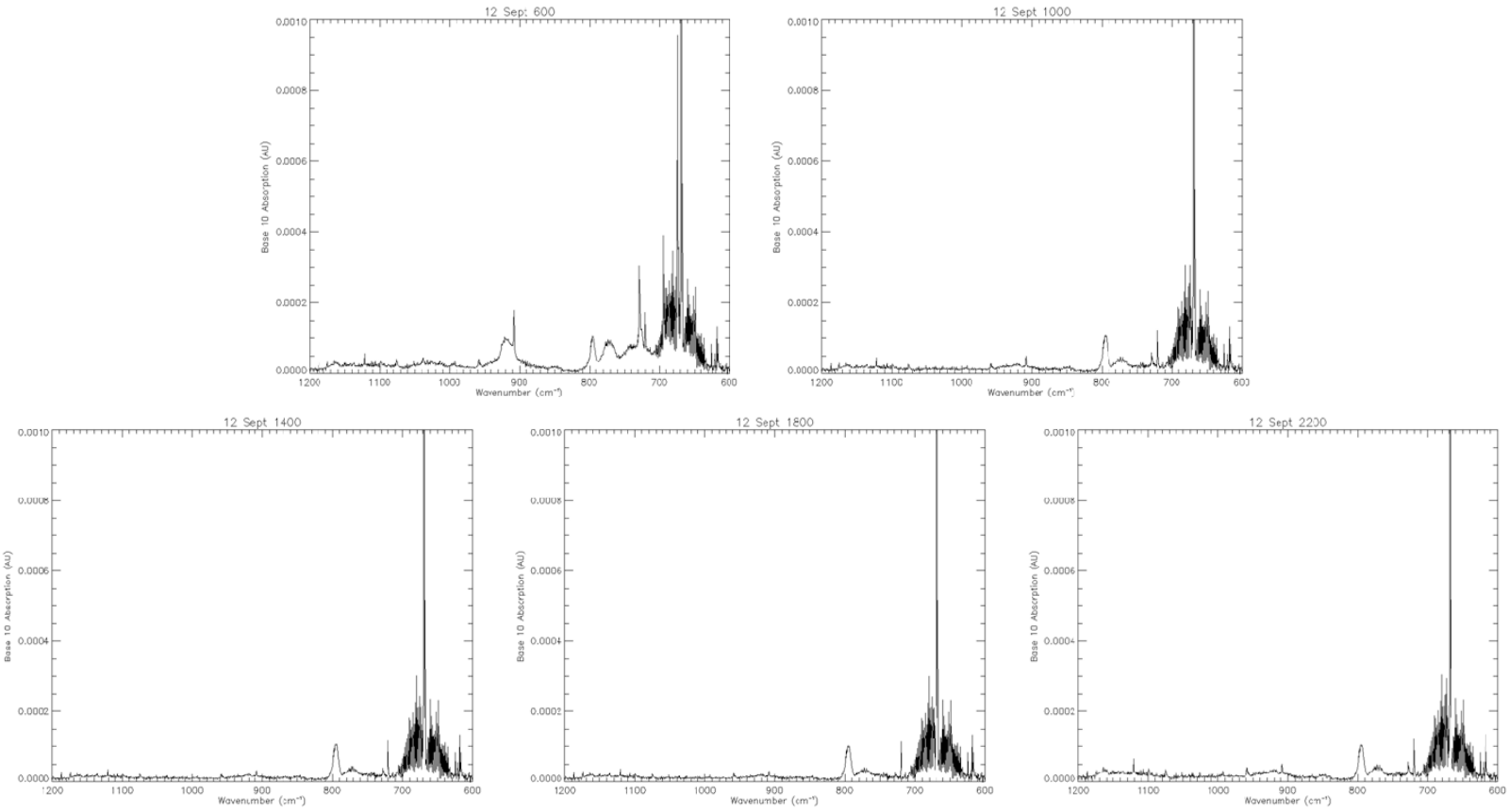

Figure A.1. Base 10 absorption versus wavenumber for the spectra collected during 12 September 2011. The spectral range is 1200-600 cm^{-1} to highlight major hydrocarbon absorption peaks.

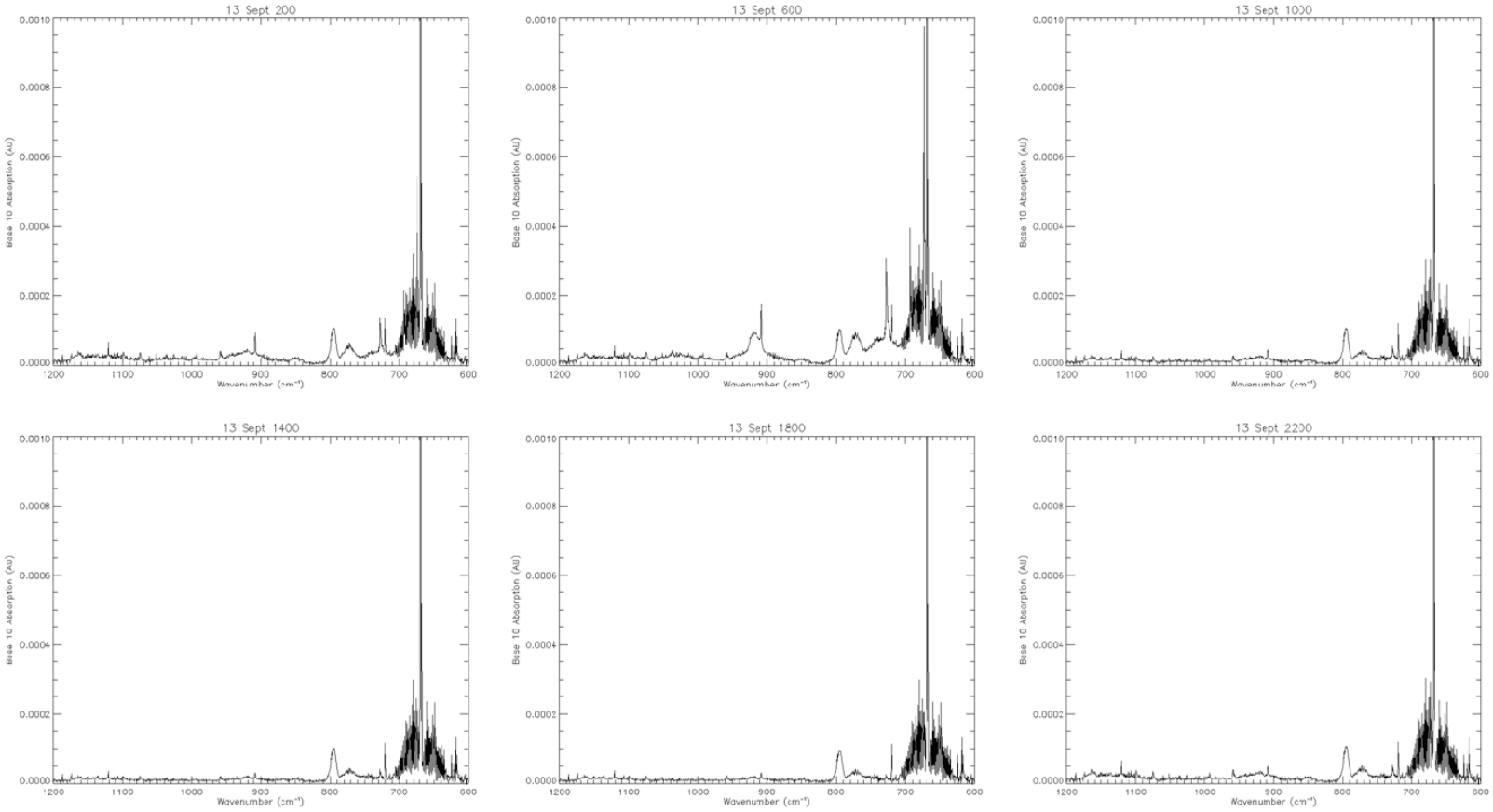

Figure A.2. Base 10 absorption versus wavenumber for the spectra collected during 13 September 2011. The spectral range is 1200-600 cm^{-1} to highlight major hydrocarbon absorption peaks.

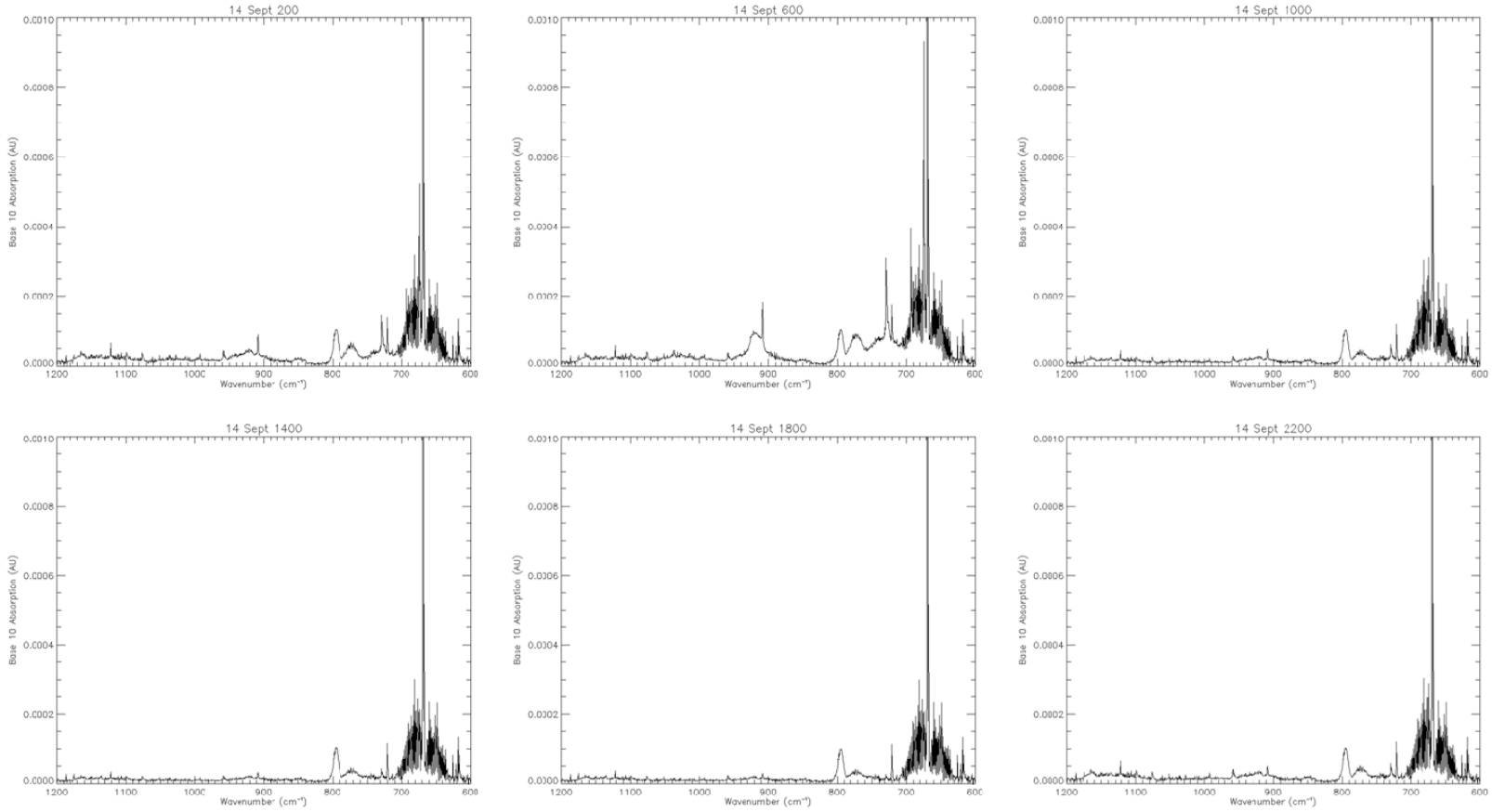

Figure A.3. Base 10 absorption versus wavenumber for the spectra collected during 14 September 2011. The spectral range is 1200-600 cm^{-1} to highlight major hydrocarbon absorption peaks.

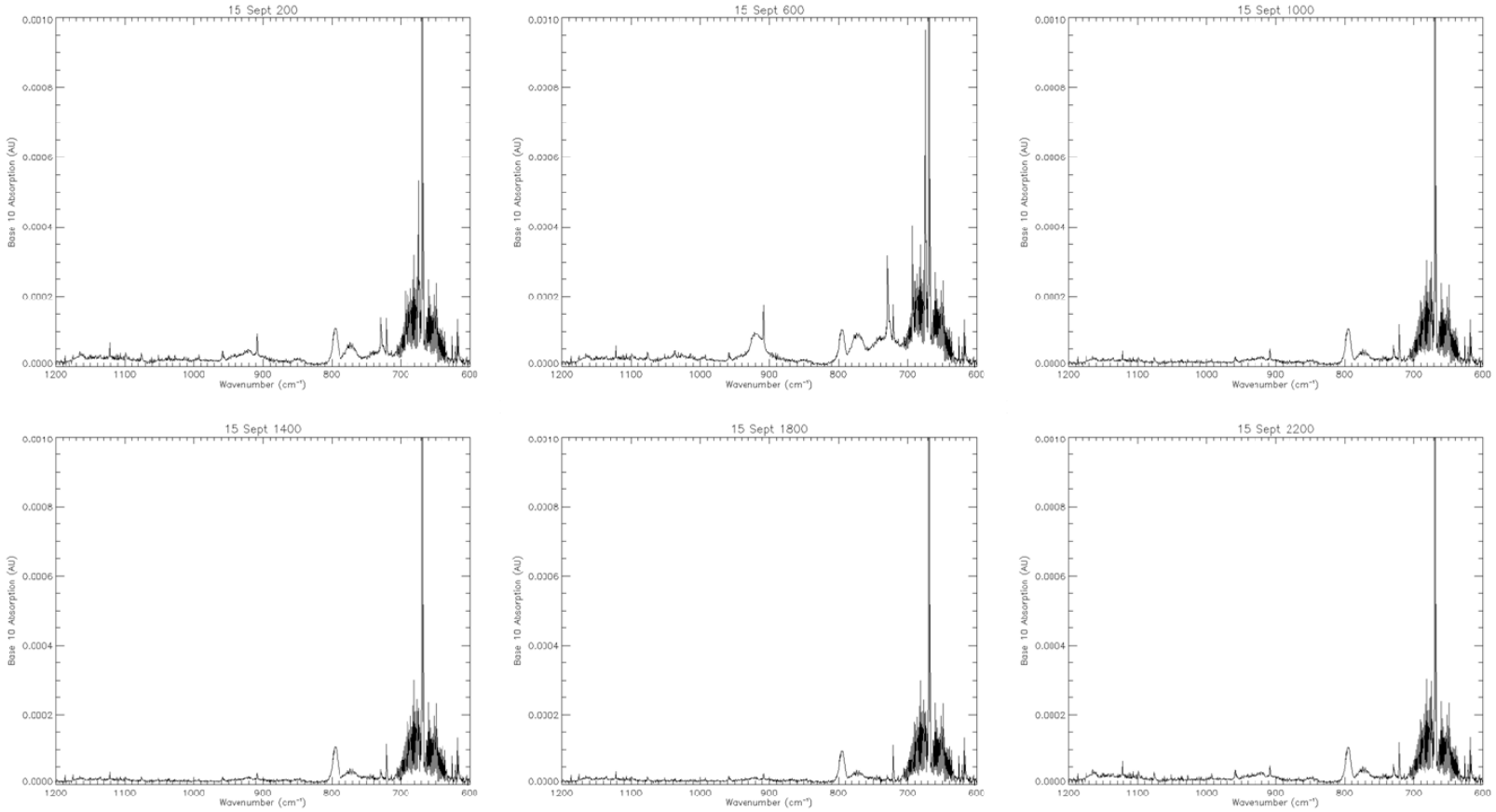

Figure A.4. Base 10 absorption versus wavenumber for the spectra collected during 15 September 2011. The spectral range is 1200-600 cm^{-1} to highlight major hydrocarbon absorption peaks.

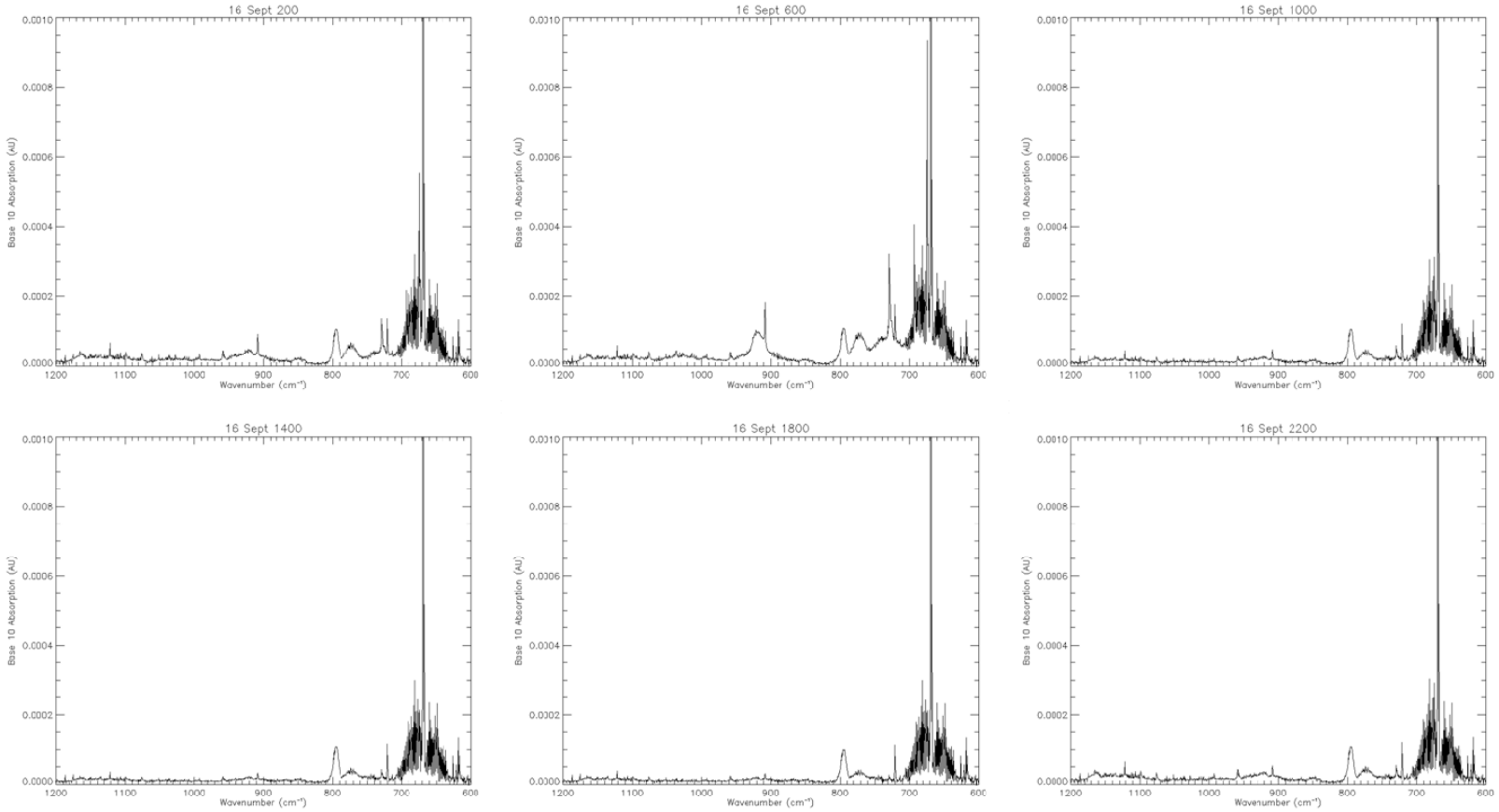

Figure A.5. Base 10 absorption versus wavenumber for the spectra collected during 16 September 2011. The spectral range is 1200-600 cm^{-1} to highlight major hydrocarbon absorption peaks.

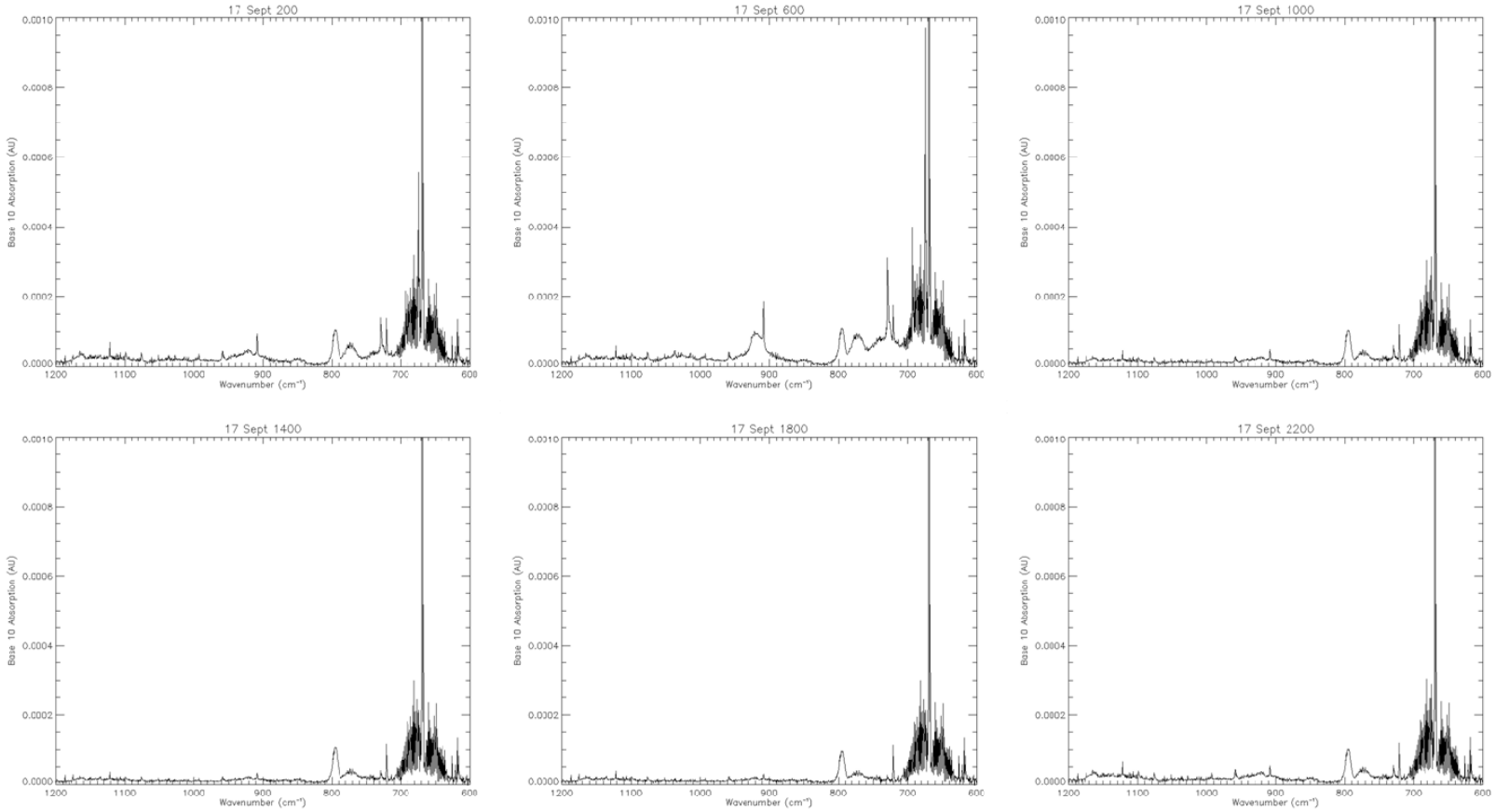

Figure A.6. Base 10 absorption versus wavenumber for the spectra collected during 17 September 2011. The spectral range is 1200-600 cm^{-1} to highlight major hydrocarbon absorption peaks.

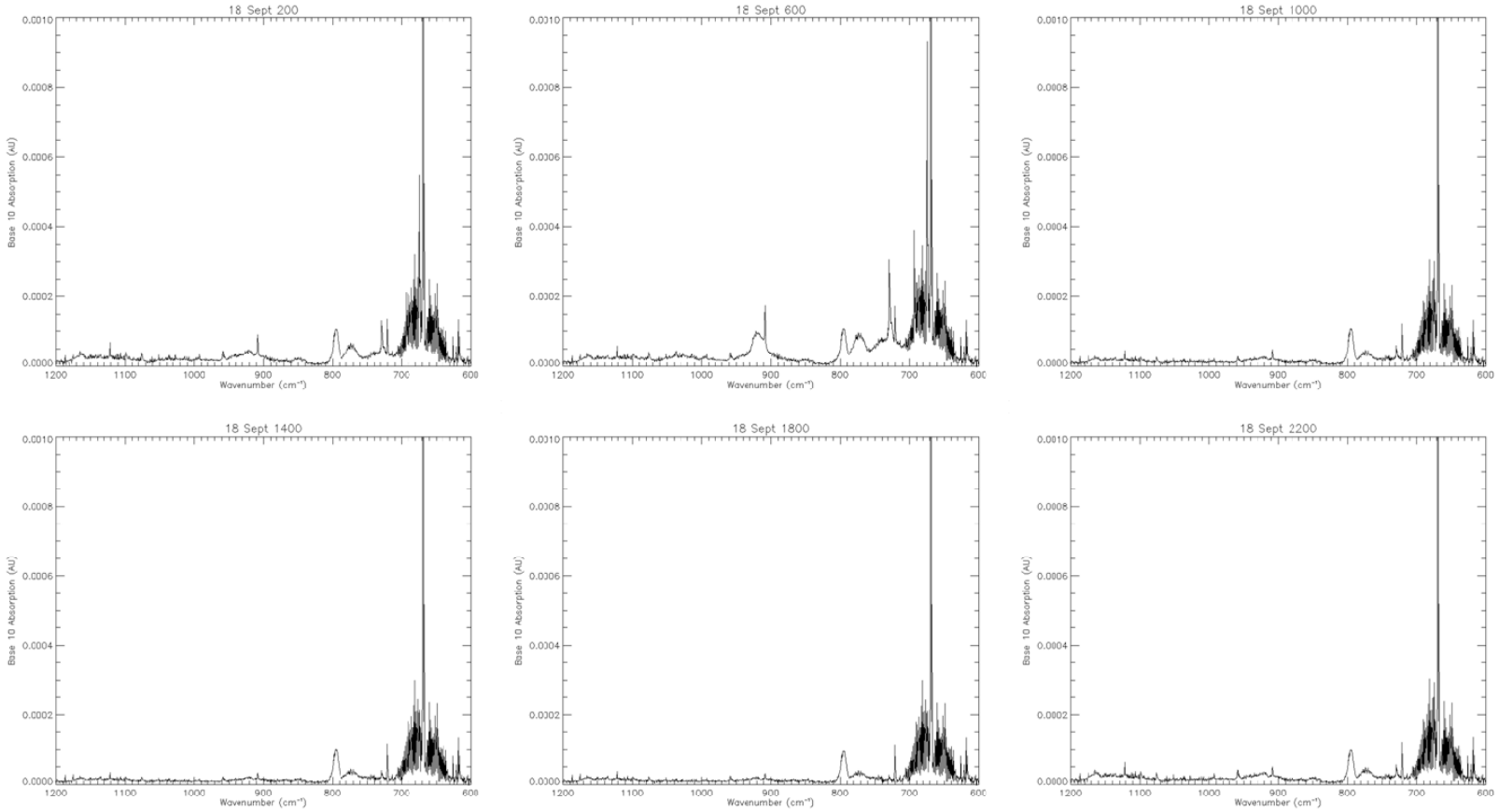

Figure A.7. Base 10 absorption versus wavenumber for the spectra collected during 18 September 2011. The spectral range is 1200-600 cm^{-1} to highlight major hydrocarbon absorption peaks.

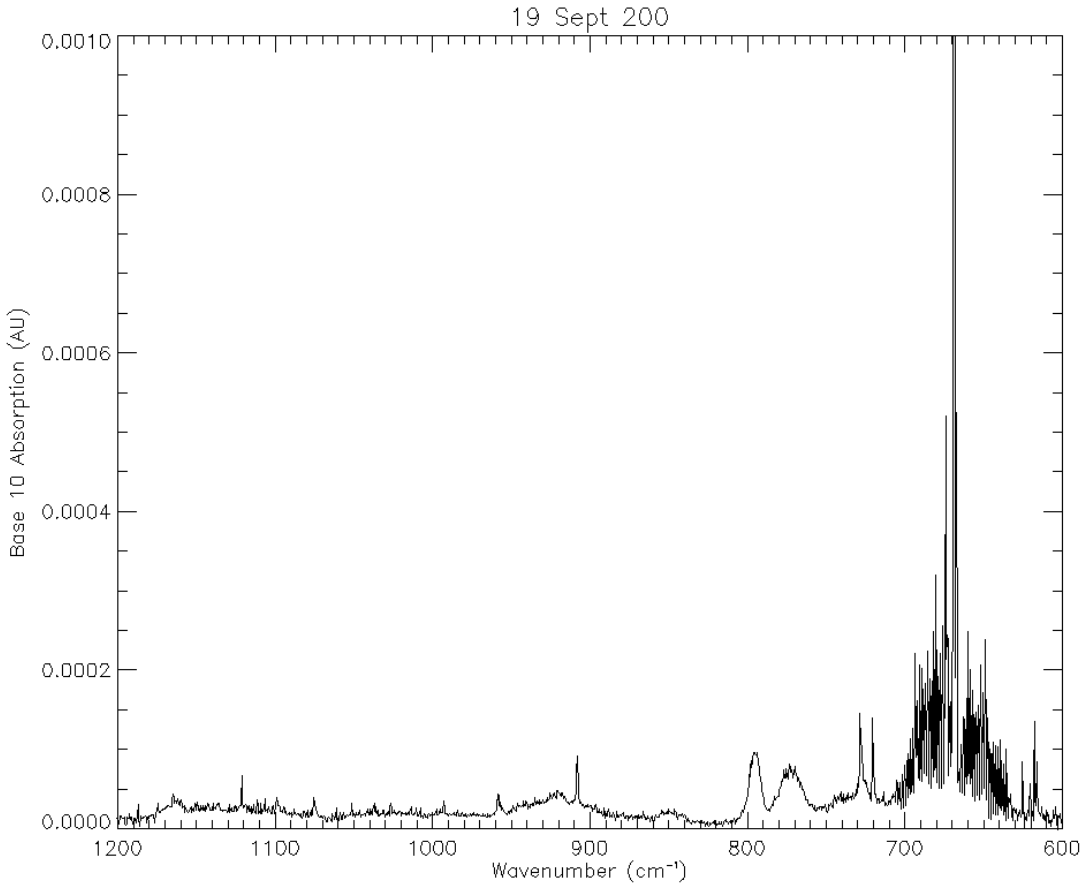

Figure A.8. Base 10 absorption versus wavenumber for the spectrum collected during 19 September 2011. The spectral range is 1200-600 cm^{-1} to highlight major hydrocarbon absorption peaks.

REFERENCES

Ambrose, J. L., H. Mao, H. R. Mayne, J. Stutz, R. Talbot, and B. C. Sive (2007), Nighttime nitrate radical chemistry at Appledore Island, Maine during the 2004 International Consortium for Atmospheric Research on Transport and Transformation, *J. Geophys. Res.*, *112*, D21302.

Ambrose, J. L. et al. (2010), A comparison of GC-FID and PTR-MS toluene measurements in ambient air under conditions of enhanced monoterpene loading, *Atmos. Meas. Tech.*, *3*, 959-980.

Anderson, R. J., and P. R. Griffiths (1975), Errors in absorbance measurements in infrared Fourier transform spectrometry because of limited instrument resolution, *Anal. Chem.*, *74*, 2339-2347.

Apel, E. C., J. G. Calvert, T. M. Gilpin, F. C. Fehsenfeld, and W. A. Lonneman (2003a), Nonmethane Hydrocarbon Intercomparison Experiment (NOMHICE): Task 4, ambient air, *J. Geophys. Res.*, *108*, 4300-4319.

Apel, E. C., A. J. Hills, R. Lueb, S. Zindel, S. Eisele, and D. D. Riemer (2003b), A fast-GC/MS system to measure C_2 to C_4 carbonyls and methanol aboard aircraft, *J. Geophys. Res.*, *108*, 8794-8806.

Apel, E. C. et al. (2008), Intercomparison of oxygenated volatile organic compound measurements at the SAPHIR atmosphere simulation chamber, *J. Geophys. Res.*, *113*, D20307.

Apel, E. C. et al. (2010), Chemical evolution of volatile organic compounds in the outflow of the Mexico City Metropolitan area, *Atmos. Chem. Phys.*, *10*, 2353-2375.

Atkinson, R. (1994), Gas-phase tropospheric chemistry of organic compounds, *J. Phys. Chem. Ref. Data*, *Monograph 2*, 1-214.

Atkinson, R. (2000), Atmospheric chemistry of VOCs and NO_x, *Atmos. Environ.*, *34*, 2063-2101.

Atkinson, R., and J. Arey (2003), Atmospheric degradation of volatile organic compounds, *Chem. Rev.*, *103*, 4605-4638.

Atkinson, R. et al. (2006), Evaluated kinetic and photochemical data for atmospheric chemistry: Volume II – gas phase reactions of organic species, *Atmos. Chem. Phys.*, *6*, 3625-4055.

Bacsik, Z., J. Mink, and G. Keresztury (2004), FTIR spectroscopy of the atmosphere: I. Principles and methods, *Appl. Spectrosc. Rev.*, *39*, 295-363.

Banta, R. M. et al. (1998), Daytime buildup and nighttime transport of urban ozone in the boundary layer during a stagnation episode, *J. Geophys. Res.*, *103*, 22519-22544.

Banta, R. M., L. Mahrt, D. Vickers, J. Sun, B. B. Balsley, Y. L. Pichugina, and E. J. Williams (2007), The Very stable boundary layer on nights with weak low-level jets, *J. Atmos. Sci.*, *64*, 3068-3090.

Barro, R., J. Regueiro, M. Llompart, and C. Garcia-Jares (2009), Analysis of industrial contaminants in indoor air: Part 1. Volatile organic compounds, carbonyl compounds, polycyclic aromatic hydrocarbons and polychlorinated biphenyls, *J. Chromatogr. A*, *1216*, 540-566.

Batterman, S. A., G.-Z. Zhang, and M. Baumann (1998), Analysis and stability of aldehydes and terpenes in electropolished canisters, *Atmos. Environ.*, *32*, 1647-1655.

Berkowitz, C. M., C. W. Spicer, and P. V. Doskey (2005), Hydrocarbon observations and ozone production rates in Western Houston during the Texas 2000 Air Quality Study, *Atmos. Environ.*, *39*, 3383-3396.

Biesenthal, T., Q. Wu, P. Shepson, H. Wiebe, K. Anlauf, and G. MacKay (1997), A study of relationships between isoprene, its oxidation products, and ozone in the Lower Fraser Valley, BC, *Atmos. Environ.*, *31*, 2049-2058.

Blanchard, C. L., G. M. Hidy, S. Tanenbaum, R. Rasmussen, R. Watkins, and E. Edgerton (2010), NMOC, ozone, and organic aerosol in the southeastern United States, 1999-2007: 1. Spatial and temporal variations of NMOC concentrations and composition in Atlanta, Georgia, *Atmos. Environ.*, *44*, 4827-4839.

Bloomer, B. J., K. Y. Vinnikov, and R. R. Dickerson (2010), Changes in seasonal and diurnal cycles of ozone and temperature in the eastern U.S., *Atmos. Environ.*, *44*, 2543-2551.

Blunden, J., V. P. Aneja, and W. A. Lonneman (2005), Characterization of non-methane volatile organic compounds at swine facilities in eastern North Carolina, *Atmos. Environ.*, *39*, 6707-6718.

Brault, J. W. (1985), Fourier transform spectroscopy, in *High Resolution in Astronomy: Proceedings from the Fifteenth Advanced Course of the Swiss Society of Astronomy and Astrophysics*, edited by A. O. Benz, et al., p. 61, Sass Fee, Sauverny, Observatoire de Geneve, Switzerland.

Brown, S. S. et al. (2007), Vertical profiles in NO_3 and N_2O_5 measured from an aircraft: Results from the NOAA P-3 and surface platforms during the New England Air Quality Study 2004, *J. Geophys. Res.*, *112*, D22304.

Brown, S. S. et al. (2009), Nocturnal isoprene oxidation over the Northeast United States in summer and its impact on reactive nitrogen partitioning and secondary organic aerosol, *Atmos. Chem. Phys.*, *9*, 3027-3042.

Buckley, P. I. (2009), Development of Extractive FTIR Spectroscopy with Cryogen-Free Low-Temperature Preconcentration for Autonomous Measurements of Gaseous Air Toxics, 114 pp, University of Alabama in Huntsville, Huntsville, AL.

Cantrell, C. A. et al. (2003), Peroxy radical behavior during the Transport and Chemical Evolution over the Pacific (TRACE-P) campaign as measured aboard the NASA P-3B aircraft, *J. Geophys. Res.*, *108*, 8797-8818.

Cantu, A., G. Pophal, S. Hall, and C. Laush (1998), A unique application of an extractive FTIR ambient air monitoring system for the simultaneous detection of multiple-ppb-level VOCs, *Appl. Phys.*, *67*, 493-496.

Carmichael, G. R. et al. (2003), Regional-scale chemical transport modeling in support of the analysis of observations obtained during the TRACE-P experiment, *J. Geophys. Res.*, *108*, 8823-8867.

Chameides, W. L. et al. (1992), Ozone precursor relationships in the ambient atmosphere, *J. Geophys. Res.*, *97*, 6037-6055.

Chang, C.-C., C.-F. OuYang, C.-H. Wang, S.-W. Chiang, and J.-L. Wang (2010), Validation of in-situ measurements of volatile organic compounds through flask sampling and gas chromatography/mass spectrometry analysis, *Atmos. Environ.*, *44*, 1301-1307.

Christian, T. J., B. Kleiss, R. J. Yokelson, R. Holzinger, P. J. Crutzen, W. M. Hao, T. Shirai, and D. R. Blake (2004), Comprehensive laboratory measurements of biomass-burning emissions: 2. First intercomparison of open-path FTIR, PTR-MS, and GC-MS/FID/ECD, *J. Geophys. Res.*, *109*, D02311.

Colman, J. J., A. L. Swanson, S. Meinardi, B. C. Sive, D. R. Blake, and F. S. Rowland (2001), Description of the analysis of a wide range of volatile organic compounds in whole air samples collected during PEM-Tropics A and B, *Anal. Chem.*, *73*, 3723-3731.

Couach, O., I. Balin, R. Jimenez, P. Ristori, S. Perego, F. Kirchner, V. Simeonov, B. Calpini, and H. van den Bergh (2003), An investigation of ozone and planetary boundary layer dynamics over the complex topography of Grenoble combing measurements and modeling, *Atmos. Chem. Phys.*, *3*, 549-562.

Davis, S. P., M. C. Abrams, and J. W. Brault (2001), *Fourier Transform Spectrometry*, 259 pp., Academic Press, San Diego, CA.

Dayal, B. S., and J. F. MacGregor (1997), Improved PLS algorithms, *J. Chemometrics*, *11*, 73-85.

de Gouw, J. et al. (2005), Budget of organic carbon in a polluted atmosphere: Results from the New England Air Quality Study in 2002, *J. Geophys. Res.*, *110*, D16305.

Devlin, R. B., J. A. Raub, and L. J. Folinsbee (1997), Health effects of ozone, *Sci. Med.*, 8-17.

Doezema, L. A., C. Bigley, G. Canzi, K. Chang, A. J. Hirning, J. Lee, and N. Von der Ahe (2010), The influence of sampling protocol on nonmethane hydrocarbon mixing ratios, *Atmos. Environ.*, *44*, 900-908.

Doraiswamy, P., C. Hogrefe, W. Hao, R. F. Henry, K. Civerolo, J.-Y. Ku, G. Sistla, J. J. Schwab, and K. L. Demerjian (2009), A diagnostic comparison of measured and model-predicted speciated VOC concentrations, *Atmos. Environ.*, *43*, 5759-5770.

Draxler, R. R., and G. D. Hess (1998), An overview of the HYSPLIT_4 modeling system for trajectories, dispersion, and deposition, *Aus. Met. Mag.*, *47*, 295-308.

Dunlea, E. J. et al. (2009), Evolution of Asian aerosols during transpacific transport in INTEX-B, *Atmos. Chem. Phys.*, *9*, 7257-7287.

Environmental Protection Agency (1990), Clean Air Act Amendments of 1990: Conference Report to Accompany S. 1630, Report Number 101-952, edited, pp. 139-162, Washington, DC, EPA.

Environmental Protection Agency (1997), Compendium Method TO-15: Determination of volatile organic compounds (VOCs) in air collected in specially-prepared canisters and analyzed by gas chromatography/mass spectrometry (GC-MS), edited, p. 66, Research Triangle Park, NC, EPA.

Environmental Protection Agency (1999), Test Method 320: Measurement of vapor phase organic and inorganic emissions by extractive Fourier transform infrared (FTIR) spectroscopy, edited, p. 20, Research Triangle Park, NC.

Esler, M. B., D. W. T. Griffith, S. R. Wilson, and L. P. Steele (2000a), Precision trace gas analysis by FT-IR spectroscopy. 1. Simultaneous analysis of CO_2, CH_4, N_2O, and CO in air, *Anal. Chem.*, *72*, 206-215.

Esler, M. B., D. W. T. Griffith, S. R. Wilson, and L. P. Steele (2000b), Precision trace gas analysis by FT-IR spectroscopy. 2. The $^{13}C/^{12}C$ isotope ratio of CO_2, *Anal. Chem.*, *72*, 216-221.

Fehsenfeld, F. et al. (1992), Emissions of volatile organic compounds from vegetation and the implications for atmospheric chemistry, *Global Biogeochem. Cycles*, *6*, 389-430.

Fenger, J. (1999), Urban air quality, in *Air Pollution Science for the 21st Century*, edited by J. Austin, et al., pp. 1-52, Elsevier, Amsterdam, Denmark.

Filipy, J., B. Rumburg, G. Mount, H. Westberg, and B. Lamb (2006), Identification and quantification of volatile organic compounds from a dairy, *Atmos. Environ.*, *40*, 1480-1494.

Finlayson-Pitts, B. J., and J. N. Pitts (2000), *Chemistry of the Upper and Lower Atmosphere*, Academic Press, San Diego.

Fried, A. et al. (2003), Airborne tunable diode laser measurements of formaldehyde during TRACE-P: Distributions and box model comparisons, *J. Geophys. Res.*, *108*, 8798-8821.

Fried, A. et al. (2008), Role of convection in redistributing formaldehyde to the upper troposphere over North America and the North Atlantic during the summer 2004 INTEX campaign, *J. Geophys. Res.*, *113*, D17306.

Gilman, J. B. et al. (2009), Measurements of volatile organic compounds during the 2006 TexAQS/GoMACCS campaign: Industrial influences, regional characteristics, and diurnal dependencies of the OH reactivity, *J. Geophys. Res.*, *114*, D00F06.

Goldan, P. D., W. C. Kuster, F. C. Fehsenfeld, and S. A. Montzka (1995), Hydrocarbon measurements in the southeastern United States: The Rural Oxidants in the Southern Environment (ROSE) Program 1990, *J. Geophys. Res.*, *100*, 25945-25963.

Goldan, P. D., W. C. Kuster, E. Williams, P. C. Murphy, F. C. Fehsenfeld, and J. Meagher (2004), Nonmethane hydrocarbon and oxy hydrocarbon measurements during the 2002 New England Air Quality Study, *J. Geophys. Res.*, *109*, D21309.

Gorham, K. A., N. J. Blake, R. A. VanCuren, H. E. Fuelberg, S. Meinardi, and D. R. Blake (2010), Seasonal and diurnal measurements of carbon monoxide and nonmethane hydrocarbons at Mt. Wilson, California: Indirect evidence of atomic Cl in the Los Angeles basin, *Atmos. Environ.*, *44*, 2271-2279.

Griffin, R. J., D. Dabdub, and J. H. Seinfeld (2002), Secondary organic aerosol: 1. Atmospheric chemical mechanism for production of molecular constituents, *J. Geophys. Res.*, *107*, 4332-4358.

Griffiths, P. R., and J. A. deHaseth (2007), *Fourier Transform Infrared Spectrometry*, 2nd ed., 529 pp., Wiley & Sons, Hoboken, NJ.

Guenther, A. B. et al. (1995), A global model of natural volatile organic compound emissions, *J. Geophys. Res.*, *100*, 8873-8892.

Guenther, A. B., C. Geron, T. Pierce, B. Lamb, P. Harley, and R. Fall (2000), Natural emissions of non-methane volatile organic compounds, carbon monoxide, and oxides of nitrogen from North America, *Atmos. Environ.*, *34*, 2205-2230.

Haaland, D. M., and R. G. Easterling (1982), Application of new least-squares methods for the quantitative infrared analysis of multicomponent samples, *Appl. Spectrosc.*, *36*, 665-673.

Haaland, D. M., and E. V. Thomas (1988a), Partial least-squares methods for spectral analyses. 1. Relation to other quantitative calibration methods and the extraction of qualitative information, *Anal. Chem.*, *60*, 1193-1202.

Haaland, D. M., and E. V. Thomas (1988b), Partial least-squares methods for spectral analyses. 2. Application to simulated and glass spectral data, *Analytical Chemistry*, *60*, 1202-1208.

Haberhauer-Troyer, C., E. Rosenberg, and M. Grasserbauer (1999), Investigation of membrane dryers and evaluation of a new ozone scrubbing material for the sampling of organosulphur compounds in air, *J. Chrom. A*, *852*, 589-595.

Hagerman, L. M., V. P. Aneja, and W. A. Lonneman (1997), Characterization of non-methane hydrocarbons in the rural southeast United States, *Atmos. Environ.*, *31*, 4017-4038.

Harris, F. J. (1978), On the use of windows for harmonic analysis with the Discrete Fourier Transform, *Proc. IEEE*, *66*, 51-83.

Hartikainen, K., A.-M. Nerg, M. Kivimäenpää, S. Kontunen-Soppela, M. Mäenpää, E. Oksanen, M. Rousi, and T. Holopainen (2009), Emissions of volatile organic compounds and leaf structural characteristics of European aspen (*Populus tremula*) grown under elevated ozone and temperature, *Tree Physiology*, *29*, 1163-1173.

Heald, C. L. et al. (2008), Total observed organic carbon (TOOC) in the atmosphere: A synthesis of North American observations, *Atmos. Chem. Phys.*, *8*, 2007-2025.

Helmig, D. (1999), Air analysis by gas chromatography, *J. Chrom. A*, *843*, 129-146.

Herndon, S. C., M. S. Zahniser, D. D. Nelson, Jr., J. Shorter, J. B. McManus, R. Jimanez, C. Warneke, and J. A. de Gouw (2007), Airborne measurements of HCHO and HCOOH during the New England Air Quality Study 2004 using a pulsed quantum cascade laser spectrometer, *J. Geophys. Res.*, *112*.

Hirschfeld, T. (1979), Quantitative FTIR: A Detailed Look at the Problems Involved, in *Fourier Transform Infrared Spectroscopy: Appliactions to Chemical Systems*, edited by J. R. Ferraro and L. J. Basile, pp. 193-242, Academic Press, New York, NY.

Hoffmann, T., J. R. Odum, F. Bowman, D. Collins, D. Klockow, R. C. Flagan, and J. H. Seinfeld (1997), Formation of organic aerosols from the oxidation of biogenic hydrocarbons, *J. Atmos. Chem.*, *26*, 189-222.

Jacob, D. J. (2000), Heterogeneous chemistry and tropospheric ozone, *Atmos. Environ.*, *34*, 2131-2159.

Jacobson, M. Z. (2005), *Fundamentals of Atmospheric Modeling*, 2nd ed., 813 pp., Cambridge University Press, New York, NY.

Jacobson, M. Z., and D. G. Streets (2009), Influence of future anthropogenic emissions on climate, natural emissions, and air quality, *J. Geophys. Res.*, *114*, D08118.

Jenkin, M. E., S. M. Saunders, and M. J. Pilling (1997), The tropospheric degradation of volatile organic compounds: a protocol for mechanism development, *Atmos. Environ.*, *31*, 81-104.

Jenkin, M. E., and K. C. Clemitshaw (2000), Ozone and other secondary photochemical pollutants: Chemical processes governing their formation in the planetary boundary layer, in *Air Pollution Science for the 21st Century*, edited by J. Austin, et al., pp. 285-338, Elsevier, Amsterdam, Denmark.

Jobson, B. T. et al. (2004), Hydrocarbon source signatures in Houston, Texas: Influence of the petrochemical industry, *J. Geophys. Res.*, *109*, D24305.

Jobson, B. T., R. Volkamer, E. Velasco, G. Allwine, H. Westberg, B. Lamb, M. L. Alexander, C. M. Berkowitz, and L. T. Molina (2010), Comparison of aromatic hydrocarbon measurements made by PTR-MS, DOAS and GC-FID in Mexico City during the MCMA 2003 field experiment, *Atmos. Chem. Phys.* , *10*, 1989-2005.

Jordan, C., E. Fitz, T. Hagan, B. Sive, E. Frinak, K. Haase, L. Cottrell, S. Buckley, and R. Talbot (2010), Long-term study of VOCs measured with PTR-MS at a rural site in New Hampshire with urban influences, *Atmos. Chem. Phys.*, *9*, 4677-4697.

Karnosky, D. F., J. M. Skelly, K. E. Percy, and A. H. Chappelka (2007), Perspectives regarding 50 years of research on effects of tropospheric ozone air pollution of U.S. forests, *Environ. Pollution*, *147*, 489-506.

Kelly, T. J., and M. W. Holdren (1995), Applicability of canisters for sample storage in the determination of hazardous air pollutants, *Atmos. Environ.*, *29*, 2595-2608.

Kim, K.-H., S.-I. Oh, and Y.-J. Choi (2004), Comparative analysis of bias in the collection of airborne pollutants: Tests on major aromatic VOC using three types of sorbent-based methods, *Talanta*, *64*, 518-527.

Kim, S., T. Karl, A. Guenther, G. Tyndall, J. Orlando, P. Harley, R. Rasmussen, and E. Apel (2010), Emissions and ambient distributions of biogenic volatile organic compounds (BVOC) in a ponderosa pine ecosystem: interpretation of PTR-MS mass spectra, *Atmos. Chem. Phys.*, *10*, 1759-1771.

Kleinman, L. (2005), The dependence of tropospheric ozone production rate on ozone precursors, *Atmos. Environ.*, *39*, 575-586.

Kleinman, L. I. (1994), Low and high NO_x tropospheric photochemistry, *J. Geophys. Res.*, *99*, 16831-16838.

Koppmann, R., F. J. Johnen, A. Khedim, J. Rudolph, A. Wedel, and B. Wiards (1995), The influence of ozone on light nonmethane hydrocarbons during cryogenic preconcentration, *J. Geophys. Res.*, *100*, 11383-11391.

Kuang, S. et al. (2011), Nocturnal ozone enhancement in the lower troposphere observed by lidar, *Atmos. Environ.*, *45*, 6078-6084.

Kumar, A., and I. Viden (2007), Volatile organic compounds: Sampling methods and their worldwide profile in ambient air, *Environ. Monit. Assess.*, *131*, 301-321.

Lee, J. P., and M. B. Comisarow (1987), Advantageous apodization functions for magnitude-mode Fourier Transform Spectroscopy, *Appl. Spectrosc.*, *41*, 93-98.

Legreid, G., J. B. Lööv, J. Staehelin, C. Hueglin, M. Hill, B. Buchmann, A. S. H. Prevot, and S. Reimann (2007), Oxygenated volatile organic compounds (OVOCs) at an urban background site in Zürich (Europe): Seasonal variation and source allocation, *Atmos. Environ.*, *41*, 8409-8423.

Lelieveld, J., and F. Dentener (2000), What controls tropospheric ozone?, *J. Geophys. Res.*, *105*, 3531-3551.

Lippmann, M. (1991), Health effects of tropospheric ozone, *Environ. Sci. Tech.*, *25*, 1954-1962.

Logan, J. A. (1985), Tropospheric ozone: Seasonal behavior, trends, and anthropogenic influence, *J. Geophys. Res.*, *90*, 10463-10482.

Madronich, S., and J. G. Calvert (1989), *The NCAR Master Mechanism of Gas Phase Chemistry - Version 2.0*, NCAR Technical Note NCAR/TN-333+STR.

Mattu, M. J., G. W. Small, and M. A. Arnold (1997), Applications of mulitvariate calibration techniques to quantitative analysis on bandpass-filtered Fourier-transform infrared interferogram data, *Appl. Spectrosc.*, *51*, 1369-1376.

McClenny, W. A., J. D. Pleil, M. W. Holdren, and R. N. Smith (1984), Automated cryogenic preconcentration and gas chromatographic determination of volatile organic compounds in air, *Anal. Chem.*, *56*, 2947-2951.

McClenny, W. A., K. D. Oliver, and E. H. Daughtrey (1995), Dry purging of solid adsorbent traps to remove water vapor before thermal desorption of trace organic gases, *J. Air and Waste Manag. Assoc.*, *45*, 792-800.

McKeen, S. A. et al. (1997), Photochemical modeling of hydroxyl and its relationship to other species during the Tropospheric OH Photochemistry Experiment, *J. Geophys. Res.*, *102*, 6467-6493.

Miller, B. R., R. F. Weiss, P. K. Salameh, T. Tanhua, B. R. Greally, J. Muhle, and P. G. Simmonds (2008), Medusa: A sample preconcentration and GC-MS detector system for *in situ* measurements of atmospheric trace halocarbons, hydrocarbons, and sulfur compounds, *Anal. Chem.*, *80*, 1536-1545.

Miller, L. et al. (2010), Intra-urban correlation and spatial variability of air toxics across an international airshed in Detroit, Michigan (USA) and Windsor, Ontario (Canada), *Atmos. Environ.*, *44*, 1162-1174.

Newchurch, M. J. et al. (2011), Spatio-temporal veriations of ozone in the boundary layer and free troposphere, paper presented at AGU Fall Meeting 2011, San Francisco, CA

Ng, N. L. et al. (2007), Effect of NO_x level on secondary organic aerosol (SOA) formation from the photooxidation of terpenes, *Atmos. Chem. Phys.*, *7*, 5159-5174.

NIOSH (2003), *Organic and Inorganic Gases by Extractive FTIR Spectrometry*, Fourth ed., 47 pp., The National Institute of Occupational Safety and Health.

Ochiai, N., A. Tsuji, N. Nakamura, S. Daishima, and D. B. Cardin (2002), Stabilities of 58 volatile organic compounds in fused-silia-lined and SUMMA polished canisters under various humidified conditions, *J. Environ. Mon.*, *4*, 879-889.

Olson, D. A., D. M. Hammond, R. L. Seila, J. M. Burke, and G. A. Norris (2009), Spatial gradients and source apportionment of volatile organic compounds near roadways, *Atmos. Environ.*, *43*, 5647-5653.

Park, C., G. W. Schade, and I. Boedeker (2010), Flux measurements of volatile organic compounds by the relaxed eddy accumulation method combined with a GC-FID system in urban Houston, Texas, *Atmos. Environ.*, *44*, 2605-2614.

Pate, B., R. K. M. Jayanty, M. R. Peterson, and G. F. Evans (1992), Temporal stability of polar organic compounds in stainless steel canisters, *J. Air and Waste Manag. Assoc.*, *42*, 460-462.

Peischl, J. et al. (2010), A top-down analysis of emissions from selected Texas power plants during TexAQS 2000 and 2006, *J. Geophys. Res.*, *115*, D16303.

Philpotts, A. R., W. Thain, and P. G. Smith (1951), Effect of finite slit width on infrared absorption measurements, *Anal. Chem.*, *23*, 268-272.

Piccot, S. D., J. J. Watson, and J. W. Jones (1992), A global inventory of volatile organic compound emissions from anthropogenic sources, *J. Geophys. Res.*, *97*, 9897-9912.

Pressley, S., B. Lamb, H. Westberg, A. Guenther, J. Chen, and E. Allwine (2004), Monoterpene emissions from a Pacific Northwest Old-Growth Forest and impact on regional biogenic VOC emission estimates, *Atmos. Environ.*, *38*, 3089-3098.

Qin, Y., T. Walk, R. Gary, X. Yao, and S. Elles (2007), C_2-C_{10} nonmethane hydrocarbons measured in Dallas, USA--Seasonal trends and diurnal characteristics, *Atmos. Environ.*, *41*, 6018-6032.

Rappenglück, B., and P. Fabian (1999), Nonmethane hydrocarbons (NMHC) in the Greater Munich Area/Germany, *Atmos. Environ.*, *33*, 3843-3857.

Richardson, R. L., H. Yang, and P. R. Griffiths (1998), Effects of detector nonlinearity on spectra measured on three commercial FT-IR spectrometers, *Appl. Spectrosc.*, *52*, 572-578.

Riemer, D. et al. (1998), Observations of nonmethane hydrocarbons and oxygenated volatile organic compounds at a rural site in the southeastern United States, *J. Geophys. Res.*, *103*.

Riemer, N., H. Vogel, B. Vogel, B. Schell, I. Ackermann, C. Kessler, and H. Hass (2003), Impact of the heterogeneous hydrolysis of N_2O_5 on chemistry and nitrate aerosol formation in the lower troposphere under photosmog conditions, *J. Geophys. Res.*, *108*, 4144-4165.

Rothman, L. S. et al. (2009), The HITRAN 2008 molecular spectroscopic database, *J. Quant. Spectrosc. and Rad. Trans.*, *110*, 533-572.

Russo, R. S., Y. Zhou, M. L. White, H. Mao, R. Talbot, and B. C. Sive (2010), Multi-year (2004-2008) record of non-methane hydrocarbons and halocarbons in New England: Seasonal variations and regional sources, *Atmos. Chem. Phys.*, *10*, 4909-4929.

Ryerson, T. B. et al. (1998), Emission lifetimes and ozone formation in power plant plumes, *J. Geophys. Res.*, *103*, 22569-22583.

Ryerson, T. B. et al. (2001), Observations of ozone formation in power plant plumes and implecations for ozone control strategies, *Science*, *292*, 719-723.

Salawitch, R. J. et al. (1994), The diurnal variation of hydrogen, nitrogen, and chlorine radicals: Implications for the heterogeneous production of HNO_2, *Geophys. Res. Lett.*, *21*.

Salmond, J. A., and I. G. McKendry (2002), Secondary ozone maxima in a very stable nocturnal boundary layer: observations from the Lower Fraser Valley, BC, *Atmos. Environ.*, *36*, 5771-5782.

Seinfeld, J. H., and S. N. Pandis (2006), *Atmospheric Chemistry and Physics: From Air Pollution to Climate Change*, Second ed., 1203 pp., Wiley and Sons, Hoboken, NJ.

Sharpe, S. W., T. J. Johnson, R. L. Sams, P. M. Chu, G. C. Rhoderick, and P. A. Johnson (2004), Gas-phase databases for quantitative infrared spectroscopy, *Appl. Spectrosc.*, *58*, 1452-1461.

Sicard, P., O. Lesne, N. Alexandre, A. Mangin, and R. Collomp (2011), Air quality trends and potential health effects - Development of an aggregate risk index, *Atmos. Environ.*, *45*, 1145-1153.

Sillman, S., D. He, M. R. Pippin, P. H. Daum, D. G. Imre, L. I. Kleinman, J. H. Lee, and J. Weinstein-Lloyd (1998), Model correlations for ozone, reactive nitrogen, and peroxides for Nashville in comparison with measurements: Implications for O_3-NO_x-hydrocarbon chemistry, *J. Geophys. Res.*, *103*, 22629-22644.

Sillman, S. et al. (2002), Loss of isoprene and sources of nighttime OH radicals at a rural site in the United States: Results from photochemical models, *J. Geophys. Res.*, *107*, 4043-4057.

Sillman, S., and D. He (2002), Some theoretical results concerning O_3-NO_x-VOC chemistry and NO_x-VOC indicators, *J. Geophys. Res.*, *107*, 4659-4674.

Sive, B. C., Y. Zhou, D. Troop, Y. Wang, W. C. Little, O. W. Wingenter, and R. Talbot (2005), Development of a cryogen-free concentration system for measurement of volatile organic compounds, *Anal. Chem.*, *77*, 6989-6998.

Spinei, E., S. A. Carn, N. A. Krotkov, G. H. Mount, K. Yang, and A. Krueger (2010), Validation of ozone monitoring instrument SO2 measurements in the Okmok volcanic cloud over Pullman, WA, July 2008, *J. Geophys. Res.*, *115*, D00L08.

Stutz, J., and U. Platt (1996), Numerical analysis and estimation of the statistical error of differential optical absorption spectroscopy measurements with least-squares methods, *Appl. Opt.*, *35*, 6041-6053.

Su, Y.-C., C.-C. Chang, and J.-L. Wang (2008), Construction of an automated gas chromatography/mass spectrometry system for the analysis of ambient volatile organic compounds with on-line internal standard calibration, *J. Chrom. A*, *1201*, 134-140.

Talbot, R., H. Mao, and B. Sive (2005), Diurnal characteristics of surface level O_3 and other important trace gases in New England, *J. Geophys. Res.*, *110*, D09307.

Thomas, E. V., and D. M. Haaland (1990), Comparison of multivariate calibration methods for quantitative spectral analysis, *Anal. Chem.*, *62*, 1091-1099.

Volkamer, R., L. T. Molina, M. J. Molina, T. Shirley, and W. H. Brune (2005), DOAS measurement of glyoxal as an indicator for fast VOC chemistry in urban air, *Geophys. Res. Lett.*, *32*, L08806.

Wagner, V., C. Schiller, and H. Fischer (2001), Formaldehyde measurements in the marine boundary layer of the Indian Ocean during the 1999 INDOEX cruise of the R/V Ronald H. Brown, *J. Geophys. Res.*, *106*, 28529-28538.

Wang, J.-L., W.-L. Chen, G.-R. Her, and C.-C. Chan (2002), Validation of ozone precursor measurement through inter-comparison with NOx and CO measurement, *Atmos. Environ.*, *36*, 3041-3047.

Warneke, C. et al. (2004), Comparison of daytime and nighttime oxidation of biogenic and anthropogenic VOCs along the New England coast in summer during New England Air Quality Study 2002, *J. Geophys. Res.*, *109*, D10309.

Warneke, C. et al. (2010), Biogenic emission measurement and inventories determination of biogenic emissions in the eastern United States and Texas and comparison with biogenic emission inventories, *J. Geophys. Res.*, *115*, D00F18.

Weisel, C. P. (2002), Assessing exposure to air toxics relative to asthma, *Environ. Health Perspec. Supp.*, *110*, 527-540.

Weiss, R. F., J. Mühle, P. K. Salameh, and C. M. Harth (2008), Nitrogen trifluoride in the global atmosphere, *Geophys. Res. Lett.*, *35*, L20821.

Wert, B. P. et al. (2003), Signatures of terminal alkene oxidation in airborne formaldehyde measurements during TexAQS 2000, *J. Geophys. Res.*, *108*, 4104-4118.

White, M. L. et al. (2008), Volatile organic compounds in northern New England marine and continental environments during the ICARTT 2004 campaign, *J. Geophys. Res.*, *113*, D08S90.

Wold, S., M. Sjostrom, and L. Eriksson (2001), PLS-regressionL a basic tool of chemometrics, *Chemometrics and Intelligent Laboratory Systems*, *58*, 109-130.

Wong, K. W., and J. Stutz (2010), Influence of nocturnal vertical stability on daytime chemistry: A one-dimensional model study, *Atmos. Environ.*, *44*, 3753-3760.

Xiao, X., D. S. Cohan, D. W. Byun, and F. Ngan (2010), Highly nonlinear ozone formation in the Houston region and implications for emission controls, *J. Geophys. Res.*, *115*, D23309.

Zaveri, R. A. et al. (2010), Nighttime chemical evolution of aerosol and trace gases in a power plant plume: Implications for secondary organic nitrate and organosulfate aerosol formation, NO_3 radical chemistry, and N_2O_5 heterogeneous hydrolysis, *J. Geophys. Res.*, *115*, D12304.

Zhou, Y., R. K. Varner, R. S. Russo, O. W. Wingenter, K. B. Haase, R. Talbot, and B. C. Sive (2005), Coastal water source of short-lived halocarbons in New England, *J. Geophys. Res.*, *110*, D21302.

Zhou, Y. et al. (2008), Bromoform and dibromomethane measurements in the seacoast region of New Hampshire, 2002-2004, *J. Geophys. Res.*, *113*, D08305.

Ziemba, L. D., J. E. Dibb, R. J. Griffin, C. H. Anderson, S. I. Whitlow, B. L. Lefer, B. Rappenglück, and J. Flynn (2010), Heterogeneous conversion of nitric acid to nitrous acid on the surface of primary organic aerosol in an urban atmosphere, *Atmos. Environ.*, *44*, 4081-4089.